UNIVERSITY OF SOUTHAMPTON

Faculty of Engineering, Science and Mathematics
Optoelectronics Research Centre

The study of surface SHG and polygonal microcavity design for nonlinear applications on $LiNbO_3$

by

Tleyane J. Sono

A thesis submitted in partial fulfillment for the degree of Doctor of Philosophy

May 2009

Declaration of Authorship

I, Tleyane J. Sono, declare that this thesis titled, The study of surface SHG and polygonal microcavity design for nonlinear applications on $LiNbO_3$ and the work presented in it are my own. I confirm that:

- This work was done wholly or mainly while in candidature for a research degree at this University.
- Where any part of this thesis has previously been submitted for a degree or any other qualification at this University or any other institution, this has been clearly stated.
- Where I have consulted the published work of others, this is always clearly attributed.
- Where I have quoted from the work of others, the source is always given. With the exception of such quotations, this thesis is entirely my own work.
- I have acknowledged all main sources of help.
- Where the thesis is based on work done by myself jointly with others, I have made clear exactly what was done by others and what I have contributed myself.

Signed: _____

Date: _____

UNIVERSITY OF SOUTHAMPTON

Abstract

Faculty of Engineering, Science and Mathematics
Optoelectronics Research Centre

Doctor of Philosophy

The study of surface SHG and polygonal microcavity design for nonlinear applications on $LiNbO_3$

by Tleyane J. Sono

A z-cut congruent lithium niobate crystal ($LiNbO_3$) has been used in this thesis, as a platform for the surface second harmonic generation (SHG) studies and for the designs of polygonal microcavities for nonlinear applications.

Reflection second harmonic generation (RSHG) experiments were performed on $LiNbO_3$ to reveal the interfacial layer symmetry as the crystal is rotated around the z axis. RSHG was also used, unsuccessfully as a non-destructive tool to map the domain-inverted area in the poled $LiNbO_3$ crystals. But nevertheless, the polarity of the direction of the y-axis of the crystal was determined from RSHG data and the data shows that this direction also inverts, during domain inversion. RSHG was used unsuccessfully to monitor the relaxation of the internal field within the domain inverted area of the poled $LiNbO_3$.

A general operational principle of optical microcavities was discussed, in which a detailed theory governing the operational modes of a resonating hexagonal microcavity, made from bulk $LiNbO_3$ crystal was reviewed for nonlinear device applications. A model for a total internal reflection (TIR) technique for the QPM method in a double-resonating hexagonal microcavity was formulated. The TIR-QPM model was based on finding a suitable hexagonal dimension in which, both the fundamental and SHG signal resonate simultaneously while at the same time allowing QPM to occur via TIR. The TIR-QPM model and the FDTD simulation were used to demonstrate the potential capability of the double-resonating hexagonal microcavity for efficient SHG. The model to achieve a nonlinear microcavity by periodically poling ring/disk resonator Ti:$LiNbO_3$ ridge waveguide was introduced.

Acknowledgements

I wish to express my sincere thanks and appreciation to all those people who have helped and encouraged me during the course of this work. In particular, I would like to express my deepest gratitude to the following people:

My supervisor, Professor R. W. Eason, for his constant guidance and interest in this work since the beginning. For his caring support during hard times and for his interest on the personal well being of his student within the ORC.
My former supervisor, Dr. J. G. Frey, for his guidance throughout the RSHG work in the School of Chemistry and for his understanding on my career plans to move to the ORC.
Dr. L. Danos, then a postdoc researcher in JGF's group in the School of Chemistry for guidance and advice through the experimental and data analysis of the RSHG work.
My co-supervisor, Dr. S. Mailis, for his constant support and advice on all the experimental and theoretical aspects throughout this work.
Dr. C. Riziotis, of the Photonics and Nanoapplications Laboratory, Theoretical and Physical Chemistry Institute, Athens, Greece, for his constant guidance and advice on the theoretical and simulation work on the hexagonal microcavity studies.
Dr. Eleanor Tarbox for her non-tiring efforts on proof reading of this thesis.
To the technical staff in our clean room: Neil and Dave for making sure that the clean room facilities were in good working condition and for all the technical help.
To the technical staff at the James Watt Nanofabrication Centre (JWNC) at University of Glasgow, in particular Linda Polock for accommodating us to work in their clean room after the fire incident at our University.
To the Commonwealth Scholarship commission for awarding me the Commonwealth scholarship to the United Kingdom.
To my family for the encouraging support they have shown during this study, especially to my wife Felicia, who supported me unwaveringly for the many long years that I was away completing this work, it was hard but we made it through.

In loving memory of my parents
Mhalamhala Joseph and Malehu Rebecca
Sono

...

Contents

Contents **1**

List of Figures **5**

List of Tables **11**

1 Introduction **12**

1.1 Objectives 12

1.2 Introduction and Summary of Chapters 13

2 Summary of the Physical and Chemical properties of crystalline Lithium Niobate **16**

2.1 Introduction 16

2.2 Crystal Structure 16

2.3 Stoichiometry 18

2.4 Properties 21

2.4.1 Paraelectric Phase 21

2.4.2 Ferroelectricity 21

2.4.3 Domain Inversion in $LiNbO_3$ 23

2.4.4 Pyroelectric Properties 25

2.4.5 Piezoelectric effect 25

2.4.6 Sellmeier equation and refractive index 26

2.4.7 Photorefractive effect 27

2.4.8 Reduction of photorefraction 28

2.4.9 Linear Optical Properties 28

2.4.10 Nonlinear Optical Properties 29

2.4.11 Microcavities for application in nonlinear optical processes 30

2.5 Conclusion 31

3 Reflection Second Harmonic Generation 32
3.1 Introduction . . . 32
3.2 Theory . . . 34
3.2.1 Permutation symmetry and spatial symmetry . . . 36
3.2.1.1 Intrinsic permutation . . . 36
3.2.1.2 Overall permutation and Kleinman symmetry . . . 37
3.2.2 The Three Layer Model for RSHG . . . 37
3.3 Experimental . . . 43
3.3.1 RSHG experimental setup . . . 43
3.3.2 Poling setup . . . 45
3.4 Conclusion . . . 45

4 RSHG: Results and Discussions 47
4.1 Introduction . . . 47
4.2 Use of RSHG to reveal the symmetry of the interfacial layer of a z-cut $LiNbO_3$ crystal . . . 48
4.3 Methods for the characterization of the inverted domains . . . 53
4.3.1 Differences in SHG signal between the $+z$ and $-z$ domains of a z-cut $LiNbO_3$ crystal . . . 54
4.4 Use of RSHG to detect the inversion of the y-axis $+y \Leftrightarrow -y$ on reversal of the spontaneous polarization . . . 56
4.5 Time-dependent Surface Second Harmonic Generation effects . . . 63
4.6 Conclusion . . . 67

5 Optical MicroCavity design and modeling 69
5.1 Introduction . . . 69
5.2 Review of Microcavities . . . 71
5.2.1 Material . . . 72
5.3 Theory of a Microcavity . . . 73
5.3.1 Input and Output Coupling Mechanism . . . 79
5.3.2 Ray optics approach for a hexagonal microcavity . . . 81
5.4 Simulations . . . 84
5.4.1 FDTD formulation . . . 84
5.5 Simulation Results for the Hexagonal Microcavity . . . 89
5.5.1 Cavity spectrum . . . 91
5.5.2 Reducing Cavity losses . . . 91
5.6 Steady-state simulation . . . 96
5.7 Conclusion . . . 100

6 Nonlinear Optical Hexagonal Microcavities 101
6.1 Introduction . . . 101
6.2 Theory . . . 104
6.2.1 TIR-QPM . . . 104
6.2.2 The Model of TIR-QPM in a hexagonal cavity . . . 108
6.3 Simulation Results . . . 111
6.3.1 Determination of the ideal cavity size using FDTD simulation . . . 112
6.3.2 Steady-state Cavity Response . . . 114
6.3.3 SHG efficiency via TIR-QPM in a hexagonal cavity . . . 115
6.4 Conclusion . . . 120

7 Feasibility studies of a nonlinear micro-ring resonator on a Ti:indiffused $LiNbO_3$ waveguide 121
7.1 Introduction . . . 121
7.2 Theory . . . 124
7.2.1 Ti:$LiNbO_3$ . . . 124
7.2.2 Nonlinear ring resonator . . . 125
7.3 Bend loss . . . 126
7.4 Experimental . . . 127
7.4.1 Photolithography mask design . . . 127
7.4.2 Substrate preparation . . . 127
7.4.3 Ti deposition . . . 129
7.4.4 Ti indiffusion . . . 129
7.4.5 Poling of Ti:$LiNbO_3$ . . . 129
7.4.6 Determination of n_{eff} . . . 130
7.4.7 Applying photoresist . . . 131
7.4.8 Soft bake . . . 131
7.4.9 Exposure . . . 131
7.4.10 Post exposure bake . . . 131
7.4.11 Development . . . 132
7.4.12 Dry etching of the ridge waveguide . . . 132
7.5 Results and Discussion . . . 136
7.5.1 Effective index . . . 136
7.5.2 BPM simulation . . . 137
7.6 Conclusion . . . 141

8 Conclusions and Further work **143**
8.1 Conclusions 143
8.2 Further Work 147

Bibliography **149**

List of Figures

2.1 Top view of the hexagonal unit cells of $LiNbO_3$ outlined by the solid black lines. In the standard conversion $a = b \equiv x$ and $c \equiv z$ and the y axis is taken to be normal to the xz plane. The mirror planes are along the y-axis [1]. The picture is reproduced using Diamond 3.1d software. 17

2.2 Hexagonal unit cell of $LiNbO_3$ [1]. Picture reproduced using Diamond 3.1d software 18

2.3 Hexagonal unit cell of $LiNbO_3$ showing the x-cut face. The oxygen planes along the y-axis are denoted by the black horizontal lines. The order of the metallic ions in between oxygen lines along the y-axis is found to be ..., Nb^{5+}, Li^{+}, v, Nb^{5+}, Li^{+}, ... going in one direction while the order along the anti-direction, along the y-axis, is found to be ..., v, Li^{+}, Nb^{5+},v, ... [1]. Picture reproduced using Diamond 3.1d software 19

2.4 Phase diagram of lithium niobate (after [2]) 22

2.5 x-cut face of the virgin and poled $LiNbO_3$ crystal. In the poled state, the order of the cations in between the oxygen layers both along the z and the y axis appears to be reversed. 24

3.1 a) Three layer model of an interface. Medium r consists of air, while both medium m and t are made of $LiNbO_3$. b) In this figure x' is the new space-fixed coordinate relative to x as the sample is rotated around z by the azimuthal angle (φ). γ and Γ are the input and output polarisation angles respectively. See the text for further details. 38

3.2 Experimental set-up. The dotted line shows the electrical signal path. PBS1 and PBS2 are the input and output polarizer, BS: beam splitter. PD: the photodiode. UVBF and VBF are the UV and visible blocking filters. L1, L2 and L3 are lenses. A1: iris diaphragm. PMT: Photomultiplier tube. DAQ: data acquisition unit. PC: personal computer. 44

3.3 A cross-section schematic diagram of the poling cell used to achieve domain invertion in $LiNbO_3$ crystal. A high voltage (HV) just above the coercive field of the crystal is applied across the crystal via the water electrodes. The O-ring are used to contain the water in between the crystal and the insulating material 45

4.1 Crystal-fixed axes (x, y, z) relative to the laboratory-fixed axes (X, Y, Z). θ and φ are the incident and the azimuthal angles. p and s are the polarization of the beam, as described in the text. 48

4.2 The open triangle symbol shows the experimental results of the RSHG rotation anisotropy for s,s input, output polarization and the error bars shows a 1δ standard error of the experimental data. The solid line is the fitted curve using equation (3.31). $\theta = 60^o$. 49

4.3 The open circle symbols show the experimental results of the RSHG rotation anisotropy for p,p input, output polarization and the error bars shows a 1δ standard error of the experimental data. The solid line is the fitted curve using equation (3.29). $\theta = 60^o$. 51

4.4 The open square symbols show the experimental results of the RSHG rotation anisotropy for s,p input, output polarization and the error bars shows a 1δ standard error of the experimental data. The solid line is the fitted curve using equation (3.30). $\theta = 60^o$. 52

4.5 Rotation anisotropy results for domain inverted samples from both $+z$ and $-z$ of z-cut $LiNbO_3$ with: (a) $\gamma = p$ and $\Gamma = p$, (b) $\gamma = s$ and $\Gamma = p$, and (c) $\gamma = s$ and $\Gamma = s$. The solid lines are the fitted curves obtained by using equation (3.32), respectively. The plane of incidence lies along 90^o and 270^o line. 55

4.6 Possible physical operations to achieve inversion of a system with mirror planes along the yz plane. (a) and (d) are the coordinate system and the $LiNbO_3$ atomic arrangement in a virgin state. (b) Shows the coordinate system rotated by 180^o around the y-axis $(C_2(y))$ from the virgin state. (c) Shows the coordinates system rotated by 180^o around the x-axis $(C_2(x))$, which is similar to the inversion of the whole crystal. (e) $LiNbO_3$ atomic arrangement following domain inversion. 57

4.7 (a) The labeled y-axes with the + z direction pointing out of the page and also showing the direction of rotation. (b) RSHG curves with the global maximum value ($\varphi = 30^o$) corresponding to the alignment of the + y_3 direction along the + X direction. The SHG signal was normalized to the value at ($\varphi = 30^o$) and the error bars are calculated as in the previous figures in this chapter. 58

4.8 (a) The labeled y-axes with the $-z$ direction pointing out of the page (b) RSHG curves with the local maximum value ($\varphi = 30^o$) corresponding to the alignment of the $+y_3$ direction along the $+X$ direction. The SHG signal was normalized to the value at ($\varphi = 90^o$) and the error bar are calculated as in the previous figures in this paper. 59

4.9 (a) The labeled y-axes with the -z direction pointing out of the page. (b) RSHG curves with the global maximum value ($\varphi = 30^o$) corresponding to the alignment of the $-y_2$ direction along the $+X$ direction. The SHG signal was normalized to the value at ($\varphi = 30^o$) and the error bars are calculated as in the previous figures in this paper. 61

4.10 Inset diagram shows the schematic top-view of a half re-poled $LiNbO_3$ sample. SHG results from the + z face of the virgin part (filled circles) and - z face of the poled area (open circles). The SHG signal was normalized to the value at ($\varphi = 90^o$)and the error bars are calculated as in the previous figures in this paper. 62

4.11 A schematic picture showing the domain inverted area and the virgin area on a domain inverted sample. Two spots were selected from the two areas for the collection of the RSHG data as a function of time 64

4.12 SHG signal vs the time after the sample was poled. The y-axis was placed parallel to the incidence plane and $\gamma = s$ and $\Gamma = p$. 65

4.13 SHG vs time after the sample was poled. The x-axis was placed parallel to the incidence plane. 67

5.1 a) geometrical layout of a ring resonator in general parameters, b) multimoded ring resonator confining 12, 8 and 6 bounces laterally coupled to a multimoded input and output bus 75

5.2 Typical normalised intensity profile from port B (dotted line) and port C (solid line) as a function of the wavelength at different output coupling constants ($\zeta_b = \zeta_a = 0.1$ and $\tau = 0.98$ calculated using equations (5.6,5.5), respectively. $R = 20\mu m$ and $n_{eff} = 3.2$. 77

5.3 Cavity Q-factor and waveguide output intensities at resonance ($\lambda = 1550nm$) as a function of the input coupling coefficient for a lossy ($\tau = 0.98$) ring resonator with $R = 20\mu m$ and $n_{eff} = 3.2$ and $\zeta_b = 0.1$. From the left, the first vertical dotted line (A) marks symmetric coupling while the second one (B) shows critical coupling. 78
5.4 lateral coupling for (a) ring resonator, (b) vertically coupled ring/disk microcavity and (c) hexagonal resonator 79
5.5 Schematic top view of a waveguide-coupled hexagonal microcavity. A bus waveguide of width W_b is displaced from the flat side of the hexagonal microcavity by a distance g_1. Both the cavity and the bus waveguide, with refractive index n_g are immersed in a background medium with refractive index n_s. $k_{wg}(k_{cav})$ is the waveguide (cavity) mode propagation vector. Capital letters A and B denote, respectively, the input and output port of the device 80
5.6 Yee lattice used for FDTD unit cell 85
5.7 Effect of the PML layer on the wavefunction along the propagation direction. The PML starts from $x = 5$ by making $\sigma_x(x < 5) = 0$ and $\sigma_x(x > 5) > 0$ 88
5.8 2D schematic layout of the hexagonal microcavity in the FDTD simulation. The launch position of the incident beam is located at the center of the width of the detection monitor as shown by a red arrow representing the k vector of the launch mode 90
5.9 Cavity response for s-polarized FW in a cavity with incident $\lambda = 0.959\mu m$ and $\alpha = 2.97\mu m$, FSR = 49 nm 92
5.10 Schematic top view of a regular and a corner-rounded hexagonal microcavity 93
5.11 Curve fitting for the Q factor determination as a function of the corner rounding. The numbers within the area of the graph are of the corresponding cavity rounding 94
5.12 Dependence of the Q-factor on the rounding of the hexagonal corners for $\alpha = 2.97\mu m$ 95
5.13 Resonance wavelength shift as a result of the rounding of the hexagonal corners for $\alpha = 2.97\mu m$ 96
5.14 FSR as a function of the rounding for $\alpha = 2.97\mu m$ 97
5.15 Numerical simulation of the regular hexagonal microcavity at resonance with $\alpha = 2.97\mu m$ and $\lambda_o = 0.960\mu m$. Top: intensity build-up within the cavity until steady state is reached. Bottom: Steady state mode field pattern showing increased scattering at the corners of the cavity. 98
5.16 Cavity modes for hexagon microcavity with different rounding $\alpha = 2.97\mu m$ 99

5.17 Cavity modes for hexagon microcavity with different rounding $\alpha = 2.97\mu m$ 100

6.1 Hexagonal superstructure achieved by etching poled z-cut, $LiNbO_3$. The -z face etches away while the $+z$ face remains unetched when the crystal is immersed in an HF:HNO_3 acid mixture [3] 103
6.2 Growth of the SH along the propagation length within a nonlinear crystal. PPM: perfect phase matching in a single domain crystal. $I2\omega$ in this figure is normalized to that of PPM. QPM: first-order QPM in a periodically poled crystal and NPM: non-phase-matched interaction see ref [4]. TIR-QPM: total internal reflection-QPM see text and ref [5, 6]. For TIR-QPM, the overall phase matching occurs not necessarily at at l_c but at a length (l_1) where the Fresnel phase shift balances the dispersion phase shift 105
6.3 Schematic diagram demonstrating the TIR-QPM technique within a parallel plate device 107
6.4 Hexagonal cavity showing schematic resonance propagation of both the FW and SH. $n_{g,\omega}$ and $n_{g,2\omega}$ are the refractive indices of the material experienced by FW and SH respectively 109
6.5 Plot showing the dependence of the cavity resonances of the FW, SH, TIR-QPM condition and the ideal condition on the cavity dimension α. The ideal cavity size is therefore at $\alpha^m = 2.98\mu m$ for $\lambda = 0.959\mu m$ 111
6.6 Plot showing the dependence of the global phase shift on the cavity size. Three ideal cavity sizes are shown at $\alpha_1^m = 2.98\ \mu m$, $\alpha_2^m = 12.73\ \mu m$, and $\alpha_3^m = 22.35\ \mu m$ i.e, all the solutions in figure 6.5 belong to the first lobe in this figure while the other lobes show the location of the other ideal cavity sizes. The dashed line represents the global phase shift. 112
6.7 FDTD simulation α scan results for $\lambda^\omega = 0.959\mu m$ and for $\lambda^{2\omega} = \frac{\lambda^\omega}{2}$. $\alpha_1^m = 2.98\mu m$ because it is at this value that $\alpha^{2\omega} \approx \alpha^{2\omega}$. 113
6.8 The cavity response for both FW and SH at a moderate ideal cavity size of $\alpha_2^m = 13.95\ \mu$m. The power output is normalized to that of SH at steady state 115
6.9 A curve fitting to the power profile for the FW within a hexagonal microcavity to determine the cavity loss per round trip for an deal cavity size of $\alpha_2^m = 13.95\ \mu$m $b = 0.33$. 116

6.10 Estimated SH growth for a regular hexagon with no rounding, for $\lambda = 0.955\mu m$ with $\alpha_2^m = 13.95$ μm.r is a reflection coefficient. The total length of a linear devices used to estimate the SH growth for PPM and QPM is $3N\alpha = 1.25mm$. For $r = 100\%$, the TIR-QPM in a hexagonal cavity greater than that from PPM method for an equivalent length. For $r = 99\%$ N_{SH}^{max} is limited to about 15 round trips before the SH signal starts to degrade down toward that of NPM 118
6.11 Growth of the SH with the rounding of the hexagonal corners, for $\lambda = 0.955$ μm with $\alpha = 13.95\mu m$. 119

7.1 PPTi:LN ring resonator for nonlinear applications 122
7.2 A schematic flow diagram for the production of the Ti in-diffused $LiNbO_3$ planar waveguide 123
7.3 Pictures of the designed photomasks with the waveguides and the periodic hexagonal patterns 128
7.4 A schematic diagram for a prism coupling setup used for the determination of n_{eff}. BS = beam splitter 130
7.5 Optical micrograph of the developed SU 8 photoresist patterns on a Ti:$LiNbO_3$ planar waveguide before dry etching 133
7.6 SEM micrograph of the developed SU 8 photoresist patterns on a $LiNbO_3$ substrate before the dry etching 134
7.7 SEM micrograph of the etched $LiNbO_3$ substrate Ti:$LiNbO_3$ waveguide before and after they were chemically etched by concentrated HF acid . . . 135
7.8 SEM micrograph of the dry etched Ti:$LiNbO_3$ waveguide 136
7.9 Planar TM modes at 632.8 nm for different Ti film thickness (τ) and dwell time (t). See table 7.2 138
7.10 Planar TE modes at 632.8 nm for different Ti film thickness (τ) and dwell time (t). See table 7.2 139
7.11 n_e index profile at 632.8 nm and 1550 nm for τ=100 nm and t= 6 h extracted from slab mode solver. 140
7.12 Modes and single mode at 632.8 nm and 1550 nm, respectively. for τ=100 nm and t= 6 h extracted from slab mode solver. 141
7.13 Single mode at 1550 nm for τ=130 nm and t= 13 h obtained using the BPM solver. 142

List of Tables

2.1 Parameters for the Sellmeier equation [7] 26

3.1 Escape length calculation for $\lambda = 266nm$. Data obtained from ref[8, 9] . . . 33

4.1 Summary of the rotational anisotropy results 48
4.2 Values of φ_0 determined from the curve fitting procedure 50
4.3 Summary of the RSGH results for both faces of the virgin $LiNbO_3$ for *s, p* . 60

7.1 Possible values of p, m and R for a given $n_{eff}(1.55\mu m) = 2.1551$ 125
7.2 Summary of the Ti film thickness used and diffusion time 129
7.3 Summary of the measured n_{eff} of the planar Ti:$LiNbO_3$ at $\lambda = 632.8$ nm . 137

Chapter 1

Introduction

1.1 Objectives

This thesis is divided in to two parts. The first part focuses on the use of the reflection SHG technique to study the properties of a poled and non-poled $LiNbO_3$ crystal, and is presented in Chapter 3 and Chapter 4. In this study the SHG technique is used achieve four goals which are: (1) to reveal the symmetry of the $LiNbO_3$ crystal, (2) to compare the amplitudes of the SHG signal from both z faces of the poled part of the $LiNbO_3$ crystal to the un-poled part, (3) to investigate the state of the direction of the y-axis after poling, and (4) to monitor the relaxation of the internal field of the crystal following the poling process.

The second part of this thesis focuses on the use of microcavities to enhance the SHG with a micro-dimension device using $LiNbO_3$/-waveguide as a platform, and is presented in Chapter 6 and Chapter 7. In this study the enhanced power of the resonating fundamental mode in the microcavity is used to enhance power of the induced SHG within a small volume of the device, as a means of creating smaller devices which can compete with the conventional longer-length devices such as PPLN. The aim is to initially demonstrate the potential of such devices numerically and thereafter to fabricate them for practical demonstration.

Two geometries of the microcavity are considered namely, hexagonal and circular shaped microcavities. A Hexagonal-shaped microcavity is selected based on the fact that micro-structures with this geometrical shape are easily made from $LiNbO_3$ via chemical etching after poling of the material. In this hexagonal geometrical shape, phase matching between the fundamental and the second harmonic waves can be achieved via total internal reflection quasi-phase-matching. In the circular microcavity, phase matching is achieved via periodic poling along the ring. In the circular geometrical shape, further

enhancement of the FW is achieved due to the high mode confinement through the use of a waveguide as compared to the use of the bulk material. In the circular micro-cavity a waveguide form, as opposed to the bulk material, is used to give rise to a high confinement to further enhances the FW.

1.2 Introduction and Summary of Chapters

Nonlinear processes such as SHG have a quadratic dependence on the intensity of the fundamental wave (FW) (I_ω), the total length of interaction during propagation (l) and the nonlinear coefficient $\chi^{(2)}$ (i.e $I_{2\omega} \propto (I_\omega l \chi^{(2)})^2 \ \mathrm{sinc}^2(\frac{1}{2}\Delta k l)$). The SHG process is carried out in two geometries: reflection and/or transmission. In the transmission geometry, the fundamental electromagnetic radiation is allowed to propagate through the nonlinear active, medium along which the second harmonic signal is generated from the FW. The conversion efficiency of the SH from the FW relies on $\chi^{(2)}$ and the interaction of the SH and FW within the medium. Materials with large values of $\chi^{(2)}$, such as lithium niobate ($LiNbO_3$) will generally have a high SH conversion efficiency. Chapter 2 of this thesis summaries the properties of $LiNbO_3$ crystal, as this material is used as a platform for all our proposed work.

In transmission geometry however, the inherent dispersion of the nonlinear medium forces the fundamental and the harmonic waves to propagate through at a different phase velocity leading to phase mismatch ($\Delta k \neq 0$) between the two waves. This phase-mismatch results in the degradation of the generated SH signal and hence compromises on the conversion efficiency.

To counter this phase matching problem several methods were put into practice. These methods included special alignment of the polarization angle and the incident angles of the FW relative to the crystallographic geometry of the nonlinear medium, to force the FW and SH beams to travel at the same velocity throughout the crystal. These methods include the so called birefringent phase matching, also called the Perfect Phase Matching (PPM) [10, 4] and the Total-Internal-Reflection Quasi-Phase-Matching (TIR-QPM) [10, 11, 5]. Another method involved spatially flipping the spontaneous polarization (P_s) after each coherence length, so as to reset the velocity mismatch at every coherence length along the propagation length. This later method is called the Quasi-Phase-Matching (QPM) [4] and it is largely applied to ferroelectric methods such as $LiNbO_3$ thanks to the electric field (EF) poling techniques of inverting a volume of

P_s. With these methods, nonlinear optical processes such as SHG have since been of technological importance which brought about devices such as the frequency doubler crystal used in lasers and periodically poled lithium niobate (PPLN) used for optical parametric oscillation.

Following the EF poling technique, destructive methods such as chemical etching are often employed [12, 3],using the differential etching property between opposite z faces, to reveal the quality of the poling in $LiNbO_3$ materials. This has since called for alternative, non destructive methods for post-poling analysis of the poled materials [12, 13, 14, 15, 16, 17]. In the first part of this work, studies have been undertaken to investigate to examine the possibility of using SHG in reflection mode as a tool for domain visualization after poling.

In reflection mode, the incident fundamental beam(s) are reflected from the surface of the medium and the SH is generated within a few atomic layers of the medium and it emerges together with the reflected FW from the medium. Reflection SHG (RSHG) has been widely employed for surface studies even in a centrosymmetric medium, where there is no bulk SHG but where there is surface SHG due to surface discontinuity which induces nonlinearity. For a non-centrosymmetric material like $LiNbO_3$, the bulk signal is trapped inside the crystal via the use of the UV absorption of the medium. Within the surface limit, the SHG properties are very much dependent on the properties of the surface, which in general is different from that of the bulk. Also, it can be expected that, within a certain limit of the surface range (depth of the surface), the z- faces of a poled and nonpoled material should result in different magnitudes of the second harmonic signal (SH). Chapter 3 investigate a detailed theory and the model governing generation of SH, together with the experimental setup for our RSHG work.

In chapter 4, RSHG is used to study various properties of the interfacial layer such as the symmetry, the magnitudes of the SH from both polar faces of the crystal and the behaviur of the y-axis after the inversion of the z-axis of the z-cut $LiNbO_3$ crystal. After poling, the NLO tensor coefficients of the crystal may be different from that of the virgin sample and they may relax back to the original value after a suitably long period of time [18, 19, 20]. Also in this chapter, we investigate this relaxation after poling with the use of RHSG.

In optical applications, such as optical communications, the integration of different optical components is required. In this integration, size and packaging of optical com-

ponents plays an important role in the practicality of the final devices. Optical cavities with micrometer dimensions, termed optical microcavities, have therefore attracted much research attention for their inclusion and role in integrated optical circuits. Microcavities have been used for various applications such as micro lasers, optical filters, and non-linear devices [21, 22].

In chapter 5 we focus our attention on optical microcavity devices with the potential for use in nonlinear applications such as nonlinear frequency generation. Intensity-dependent nonlinear optical processes such as all-optical switching have shown efficiency improvements due to the enhancement of the fundamental power in the cavity which resulted in the reduction of the required switching power in semiconductor microcavities [23]. The motivation behind this work, outlined in chapter 6 and 7, is to utilise the signal stored at resonance within the cavity to enhance the efficiency of the nonlinear optical process.

In chapter 6, we propose the generation of a SH, in a hexagonal microcavity made from single crystal lithium niobate, via TIR-QPM [24]. In chapter 7, we propose creating a periodic inverted domain structure along the circumference such that the light propagating along this path length experiences a constant domain period.

Chapter 2

Summary of the Physical and Chemical properties of crystalline Lithium Niobate

2.1 Introduction

Lithium niobate ($LiNbO_3$) is a multifunctional material due to its wide of properties, such as ferroelectric, pyroelectric, piezoelectric, photorefractive properties, and because it has high linear and nonlinear coefficients. This material has been utilized throughout this work in surface second harmonic generation (SSHG) in chapter 3-5, for modeling the generation of SHG in hexagonal microcavities in chapter 6-7 and for as a platform for fabrications of nonlinear microring cavities in chapter 8. Therefore a summary of its general properties is appropriate and these are outlined in this chapter.

2.2 Crystal Structure

$LiNbO_3$ is a synthetic crystal and its main constituents are Li^+, Nb^{5+} and O^{2-}, as shown in figures 2.1 and 2.2. The Li^+ and Nb^{5+} cations are six-fold coordinated with O^{2-} anions and these anions are further four-coordinated with Li^+ and Nb^{5+} [1]. $LiNbO_3$ belongs to a trigonal lattice system, it has a three fold symmetry relative to the crystallographic c-axis and mirror planes along each of the three equivalent y axes which together makes it to belong to the $3m$ point group. Like any other material belonging to the trigonal system, lithium niobate can be described via either the hexagonal (see figure 2.1 and 2.2) or the rhombohedral unit cell, with six or two formula weights per unit cell, respectively. In the

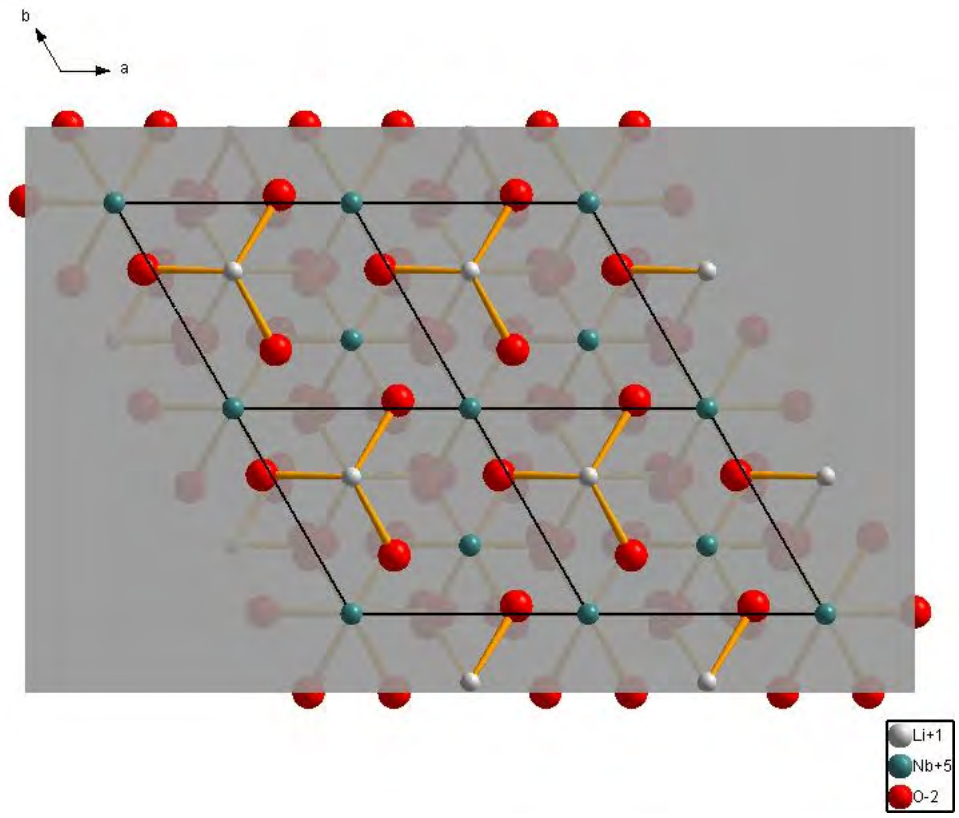

Figure 2.1: Top view of the hexagonal unit cells of $LiNbO_3$ outlined by the solid black lines. In the standard conversion $a = b \equiv x$ and $c \equiv z$ and the y axis is taken to be normal to the xz plane. The mirror planes are along the y-axis [1]. The picture is reproduced using Diamond 3.1d software.

hexagonal unit cell, as outlined in figure 2.2, the crystal contains three equivalent $a = b$ axes (a_1, a_2, a_3) all in a plane perpendicular to the c axis and perpendicular to the mirror planes. The conventional hexagonal axes become (a_1, a_2, a_3, c). From room temperature to within the Curie temperature, $T_c \approx 1400K$ depending on the crystal composition, it maintains its rhombohedral structure with space group of $R3c$. Its structure is made of distorted oxygen octahedra (LiO_6, NbO_6 and vO_6, where v is a vacancy) interconnected by sharing their corners, faces and edges along different crystallographic directions.

The physical properties of lithium niobate are described by Cartesian coordinates $(x, y$ and $z)$ rather than the crystallographic axes $(a, b$ and $c)$. The adopted standard relation between the two is as follows, z is parallel to the c and the x is along the hexagonal a_i axes where $i = 1, 2, 3$ and then the y is the axis normal to the xz plane. Thus the y axis is along the mirror planes. The polarity of the axis is defined as follows,

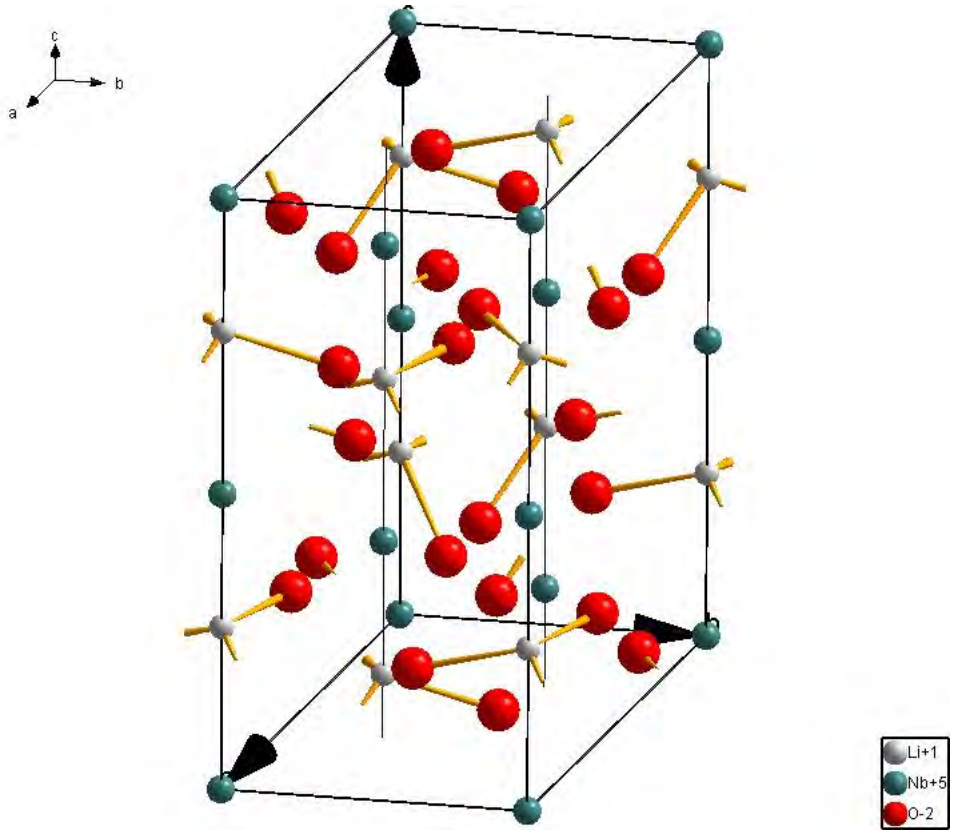

Figure 2.2: Hexagonal unit cell of $LiNbO_3$ [1]. Picture reproduced using Diamond 3.1d software

the $+c$ axis is defined as that c face that generates a positive charge upon cooling [25]. As the generated charge is based upon the resulting net charge appearing on the face per relative displacement of atoms, the polarity of the face can also be described by the order of the cation along the z axis. Figure 2.3 shows the x-cut face of $LiNbO_3$. From this figure, the cation order along the z axis from the $+z$ to the $-z$ face is $\ldots$, Nb^{5+}, Li^{+}, v Nb^{5+}, Li^{+}, $\ldots$. Careful examination of figure 2.3 reveals that the polarity of the y-axis can also be defined using the order of the cation along the y-axis. The distorted cation from the $+y$ to the $-y$ axes is $\ldots$, Nb^{5+}, Li^{+}, v, Nb^{5+}, Li^{+}, $\ldots$.

2.3 Stoichiometry

$LiNbO_3$ exists over a range of compositions from a near stoichiometric value ($X = \frac{[Li]}{([Li]+[Nb])} \approx 50\%$) to lithium-deficient compositions as low as $X \approx 45\%$ (see figure 2.4). $LiNbO_3$ is normally grown via the Czochralski technique, in which a $LiNbO_3$

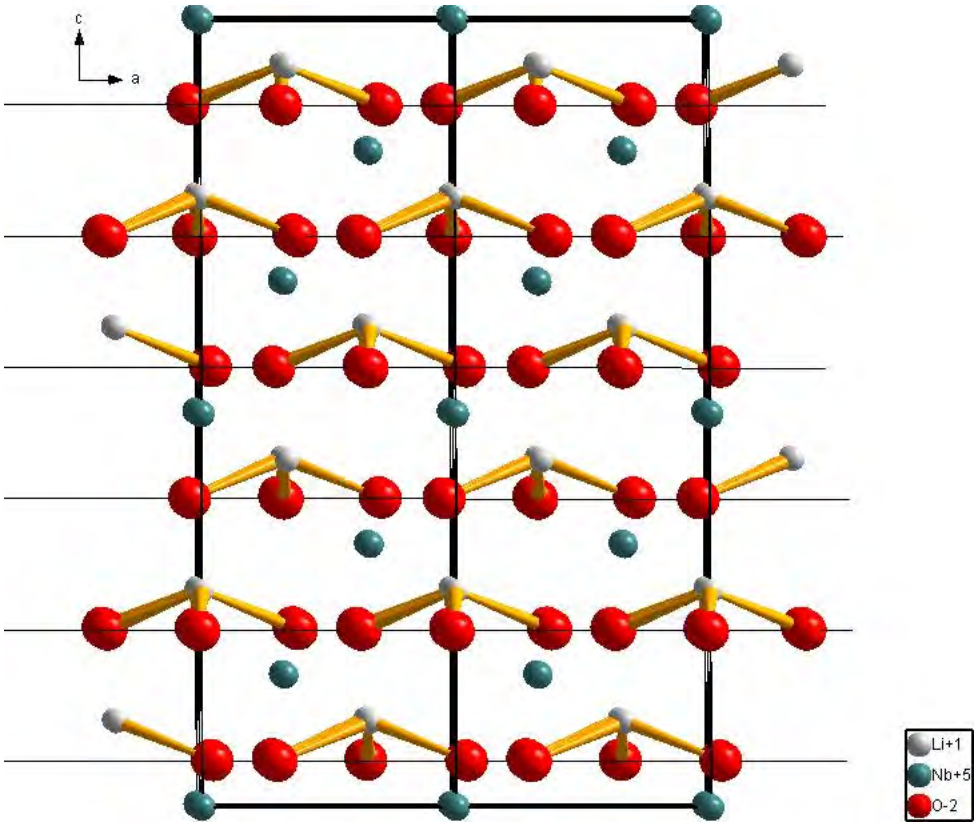

Figure 2.3: Hexagonal unit cell of $LiNbO_3$ showing the x-cut face. The oxygen planes along the y-axis are denoted by the black horizontal lines. The order of the metallic ions in between oxygen lines along the y-axis is found to be ..., Nb^{5+}, Li^{+}, v, Nb^{5+}, Li^{+}, ...going in one direction while the order along the anti-direction, along the y-axis, is found to be ..., v, Li^{+}, Nb^{5+},v, ...[1]. Picture reproduced using Diamond 3.1d software

seed crystal is attached to a rod and dipped in to a platinum crucible containing a high purity molten mixture of Li_2O and Nb_2O_5 compounds held at a temperature just above the melting of $LiNbO_3$. As the rod is rotated at a desired speed and pulled out of the melt at the optimum rate, the seed initiates new growth of the $LiNbO_3$ crystal from within the melt. Normally an electric field is applied along the crystal to force a monodomain formation as the crystal is cooled. Domains are defined as the volume containing P_s pointing along one direction and the separations between the domains are referred as domain walls. Crystals belonging to the trigonal system can only have 180^o oriented domains. Hence, the resulting $LiNbO_3$ crystal has its domain aligned along the z-axis. Because of the forced polarization of the domain during growth, the crystal is said to be poled. However, the crystal can be poled gain later after growth during domain engineering. To distinguish between the two poling stage, the crystal poled during growth is referred as the *virgin* crystal, while the post-growth domain inversion is simply termed

poling and the resulting sample are said to be poled.

A more reproducible, commonly grown and commercially readily available crystal is made from the congruent melt, with $X = 48.4\%$, because it is made from a Li_2O and Nb_2O_5 melt of equal composition. The ease of forming congruent $LiNbO_3$ can be attributed to the weaker Li-O bond, as compared to the stronger Nb-O bond, thus in the case of cation substitutions competition during growth, the weaker bond would be easily broken. Since Li^+ and Nb^{5+} have an equivalent ionic radius there is more chance that Nb^{5+} can replace Li^+ and form a stable compound than the converse unless excess Li^+ is used during growth. The melt percentage composition of less than 50%, leaves room for two kinds of defect inclusion, intrinsic (*nonstoichiometric*) and extrinsic defects within the crystal. Intrinsic defects include antisite defects, in which a cation has occupied another cation's position, for example Nb^{5+} on Li^+ site ($Nb^{5+}_{Li^+}$), Nb^{5+} on the structural vacancy Nb^{5+}_v, Li^+_v, a lithium vacancy (v_{Li^+}), a niobium vacancy ($v_{Nb^{5+}}$) and oxygen vacancies [26].

v_{Li^+} and $Nb^{+5}_{Li^+}$ seem to be some of the most important intrinsic defects as they can be considered to have a higher concentration than others in congruent $LiNbO_3$. Most of the extrinsic defects seem to prefer the position v_{Li^+} and $Nb^{+5}_{Li^+}$ first. Most of the $LiNbO_3$ properties, such as T_c, P_s, refractive index n, nonlinear coefficient (NLO) and coercive field,E_c, depend mostly on X and hence on $[v_{Li^+}]$ [27, 28, 29]. It has been shown that although P_s, NLO, n and T_c decrease in magnitude with $Nb^{+5}_{Li^+}$ and extrinsic defects (Ex) on the niobium site $Ex_{Nb^{5+}}$, the change is more sensitive to $Nb^{+5}_{Li^+}$ than to $Ex_{Nb^{5+}}$ (i.e the change in P_s was found to be much steeper with $Nb^{+5}_{Li^+}$ than with $Ex_{Nb^{5+}}$) [27].

Extrinsic defects such as Fe, Mg and other elements are also present in the melt in a trace concentration. As they are not meant to be there, they normally occupy the position of the intrinsic defects and that of the actual elements. They are normally suppressed during growth of the material by using very high purity starting materials. However, as they vary the properties of the material (high [Mg] reduces optical damage for example), they are sometimes included as dopants during or after growth, to modify the properties of $LiNbO_3$.

Thus, intrinsic defects give a window for the incorporation of dopants within the material leading to titanium indiffusion for the formation of Ti:$LiNbO_3$ waveguides [30, 31]. Holmes and Smyth[32] have shown that the diffusivity of Ti within $LiNbO_3$ decreases with increasing Li content. Thus, Li rich crystals will require more time for the Ti to diffuse through during waveguide fabrication. On the other hand, some of

crystal's properties that depend mostly on the Li-O bonds, such as the d_{33} nonlinear coefficient which increases with increasing Li content, are compromised [28]. The value of the nonlinear coefficients increases as the value of X increases toward a stoichiometric value.

From the above discussion, a trend in the crystal parameters is expected from congruent to stoichiometric crystals. Some of the trends will be discussed below.

2.4 Properties

2.4.1 Paraelectric Phase

For temperatures above T_c but below its melting point (T_m = 1526K) see figure 2.4, $LiNbO_3$ attains a paraelectric phase in which case it loses most of its practical value because it becomes centrosymmetric, with a space group $R\bar{3}c$, and hence it is no longer polar. In the paraelectric phase, the Li^+ and Nb^{5+} move to an average position along the z axis at the centre of the oxygen triangle and the center of the two oxygen layers, respectively. All odd rank tensor properties such as 1^{st} rank P_s, 3^{rd} rank r_{ijk} electro-optic effect and d_{ijk} nonlinear optical effects disappear. Also, the paraelectric phase occurs at a very high temperature, in a range which is not of practical importance to our application in this work, and hence we do not dwell on the crystal's properties in this phase.

2.4.2 Ferroelectricity

As the temperature of the sample is reduced below T_c, the Li^+ moves away from the centre of the oxygen triangle while the Nb^{5+} is displaced away from the center of the oxygen layers. These cations move in the same directions. The charge separation due to the displacement of the cations relative to the oxygen octahedra induces a P_s along the direction of the shift of the cations making $LiNbO_3$ become a ferroelectric material. Ferroelectric materials are those that contain P_s and for which the direction of the P_s can be switched between equivalent states. For $LiNbO_3$ which contains P_s along the z axis, the direction of P_s can be switched to point either along the $+z$ or $-z$ in a single domain via a processes called domain inversion. For domain inversion to occur, the Li^+ needs to move from the other side of the oxygen triangle through to the other side while the Nb^{5+} needs only to shift from the one half of the oxygen layer to the other. The large radial size of the oxygen ion ($R_{O^{2-}} = 1.40$ Å) is bigger than that of the lithium ion ($R_{Li^+} = 0.68$ Å) which inhibits the Li^+ from easy motion through the oxygen triangle. A large electric

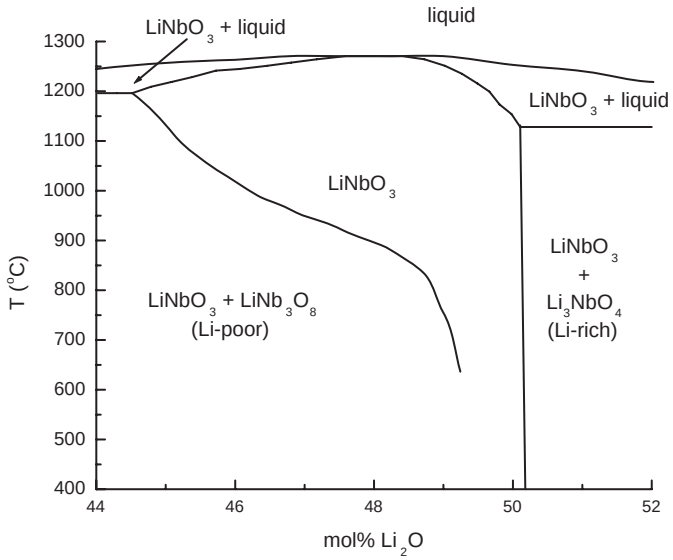

Figure 2.4: Phase diagram of lithium niobate (after [2])

field is required to force the Li^+ to pass through the oxygen triangle unless the crystal is heated to $T \approx T_c$ or the size of the oxygen ion within the crystal is temporarily reduced.

The ferroelectric property of $LiNbO_3$ arises from the displacements (Δz) of the homopolar metallic cation along the polar direction (z axis), i.e. the ion associated with the driving mechanism of the phase transition. At temperatures below T_c, ferroelectric parameters such as P_s and T_c of the material can be related to the homopolar displacement. For a displacive-type ferroelectric such as $LiNbO_3$, the universal relation between ferroelectric parameters, extracted from a least squares technique, given as [12]

$$T_c = 2.00\times10^4(\Delta z)^2(K\mathring{A}^{-1}) \tag{2.1}$$

$$P_s = (258)(\Delta z)^2(\mu C cm^{-2}\mathring{A}^{-1}) \tag{2.2}$$

$$T_c = (0.303)(P_s)^2(\mu C cm^{-2})^{-1}K \tag{2.3}$$

In equation 2.2, Δz is in Å T_c in K and P_s in $\mu C cm^{-2}$. For $LiNbO_3$, $\Delta z \approx 0.269$ Å and $P_s = 71\ \mu C cm^{-2}$ [12]. These equations are useful also for predicting ferroelectric parameters for new displacive-type ferroelectric materials.

For a temperature less than T_c, P_s is parallel to the crystal's $+z$ axis. To reverse

the direction of P_s, an $E-$ field more than the coercive field, E_c, is applied along the polar direction to induce the displacement of the cations along this direction. E_c can be considered as the one holding the material constituents at their respective location.

2.4.3 Domain Inversion in $LiNbO_3$

As seen from figure 2.5, domain reversal requires Li^+ to move through an oxygen layer into the vacant site, leaving behind the vacant site, while Nb^{5+} just shifts from the upper half of the center to the lower half within the same oxygen sandwich. The outcome is that, what used to be a positive z face in the virgin state becomes a negative z face in the poled state and the order of the atoms along the z axis is reversed in the two states.

Domain inversion also results in the reversal of the order of the cations along the y axis. From figure 2.5, the order of the cations along the y axis in between the oxygen sandwich appears to be reversed in the poled state from the original state. Thus after poling, what used to be a $+y$ face becomes a $-y$ face and vice versa. The inversion of the y axis due to the inversion of the z axis has been confirmed experimentally via the use of the technique surface second harmonic generation to be described in chapter 3 [33]. Since the x axis is normal to the mirror planes, the direction of this axis remains the same after poling.

Domain inversion has been achieved via several techniques as described in a review by Houe and Townsend [34]. Poling in $LiNbO_3$ crystal can be achieved by the application of a small electric field whilst cooling the crystal through T_c. At T $\approx T_c$, the Li^+ is on average within the oxygen triangle, hence only a small electric field is required to push the ions in a desired direction to achieve domain inversion. This method is more suitable for achieving single domain in the crystal during growth but it can also be applied after the crystal has been grown. One major drawback of this method is that it requires the crystal to be held at a high temperature which limits its application to bulk crystals as waveguide can degrade at this high temperature.

Fast electrons or X-ray radiation incident on the crystal has been shown to assist the Li^+ to pass through the oxygen triangle and hence can be used for domain inversion. This is made possible by a reduction in the radius of the oxygen ion upon being ionized by the applied radiation. As the Li^+ is already close to the oxygen layer to start with, once the crystal is irradiated and the oxygen is ionized, it will take only a small electrical field to force the Li^+ through even at temperatures much lower than T_c within a shot period of time (on the picoseconds scale). Poling on waveguides has been achieved via

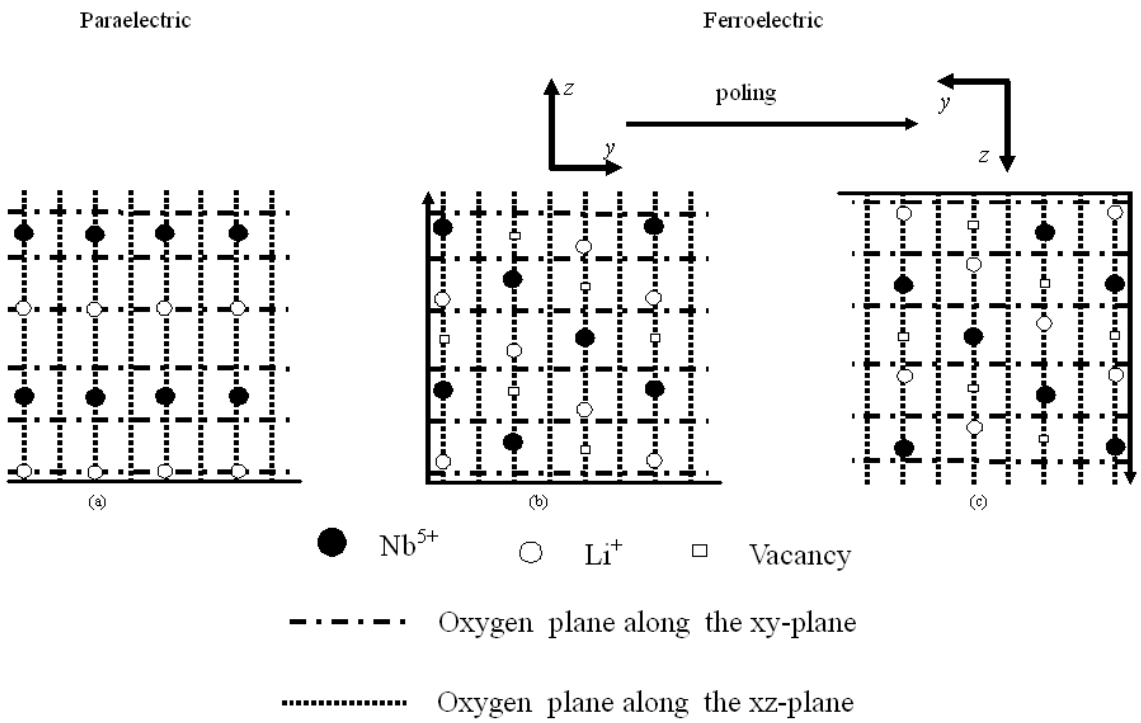

Figure 2.5: x-cut face of the virgin and poled $LiNbO_3$ crystal. In the poled state, the order of the cations in between the oxygen layers both along the z and the y axis appears to be reversed.

this method with the use of a 10 keV electron beam scanned onto the crystal through the mask and with an application of a small external electric field of 10 Vcm^{-1} at 580 ^oC [35]. Domain inversion with this method can be achieved either on the $+z$ or $-z$ face by choosing suitable direction for the applied electric field. Scanning Electron Microscopes (SEM) have also being used to achieve both 1D and 2D periodic poling on the $-z$ face of both $LiNbO_3$ crystals and Ti:$LiNbO_3$ without the application of an external electric field [36, 14]. With the SEM method of poling, only the $-z$ face was poled while the $+z$ face was earthed via a deposited metal coating.

As the temperature of the $LiNbO_3$ crystal is raised toward T_c, Li_2O out-diffusion occurs mostly from the $+z$ face which results in local decomposition of $LiNbO_3$ to $LiNb_3O_8$ (see figure 2.4)[2]. If part of the $+z$ face is covered, a controlled out-diffusion occurs on the $+z$ face and this method has been used to induced periodic poling [37]. The resulting domain inversion is thought to be due to the local structural variation due to the out-diffusion which results in a lower T_c than that of the non-out-diffused part and hence domain inversion can occur. The resulting domain wall attains a triangular shape with a

30^o angle. If the $+z$ face is not periodically covered, at high temperature an uncontrolled local domain inversion occurs and this can causes problem for waveguide application such as undesired variation of the refractive index. For this same reason, $LiNbO_3$ waveguides fabricated at high temperature for non linear applications are limited to the $-z$ face.

The poling electric field is inversely proportional to the temperature. At room temperature, the required poling field is large and the field is normally pulsed on the crystal to avoid permanent damage on the sample [38]. In general, the electric field poling (EFP) technique relies on applying an electric field larger than E_c across the sample for a short period of time. For congruently grown $LiNbO_3$, $E_c \approx 22kV/mm$. Once reversed, the domain can also be reversed again, *reversed* poling, but this time with less field required than that for the *forward* poling [39]. The anisotropy is brought about by the presence of positive internal field, E_{in}, which itself is due to the presence of nonstoichiometric point defects within the sample [40]. In the virgin state of the crystal, E_{in} is parallel to the z axis and it does not follow completely the P_s motion unless annealed at a temperature above 150 ^oC. As a result the required field to achieve *reversed* poling is $E_c - E_{in}$, compared to the *forward* poling which is $E_c + E_{in}$ [18].

2.4.4 Pyroelectric Properties

This is an effect in which the net dipole moment per unit volume within a medium changes with a change in temperature (ΔT). For ferroelectric materials, the pyroelectricity is present when P_s changes with ΔT. The relationship between ΔP_s and ΔT is linear and can be written as $P_s = \eta_i \Delta T$, where η_i is the pyroelectric coefficient. In uniaxial materials such as $LiNbO_3$, where P_s lies only along the z-axis, $\eta_i = \eta_z$ where $\eta_z = -4 \times 10^{-5} C K^{-1} m^{-2}$ [25]. We do not use these properties in this work but they affect the control of handling the crystal during fabrication, as uncontrolled changes in temperature can lead to the formation of surface domains.

2.4.5 Piezoelectric effect

When $LiNbO_3$ is subjected to stress (σ_i), a polarization (P_i) is induced. P_i is linearly proportional to the applied stress and can be written in a tensor form as $P_i = \sum d_{ijk}\sigma_{jk}$ where $i, j, k = x, y, z$ and d_{ijk} is the third rank piezoelectric tensor [25]. By the application of the intrinsic permutation, symmetry constraints and Neumann's principle (see chapter 3), the 27 elements of d_{ijk} are reduced to 18. Due to a further symmetry constraints of the crystal on d_{ijk}, there are only four independent piezoelectric coefficients $d_{113} =$

Table 2.1: Parameters for the Sellmeier equation [7]

	$i = o$	$i = e$
A_0	4.5312×10^{-5}	3.9466×10^{-5}
λ_o	223.219	218.203
A_1	2.7322×10^{-5}	8.3140×10^{-5}
λ_1	260.26	250.847
A_{IR}	3.6340×10^{-8}	3.0998×10^{-8}
A_{UV}	2.6613	2.6613
μ_0	2.1203×10^{-6}	7.5187×10^{-6}
μ_1	-1.8275×10^{-4}	-3.8043×10^{-5}

$d_{131}, d_{222}, d_{311}$ and d_{333} of the possible 18 coefficients. This effect is also not used in this work.

2.4.6 Sellmeier equation and refractive index

Nearly all the properties of $LiNbO_3$ depend on its refractive index. $LiNbO_3$ is a negative uniaxial material which implies that, in its transparency range, its ordinary refractive index (n_o) is greater than the extraordinary refractive index n_e. $LiNbO_3$ is a dispersive material and also its index depends on the composition within the medium. A general form for representing n_i, from the infra-red to the UV range, is via the Sellmeier equation where the composition, the frequency and in some cases the temperature dependence are treated as variables [7, 41, 29]. A general Sellmeier equation for $LiNbO_3$ can be written as [29]

$$\begin{aligned} n_i^2 &= \frac{50 + c_{Li}}{100} \frac{A_{0,i}}{(\lambda_{0,i} + \mu_{0,i}F)^{-2} - \lambda^{-2}} \\ &+ \frac{50 - c_{Li}}{100} \frac{A_{1,i}}{(\lambda_{1,i} + \mu_{1,i}F)^{-2} - \lambda^{-2}} \\ &- A_{IR,i}\lambda^2 + A_{UV} \end{aligned} \tag{2.4}$$

where c_{Li} is the mol % of Li_2O, λ is the wavelength in nm and $i = e, o$. $F = f(T) - f(T_0)$ is the temperature factor where $f(T)$ is given as [7]

$$f(T) = (T + 273)^2 + 4.0238 \times 10^5 \left[coth\left(\frac{261.6}{T + 273}\right)\right] \tag{2.5}$$

where T is in ^oC. The parameters used in equation (2.5) are shown in table 2.1.

The above general Sellmeier equation is only valid from the far infra red up to the UV region. In the far UV range, above 5.3 eV, pure congruent $LiNbO_3$ is very absorptive

[9, 42]. Also above 5.3 eV, congruent $LiNbO_3$ losses its birefringent properties. The absorption edge can be shifted more in the UV range via the incorporation of the desired (doping) defects such Mg [42]. The linear refractive index of $LiNbO_3$ can be changed locally, from that described by the Sellmeier equation (2.5), by local doping with material such as Ti, H or Zn for waveguide production. Due to their low diffusivity, Ti indiffusion is normally limited to the surface. We will return to the details of Ti:$LiNbO_3$ in the subsequent chapters when dealing with waveguide production.

2.4.7 Photorefractive effect

The photorefractive effect is the ability of the crystal to change its local refractive index under high exposure to intensity laser beam. Normally, such an effect is not desired, such as in the case of waveguides where precise control of n is needed, then this effect is called *optical damage* while in the case of holographic devices, where the effect is used to induce memory within the crystal, dopants are used to increase the photorefraction.

Extrinsic defects such as Fe, Cu and Rh in congruent $LiNbO_3$ result in an intermediate energy level in between the valence and the conduction energy band. The electrons in the intermediate energy level can be optically excited, via a long exposure of laser beam with correct energy, causing them to migrate into the conduction band leaving behind holes. Once in the conduction band photo-induced electrons can diffuse through the crystal to a region where the intensity is low. The spatially local redistribution of photo-induced charges between the valence, impurity and conduction energy level set up a local space charge field, E_{sc}. E_{sc} results in a change in the refractive index via the electro-optic effect (see the next section).

Photorefraction is a combination of a bulk photovoltic effect (appearance of a short circuit current through the material when illuminated with light) and electro-optical effects [25]. In $LiNbO_3$, ions of iron, for example which are normally present as Fe^{2+} and Fe^{3+} act as electron donors and acceptors respectively and higher [Fe] results in an increase of the photorefraction. The presence of Fe^{2+} and Fe^{3+} is indicated by the absorption band at around 2.6 eV which is due to the $Fe^{2+} - Nb^{5+}$ intervalance transfer and the red shift in the absorption edge starting at around 3.1 eV due to the $O^{2-} - Fe^{3+}$ charge transfer. These photorefraction effects can be initiated by long exposure of photons with $\lambda \approx 500$ nm, to excite the donor electrons. Cu^{+}/Cu^{2+} ions in $LiNbO_3$ were also demonstrated to induce photorefraction in a similar manner as Fe^{2+}/Fe^{3+} in that they become electron donor and acceptor, respectively, see ref [43, 44].

2.4.8 Reduction of photorefraction

In frequency conversion lithium niobate devices, the crystal is exposed to a high intensity field which can lead to local changes in refractive index if the crystal contains photorefractive enhancing defects such as Fe and Cu. This results in changes in the optical path of the beam and hence a reduced efficiency of conversion. In such cases, a limit in the laser beam intensity is set so as to avoid optical damage via the photorefractive effect.

Attempts have been employed to relax photorefraction, and these include the application of an external field to cancel the photoinduced internal electric field [45], operating the device at a temperature above 170^oC [46] and limiting the operation of the device to a wavelength that lies above the visible range. However, the above conditions do not favour operation of most devices which operate at room temperature and use the near UV and visible region. Another way of relaxing photorefraction is the incorporation of the "so called" photoresistant dopants such Mg, Zn, and Hf. When the concentration of the dopants exceeds a certain value, called the optical damage threshold (ODT), the photoconductivity levels off and the crystal and the material shows enhanced resistance to optical damage.

Below the ODT, it has been shown that the photoresistant dopants occupy the $Nb^{5+}_{Li^+}$ site while above ODT these dopants can replace Nb or Li [31, 47]. Nondoped congruent $LiNbO_3$ can tolerate only up to 10 $kWcm^{-2}$ while the near stoichiometric crystal can take even higher intensity up to 1000 $kWcm^{-2}$ before photorefraction starts to play a role. This is due to the fact that the stoichiometric crystal has fewer intrinsic defects and hence no impurities that can result in photorefraction. ODT in Mg:$LiNbO_3$ is achieved when about 4.6 $mol\%$ of MgO is included in the melt resulting in a 100-fold increase of the optical damage resistance [48]. Zhang *et. al* have grown a Zn doped $LiNbO_3$ (Zn:$LiNbO_3$) from a congruent melt and they have shown an ODT of 6 $mol\%$ of Zn [49]. They have shown that below the ODT, the Zn replaces the $Nb^{5+}_{Li^+}$ while above the ODT it replaces the Li ion. Razzari *et al.* have achieved a lower ODT with 4 $mol\%$ of Hf doping in $LiNbO_3$ (Hf:$LiNbO_3$) [50].

2.4.9 Linear Optical Properties

$LiNbO_3$ exhibits the Pockels effect in which the application of an electric field results in a linear change of the refractive index. The relation between induced refractive index

change and the electric field can be written as [25]

$$\Delta(1/n^2)_{ij} = \sum_k r_{ijk} E_k \tag{2.6}$$

where r_{ijk} is the linear electro-optic coefficient tensor. By the application of the intrinsic permutation, symmetry constraints and Neumann's principle (see chapter 3), the 27 elements of r_{ijk} are reduced to 18 and further to 4 independent elements, and can then be written in a reduced notation as

$$r_{ijk} = \begin{bmatrix} 0 & -r_{22} & r_{13} \\ 0 & r_{22} & r_{13} \\ 0 & 0 & r_{33} \\ 0 & r_{42} & 0 \\ r_{42} & 0 & 0 \\ -r_{22} & 0 & 0 \end{bmatrix} \tag{2.7}$$

The magnitudes of the above coefficient depend on the symmetry and the relative orientation of the octahedra in the crystal structure. For the case of $LiNbO_3$ where $n_e \neq n_o$, so does the change in the refractive index, and equation (2.7) can be written as shown in equation (2.9) for the case where the electric field is applied along the z-axis. $r_{33} \approx 33 pmV^{-1}$ is the largest amongst other coefficient for $LiNbO_3$ and hence Δn_e is the largest with the result that this material is suitable for electro-optical devices such as modulators (see chapter 19 of [51]).

$$\begin{aligned} \Delta n_e &= -\frac{1}{2} n_e^3 r_{33} E_3 \\ \Delta n_o &= -\frac{1}{2} n_o^3 r_{13} E_3 \end{aligned} \tag{2.8}$$

2.4.10 Nonlinear Optical Properties

$LiNbO_3$, like many other ferroelectric materials is a non-centrosymmetric crystal which makes it a possible candidate for nonlinear optical devices which utilize the odd rank polar tensor properties. This was already discussed in the previous section, where a high 3rd rank electro-optic tensor has been shown to be the basis of the electro-optical modulator devices that are made from this material. Another odd rank tensor is the third rank nonlinear optical tensor which governs non linear optical process such as second harmonic generation (SHG). SHG studies and devices constitute the basis of this work and the following chapter deals with these phenomena in more detail.

2.4.11 Microcavities for application in nonlinear optical processes

The effectiveness of the nonlinear processes is limited by the conversion efficiency which itself is limited by the phase mismatch between the fundamental and the harmonic waves. In order to resolve the above limitations multiple parameters must be considered together. One of these parameter concerns the choice of a material with large accessible nonlinear coefficients.

III-V semiconductors like $Al_xGa_{1-x}As$ ($x = 0 - 1$) have a large d_{14} or d_{36} coefficient followed by crystalline materials such as $LiNbO_3$ and MgO:$LiNbO_3$ with a large value of d_{33} [52].

Another parameter to consider address materials properties such as symmetry and dispersion should be compatible with at least one of the phase-matching processes.

Semiconductor materials such as GaAs are very dispersive and isotropic at around 1.55 μm which implies that the phase-matching process involving birefringent is not possible. QPM can be implemented in semiconductors by epitaxial growth and subsequent technological processing. Crystalline materials such as $LiNbO_3$ are ferroelectric and birefringent. This implies that greater choice can be exercised in phase-matching technique

The SH intensity is proportional to the square of the propagation length and also the square of the fundamental intensity. At the same time, integrated optics devices should be small and compact to be compatible with device forming optical circuits such as fiber optics. These requirements call for structures such as microcavites which allow the mode to circulate within the device many times equivalent to a longer length device. Thus, if the above parameters are achieved within such a device then SHG will be further improved.

Microcavity structures such as a micro-ring/disk have requirements of large refractive index contrast for them to be small in radius with minimal bend losses. Small refractive index contrast results in large bend losses for a given radius of the microring hence preventing their small scale fabrication. As an example, semiconductors can have a higher nonlinear coefficients, $d_{36} = 137pmV^{-1}$ [51], and a high refractive index of 3.37 at $\lambda = 1.55\mu m$, which implies there can be small radius microcavity devices of order of $10\mu m$ [53, 54]. Van et al, calculated a bending loss of 0.02 dB/cm for a racetrack resonator with a bending radius of 1 μm made of AlGaAs waveguide [54].

Crystalline materials such $LiNbO_3$ have a moderate refractive index of 2.21 and 2.14 for o and e respectively. Macrocavities using this material will have a radius larger than those of III-V semiconductors for the same optical losses because of the lower refractive index contrast.

For nonlinear applications, this size limitation is not as bad as the SHG is also proportional to the square of the propagation length. We therefore choose to use $LiNbO_3$ as a platform for our microcavity work because of the simple methods available for manipulating $\chi^{(2)}$ and more choice for phase matching processes.

2.5 Conclusion

In this chapter, the physical properties of $LiNbO_3$ were outlined showing why this material has for many years been a subject of both research and applications in electro-optics and related fields. This material, specifically its congruent composition, is commercially available with high purity and less extrinsic defects and hence it serves as a good platform for any research which involves nonlinear optical processes and devices. It is for this reason that this crystal was used throughout this work.

Chapter 3

Reflection Second Harmonic Generation

3.1 Introduction

Within the electric dipole approximation, second harmonic generation (SHG) is forbidden in centrosymmetric media [55], however, at the surface it becomes allowed due to the relaxation of the inversion symmetry. Reflection SHG (RSHG) has been one of the major tools for selective surface studies for a wide range of material interfaces and surfaces [56]. Surface studies such as symmetry determination using SHG are normally achieved, for example, by measuring SHG signals with a well-defined input and output beam geometry, while rotating the sample around the axis normal to the surface. This is feasible since the irreducible components of the second order susceptibility ($\chi^{(2)}$) tensor reflect the symmetry of the medium and hence of the surface. In general, the structural symmetry of the surface and that of the bulk are not the same due to the termination and discontinuity of the bulk symmetrical properties at the interface.

In reflection SHG, the contributing layers to the reflected SHG signal from the top surface has been described as having a thickness $d \approx \lambda$ [57]. The SHG signal generated in the layers where $d > \lambda$ interact destructively. Therefore, for a centrosymmetric medium, the whole $d \approx \lambda$ will contribute to the surface signal therefore making SSHG not a surface sensitive technique. At the same time, the thickness of the surface is not precisely defined, and is normally considered to have a thickness of $d << \lambda$. Thus SSHG becomes only surface specific in the limit $d << \lambda$ where the bulk contribution can be neglected in relation to that of that surface.

For non-centrosymmetric materials, the surface selectivity by SHG is limited due

Table 3.1: Escape length calculation for $\lambda = 266nm$. Data obtained from ref[8, 9]

	$n^2 - k^2$	$2nk$	n	k	$\alpha(nm)^{-1}$	$s_{1/e}(nm)$
e	11.3	2.6	3.3620	1.680	0.079	12.6
o	8.44	1.3	2.9064	1.452	0.069	14.6

to the inherent contribution from the bulk. It has been shown that with suitable selection of the input and output beam polarization and the azimuthal angles, the SHG contribution from the bulk and the surface can be separated [58]. This method is however not applicable for the determination of the symmetry of the interfacial layer where the azimuthal or the polarization angles must be varied.

Below the Curie temperature, the combination of several properties of $LiNbO_3$ such as ferroelectricity, high nonlinearity and high optical damage threshold has lead to the use of this crystal in many technological applications such as quasi phase-matching (QPM). With ferroelectric materials, QPM devices are made by periodic reversal of P_s and hence reversal of the domain. For $LiNbO_3$, ($\mathbf{P}_s$) is along the z-axis and hence its reversal implies the reversal of the z-axis ($+z \Leftrightarrow -z$). Within the surface limit, the SHG properties are very much dependent of the state of the surface which in general is different from that of the bulk. Also, it can be expected that within a certain limit of the surface range (depth of the surface), the two z- faces of a z-cut material should in results in different magnitudes of the second harmonic signal (SH).

$LiNbO_3$ exhibits high UV absorption hence the penetration of UV light is restricted to within a few hundred atomic layers in this material. Thus for $LiNbO_3$, surface selectivity using RSHG can be achieved by selecting a fundamental beam in the visible range and hence a SHG beam in the UV which must therefore originate from the top outer-most atomic layers. At $\lambda = 266nm$, the absorption coefficients ($\alpha = 4\pi k/\lambda$) is ≈ 0.08 nm^{-1} and 0.07 nm^{-1} for ordinary and extraordinary rays, respectively, where k is the imaginary part of the complex refractive index [9]. The intensity of the beam propagating within the medium is given by $I = I_0 e^{(-\alpha s)}$ where I_0 and s are the incident intensity and the propagation length. The SHG generated after a length $s_{1/e}$ where $I = I_0/e$, will effectively be absorbed and hence will not contribute to the reflected SHG signal.

At 266 nm, both ordinary and extraordinary polarized light can only propagate for a $1/e$ distance of $s_{1/e}$ 15 nm [8, 9]. Any SHG signal generated deeper than the interfacial layer will be absorbed by the bulk and will not contribute to the observed reflected signal. This layer is, however, thicker than what is usually considered as the surface (a few tens of atomic layers) and therefore it is called an interfacial layer. The difference between this

layer and the surface is that its optical properties are similar to that of the bulk while in general they differ from that of the surface. Thus the observed RSHG will include signals from both the surface and this interfacial layer.

This chapter and the following one contains the work in which RSHG is used as a probe to study the changes in the structural symmetry of $LiNbO_3$ upon domain inversion within the crystal. There, RSHG is used as non-destructive probe for the determination of the location and direction of the ferroelectric domain orientation in $LiNbO_3$ crystal. The model governing the generation of the SH within the interfacial layer together with the experimental setup are firstly outlined.

3.2 Theory

Propagation of electromagnetic radiation through a molecular distribution results in the induction of the multipoles within such a medium due to displacements of the molecules from their equilibrium positions. The induced electric polarization (P_α) (dipole moments per unit volume), in component form, is linearly related to the strength of the perturbing field E_β as

$$P_\alpha = \alpha_{\alpha\beta} E_\beta, \tag{3.1}$$

where α and β are taken relative to the molecular-fixed axes. $\alpha_{\alpha\beta}$, the polarizability tensor, is the constant of proportionality relating the induced electric polarization to the inducing field and it is a property of the material. When a laser is used as a source of electromagnetic radiation, due to its light wave field being comparable to the internal field of the crystals [12], an induced electric polarization may result from even higher orders of the incident electric field. To relate the induced polarization to these higher order terms of the inducing field, equation (3.1) can be expressed as a power series in the field strength as

$$P_\alpha = E_\beta(\alpha_{\alpha\beta} + \beta_{\alpha\beta\gamma} E_\gamma + \gamma_{\alpha\beta\gamma\delta} E_\gamma E_\delta + ...) \ . \tag{3.2}$$

Where $\beta_{\alpha\beta\gamma}$ and $\gamma_{\alpha\beta\gamma\delta}$ are the first and the second hyperpolarizability tensors and they describe the deviation of the effective polarizability tensors from $\alpha_{\alpha\beta}$ due to the intense perturbing field. They are responsible, respectively, for the frequency doubling and tripling of the oscillating induced multipoles relative to the frequency of the incident beam. In principle, the induced polarization oscillates at all possible sum and difference frequencies that can be generated from the incident beam [51]. Due to these harmonic terms, the

time variation of the total polarization from equation (3.2) does not necessary vanish. Hence, charges are accelerated and according to Larmor's theorem on electromagnetism, electromagnetic radiation is produced [59]. Polarizabilities and hyperpolarizabilities are directly related to the induced multipoles, i.e related directly to the induced dipoles or/and quadrupole moments within the material [59]. The polarization in equation (3.2) can be written in another form by replacing the polarizabilities and hyperpolarizabilities with the susceptibility of the corresponding order as

$$P_i(t) = \varepsilon_0(\chi_{ij}^{(1)}E_j(t) + \chi_{ijk}^{(2)}E_j(t)E_k(t) + \chi_{ijkl}^{(3)}E_j(t)E_k(t)E_l(t) + \cdots). \tag{3.3}$$

While the polarizabilities give more information about the molecular transition processes occurring within the medium in the presence of electromagnetic radiation, the susceptibility reflects structural properties of the medium. The subscripts (i, j, ...) in the above equation are taken relative to the space-fixed coordinates. While the two forms (equations (3.2) and (3.3)) are directly related, the first one is a *microscopic* picture, but we will use the second form shown in equation (3.3) since it is a *macroscopic* quantity and directly linked to the measurable quantities.

For the purpose of our work as in this thesis, we now wish to concentrate on the second term on the right hand side in equation (3.3), which describes the second order polarization process within the medium and is therefore responsible for SHG processes. SHG is a second-order process in which two photons with frequency ω are converted into one photon which oscillates at twice the incident frequency.
The nonlinear polarization induced within the medium for this case is given in a component form as

$$P_i^{(2)}(t) = \varepsilon_0\chi_{ijk}^{(2)}(-2\omega;\omega,\omega)E_j(t)E_k(t). \tag{3.4}$$

In equation (3.4), the repeated index j and k on the right hand side implies the summation over j and k. The sum of all the frequencies contained in the nonlinear susceptibility terms should be zero to satisfy the conservation of energy [51]. In Fourier amplitudes, the nonlinear polarization due to the SHG process within the medium is given in a component form as

$$P_i^{(2)}(2\omega) = \varepsilon_0\frac{1}{2}\chi_{ijk}^{(2)}(-2\omega;\omega,\omega)E_j(\omega)E_k(\omega). \tag{3.5}$$

Synthesising the model to fit our observed data requires the knowledge of the properties of $\chi_{ijk}^{(2)}$. We therefore spent some time exploring such properties to facilitate our discussions later in this chapter.

3.2.1 Permutation symmetry and spatial symmetry

3.2.1.1 Intrinsic permutation

This fundamental property of the nonlinear susceptibility results from time invariance and causality [55]. It implies the invariance of $\chi^{(2)}_{ijk}(-2\omega;\omega_1,\omega_2)$ under permutation of the pairs $((j,\omega_1)\ ,(k,\omega_2))$ such that

$$\chi^{(2)}_{ijk}(-2\omega;\omega_1,\omega_2) = \chi^{(2)}_{ijk}(-2\omega;\omega_2,\omega_1). \tag{3.6}$$

Intrinsic permutation reduces the number of independent elements of a third rank tensor from 27 to 18.

Spatial symmetry

For a crystal belonging to a known crystal point group or for which a point group can be assumed, the number of elements of $\chi^{(2)}_{ijk}(-2\omega;\omega_1,\omega_2)$ is further reduced due to the constraints imposed on the crystal by Neumann's principle, which restricts the relation between the χ^2 and $\chi^{2'}$ before and after symmetry transformation respectively. Neumann's principle requires $\chi^{(2)'}_{ijk}(-2\omega;\omega_1,\omega_2) = \chi^{(2)}_{ijk}(-2\omega;\omega_1,\omega_2)$ for any symmetry operations belonging to the point group of the crystal [55]. That is, for example, if rotating the crystal by 60^o is an operation belonging to the crystal's point group, then, all the independent $\chi^{2'}$ after this operation should remain the same as before.

For crystals not belonging to the hexagonal class, symmetry operations through the transformation law (see equation (3.14)) result only in reshuffling of the indices and /or sign changing. For these crystals the results of Neumann's principle can be written as

$$\chi^{(2)'}_{ijk}(-2\omega;\omega_1,\omega_2) = \varepsilon_T \chi^{(2)}_{ijk}(-2\omega;\omega_1,\omega_2) \tag{3.7}$$

where $\varepsilon_T = \pm 1$.

If in equation (3.7) $\varepsilon_T = -1$ then that element of $\chi^{(2)}_{ijk}(-2\omega;\omega_1,\omega_2)$ vanishes. Hence, the nonzero and independent elements can be found by inspection of equation (3.7) for any symmetry operation belonging to the point group of the crystal [55]. The method described above is termed direct inspection and only works for crystals not belonging to the hexagonal class [55]. The reduced elements of $\chi^{(2)}_{ijk}(-2\omega;\omega_1,\omega_2)$ for the known crystal point groups are known and tabulated [55] and therefore we will used them as given.

3.2.1.2 Overall permutation and Kleinman symmetry

Unlike the intrinsic permutation, this permutation is an approximation and hence it is not a fundamental property of the nonlinear susceptibility tensor. It is based on the assumption that the medium is transparent over all optical frequencies appearing in the formula for the nonlinear susceptibility.[55]. The permutation is now such that $\chi^{(2)}_{ijk}(-2\omega;\omega_1,\omega_2) \approx \chi^{(2)}_{ijk}(\omega;-2\omega_1,\omega_2)$. It is mostly known as Kleinman symmetry and it encapsulates the intrinsic permutation. It is worth mentioning here that the wavelength of our incident beam is 532 nm, hence its second harmonic (266 nm) lies inside the absorbing region of $LiNbO_3$ [12, 7]. Kleinman symmetry neglects the dispersion property of the medium over all used frequencies [55] and we will not assume Kleinman symmetry in our model formulation. If this permutation holds, the number of independent elements of the third rank tensor is further reduced.

For crystals belonging to the point group 3m, the independent elements of $\chi^{(2)}_{\alpha\beta\gamma}$ found without the assumption of the Kleinman symmetry ($\chi_{xzx} = \chi_{zxx} = \chi_{xxz}$) are shown in matrix (3.8) [55].

$$\begin{bmatrix} 0 & 0 & 0 & 0 & \chi_{xzx} & -\chi_{yyy} \\ -\chi_{yyy} & \chi_{yyy} & 0 & \chi_{xxz} & 0 & 0 \\ \chi_{zxx} & \chi_{zxx} & \chi_{zzz} & 0 & 0 & 0 \end{bmatrix} \tag{3.8}$$

3.2.2 The Three Layer Model for RSHG

We followed the treatment by Zhang *et al.* [60] in which they have considered a three layer slab with layers stacked on top of each other as shown in figure 3.1a. The top layer may be assumed to be air and the SHG is generated by reflection of the beam on top of the second layer. In our case, both the middle layer and the bottom layer are made of $LiNbO_3$ but we argue that the two layers possess some different optical properties in both optical frequencies used. The significance of such a difference between the bottom two layers is also expected to be polarization dependent.

For materials with center of inversion symmetry, surface SHG is generated only from the surface due to the relaxation of the surface symmetry, thus some symmetry properties of the surface and the bulk are different and this is expected to hold whether the material has a center of inversion or not. Within a centrosymmetric material, the detection of the significance of the difference in nonlinear optical properties is made possible by the fact the bulk contribution can be totally minimized. With our approach of using the UV absorption range to separate the bulk and surface contribution in noncentrosymmetric

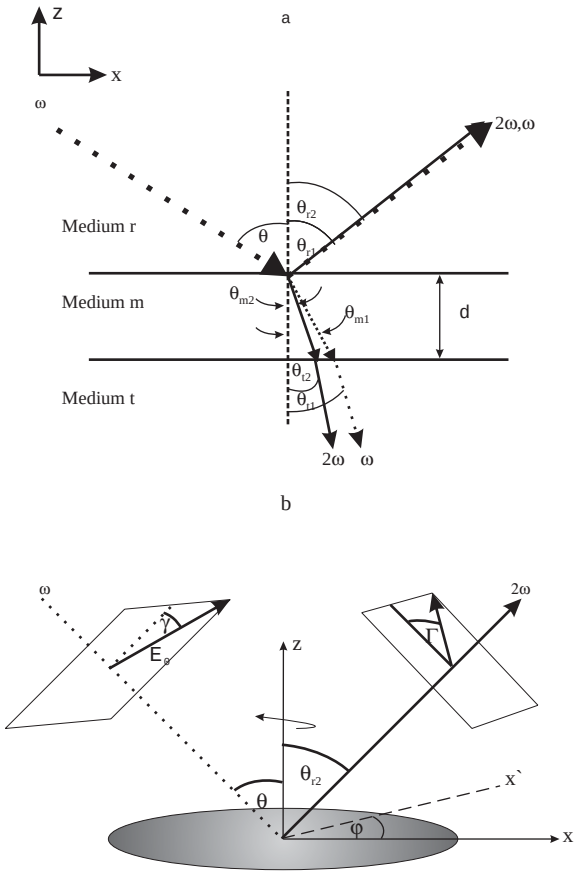

Figure 3.1: a) Three layer model of an interface. Medium r consists of air, while both medium m and t are made of $LiNbO_3$. b) In this figure x' is the new space-fixed coordinate relative to x as the sample is rotated around z by the azimuthal angle (φ). γ and Γ are the input and output polarisation angles respectively. See the text for further details.

material, it should be possible to detect the difference in optical properties between the two layers.

Zhang *et al.* [60] used the middle layer as a monolayer and we consider this layer to be made of the few outermost layers of atoms in our crystal [56]. We denote the linear dielectric constant of the medium as $\varepsilon_{\eta\nu}$, where η and ν refer to the medium (which can be r, m or t) and to the frequency of the beam (1 for ω or 2 for 2ω) respectively. The depth of the middle layer (d) is assumed to be very much less than the wavelength of the fundamental beam.

We take the plane of incidence to lie in the zx plane such that the yx plane is parallel to the plane of the slab. As shown in figure 3.1, γ and Γ are used to denote the angles of

the planes of polarization for the fundamental and the generated SHG beams respectively. These two polarization angles are measured relative to the plane of incidence. We use p and s to denote the polarization angles at 0^o and 90^o, respectively relative to the plane of incidence.

The components of the electric field of the beam in the medium (m) are related to γ and the fundamental field as

$$\begin{vmatrix} E_x \\ E_y \\ E_z \end{vmatrix} = \begin{vmatrix} a\cos(\gamma) \\ c'\sin(\gamma) \\ b\cos(\gamma) \end{vmatrix} \mathbf{E_0}, \tag{3.9}$$

where a, b, and c' are Fresnel coefficients given as

$$a = \frac{2\sqrt{\varepsilon_{r1}}\cos(\theta_{r1})\cos(\theta_{t1})}{(\sqrt{\varepsilon_{t1}}\cos(\theta_{r1}) + \sqrt{\varepsilon_{r1}}\cos(\theta_{t1}))} \tag{3.10}$$

$$b = \frac{2\sqrt{\varepsilon_{r1}}\cos(\theta_{r1})\sqrt{\varepsilon_{t1}}\sin(\theta_{t1})}{\sqrt{\varepsilon_{m1}}(\sqrt{\varepsilon_{t1}}\cos(\theta_{r1}) + \sqrt{\varepsilon_{r1}}\cos(\theta_{t1}))} \tag{3.11}$$

$$c' = \frac{2\sqrt{\varepsilon_{r1}}\cos(\theta_{r1})}{(\sqrt{\varepsilon_{t1}}\cos(\theta_{t1}) + \sqrt{\varepsilon_{r1}}\cos(\theta_{r1}))} \tag{3.12}$$

The boundary conditions

$$\sqrt{\varepsilon_{r1}}\sin(\theta) = \sqrt{\varepsilon_{r1}}\sin(\theta_{r1}) = \sqrt{\varepsilon_{m1}}\sin(\theta_{m1}) = \sqrt{\varepsilon_{t1}}\sin(\theta_{t1}) \tag{3.13}$$

are used to relate the angles of refraction and reflection of the fundamental beam in equations (3.11-3.12) to the incident angle (θ).

In most cases, such as this one, one may wish to vary the azimuthal angle (φ) in which the sample is rotated around its facial normal. With this in mind we relate the elements of $\chi^{(2)}_{ijk}$ to φ. For a z-cut surface, the rotational matrix containing the cosine direction angles required for the transformation of $\chi^{(2)}_{mno}$ into $\chi^{(2)'}_{ijk}$ by [55]

$$\chi^{(2)'}_{ijk} = R_{im}R_{jn}R_{ko}\chi^{(2)}_{mno} \tag{3.14}$$

when the sample is rotated from (mno) to (ijk) is given as

$$\mathbf{R} = \begin{bmatrix} \cos(\varphi) & \sin(\varphi) & 0 \\ -\sin(\varphi) & \cos(\varphi) & 0 \\ 0 & 0 & 1 \end{bmatrix} \tag{3.15}$$

The coordinates mno (i.e. $m = x'$ in figure 3.1b) and ijk refer to the space-fixed axes and they share the same origin. We have assumed a non-vicinal surface (small offset of

the crystal cut), hence the normal of the surface is always parallel to the z-axis of the crystal. If the surface is vicinal, one needs to introduce a further 3×3 matrix to correct for the small offset relative to the plane perpendicular to the incident plane [61, 62]. The new elements of the second order susceptibility after using equations (3.14) and (3.15) in equation (3.8) are found to be

$$\mathbf{K} = \begin{bmatrix} \chi_{yyy}K_1 & -\chi_{yyy}K_1 & 0 & 0 & \chi_{xxz} & \chi_{yyy}K_2 \\ \chi_{yyy}K_2 & -\chi_{yyy}K_2 & 0 & \chi_{xxz} & 0 & -\chi_{yyy}K_1 \\ \chi_{zxx} & \chi_{zxx} & \chi_{zzz} & 0 & 0 & 0 \end{bmatrix} \tag{3.16}$$

where $K_1 = (-3\sin(\varphi)\cos^2(\varphi) + \sin^3(\varphi))$, $K_2 = (3\sin^2(\varphi)\cos(\varphi) - \cos^3(\varphi))$.

In the electric dipole approximation the second order polarization can be written as [55]

$$\begin{bmatrix} P_x^{(2\omega)} \\ P_y^{(2\omega)} \\ P_z^{(2\omega)} \end{bmatrix} = \tfrac{1}{2}\varepsilon_o \mathbf{K} \begin{bmatrix} E_x^2 \\ E_y^2 \\ E_z^2 \\ 2E_yE_z \\ 2E_zE_x \\ 2E_xE_y \end{bmatrix}. \tag{3.17}$$

Zhang *et al.* [60] assumed that $\frac{d}{\lambda} \ll 1$ and used the results of Bloembergen and Pershan [57] to arrive at the expression for the p ($\Gamma = 0$) and the s ($\Gamma = \pi/2$) components of the SH field reflected from medium r layer as

$$E_p^{(2\omega)} = -4\pi i \frac{\omega d}{c} \frac{(-1)(\sqrt{\varepsilon_{t2}/\varepsilon_{m2}})\sin(\theta_{m2})P_z^{(2\omega)} + \cos(\theta_{t2})P_x^{(2\omega)}}{(\sqrt{\varepsilon_{t2}}\cos(\theta_{r2}) + \sqrt{\varepsilon_{r2}}\cos(\theta_{t2}))}, \tag{3.18}$$

$$E_s^{(2\omega)} = 4\pi i \frac{\omega d}{c} \frac{P_y^{(2\omega)}}{(\sqrt{\varepsilon_{t2}}\cos(\theta_{t2}) + \sqrt{\varepsilon_{r2}}\cos(\theta_{r2}))}. \tag{3.19}$$

where the so far undefined symbols have their usual meaning. By substituting the results of the operation in equation (3.17) into both (3.18) and (3.19), the latter two equations can be written as

$$\begin{aligned} E_p^{(2\omega)} &= (A\cos^2(\gamma) + B\sin^2(\gamma) + C\sin(2\gamma))E^2 \\ E_s^{(2\omega)} &= (F\cos^2(\gamma) + G\sin^2(\gamma) + H\sin(2\gamma))E^2 \\ E_{\pm 45}^{(2\omega)} &= \tfrac{1}{\sqrt{2}}\left(E_s^{(2\omega)} \pm E_p^{(2\omega)}\right) \end{aligned} \tag{3.20}$$

where the coefficients A, B, C, F, G and H are found to be

$$A = S_1 \left[\sqrt{\frac{\varepsilon_{t2}}{\varepsilon_{m2}}} \sin(\theta_{m2})(a^2\chi_{zxx} + b^2\chi_{zzz}) + \cos(\theta_{t2})(a^2 K_1 \chi_{yyy} + 2ab\chi_{xzx}) \right] \tag{3.21}$$

$$B = S_1 \left[\sqrt{\frac{\varepsilon_{t2}}{\varepsilon_{m2}}} \sin(\theta_{m2}) c'^2 \chi_{zxx} - \cos(\theta_{t2}) c'^2 K_1 \chi_{yyy} \right] \tag{3.22}$$

$$C = S_1 \left[2\cos(\theta_{t2}) a c' K_2 \chi_{yyy} \right] \tag{3.23}$$

$$F = S_1 \left[a^2 K_2 \chi_{yyy} \right] \tag{3.24}$$

$$G = S_1 \left[c'^2 K_2 \chi_{yyy} \right] \tag{3.25}$$

$$H = S_1 \left[2c' b \chi_{xzx} - 2ac' K_1 \chi_{yyy} \right] \tag{3.26}$$

where

$$S_1 = \frac{8\pi\omega i d}{c(\sqrt{\varepsilon_{t2}}\cos(\theta_{t2}) + \sqrt{\varepsilon_{r2}}\cos(\theta_{r2}))} \tag{3.27}$$

The above equations have a similar form to those found by Mejia *et al* [63] for a 3m point group, but with a slight difference in that we get an odd dependence of the anisotropic term on the azimuthal angle whereas they get an even dependence and the opposite is true. The linear dielectric constants at the second harmonic frequency in equations (3.21-3.26) can be related to the incident angle by similar boundary conditions as in equation (3.13) and by using $\theta_{r1} = \theta_{r2}$. Using the law of reflection $\theta_{r1} = \theta$ the boundary conditions at the second harmonic frequency are written as

$$\sqrt{\varepsilon_{r1}}\sin(\theta) = \sqrt{\varepsilon_{r2}}\sin(\theta_{r2}) = \sqrt{\varepsilon_{m2}}\sin(\theta_{m2}) = \sqrt{\varepsilon_{t2}}\sin(\theta_{t2}). \tag{3.28}$$

We can make a non-dispersion assumption in equations (3.13) and (3.28) for the linear dielectric constant in air (medium r) and equate them to unity. As we have been avoiding Kleinman's conjecture, we cannot make such an assumption for the pair of dielectric constants in both medium m and t. It is very tempting however to equate the dielectric constant at a specific frequency for these last two layers, but doing so will overrule our argument about some different properties between them.

From equation (3.20) one can then fit the intensity of the SHG as a function of γ at a fixed Γ and φ to determine the coefficients, for the surface under investigation, in equations (3.21 - 3.26) from the polarization dependence measurements at a fixed θ. From these coefficients, statistical methods can be used to determine the relative components of $\chi^{(2)}$ for the surface. However, this extraction of the components requires the knowledge

of the dispersive dielectric constant at the surface. We have assumed that the dielectric constant of the bulk and of the surface are not necessarily the same. This assumption is made complex by the definition of the surface due to the fact that, as the surface becomes thicker, the difference between these dielectric constants will become small. At the same time, it is hard to limit the thickness of the surface. As result, we do not attempt to extract these components of $\chi^{(2)}$.

For rotation anisotropy measurements, γ and Γ are fixed together with θ, while φ is varied. We show here three equations, determined by inserting equations (3.21 - 3.26) into equation (3.20), to be used to fit the rotation anisotropy results for $\gamma = p$ and $\Gamma = p$ as equation (3.29), $\gamma = s$ and $\Gamma = p$ as equation (3.30) and $\gamma = s$ and $\Gamma = s$ as equation (3.31).

$$E_p^{(2\omega)} = \left(a_1 + a_2(sin^3(\varphi) - 3sin(\varphi)cos^2(\varphi)\right)\left(E_0^{(\omega)}\right)^2 \tag{3.29}$$

where $a_1 = f(n(\omega), n(2\omega), \theta)(\chi_{zxx} + \chi_{zzz} + \chi_{xzx})$ and $a_2 = f(n(\omega), n(2\omega), \theta)(\chi_{yyy})$.

$$E_p^{(2\omega)} = \left(a_1 + a_2(sin^3(\varphi) - 3sin(\varphi)cos^2(\varphi)\right)\left(E_0^{(\omega)}\right)^2 \tag{3.30}$$

where $a_1 = f(n(\omega), n(2\omega), \theta)(\chi_{zxx})$, $a_2 = f(n(\omega), n(2\omega), \theta)(\chi_{yyy})$.

$$E_s^{(2\omega)} = \left(a_1(cos^3(\varphi) - 3sin^2(\varphi)cos(\varphi)\right)\left(E_0^{(\omega)}\right)^2 \tag{3.31}$$

where $a_1 = f(n(\omega), n(2\omega), \theta)(\chi_{yyy})$.

Equations (3.30)−(3.31) can be generalized in a form which distinguishes the contribution of rotationally isotropic terms B' and rotationally anisotropic terms A' as

$$E^{2\omega} = B' + A'K(\varphi) \tag{3.32}$$

B' is a linear combination of the isotropic components of the $\chi^{(2)}$: $\chi_{zxx}, \chi_{zzz}, \chi_{xzz}$, A' is proportional to the anisotropic susceptibility:χ_{yyy}, and $K(\varphi)$ denotes the sine and/or cosine variation of the azimuthal angle in equations (3.30)−(3.31).

The effect of the magnitude of B' relative to that of A' on the azimuthal variation of the SHG signal is known to affect the relative amplitudes and the number of peaks of the observed SHG signal as a function of the azimuthal angle due to the interaction between these terms [64].

We have neglected the bulk contribution in our model formulation since the SHG generated from the bulk will be absorbed for our incident beam (λ =532 nm). If that was not the case, if for example incident wavelength was in the infrared region such that

the generated SHG is outside the absorption region of the crystal, then one may have to use suitable combinations of γ, Γ and φ appropriate for the point group of the crystal to suppress the bulk contribution [58].

In the next chapter, we show the use of the rotation anisotropy measurement to reveal the symmetry of the surface of a $LiNbO_3$ substrate. Also we use this technique to investigate if the two polar faces (+ and $-z$-face) of this crystal give the same SH magnitudes. We further use this method to reveal what happens to the y axis of this crystal after the inversion of the z-axis during the domain inversion process. We now describe our experimental setup used to extract the surface SHG.

3.3 Experimental

3.3.1 RSHG experimental setup

A 532 nm Q-switched Nd:YAG frequency-doubled laser (20 Hz repetition rate, 10 ns pulse width, pulse energy of 2 mJ, Continuum, Minilite) was used as the input beam. Figure 3.2 shows a schematic of the experimental set-up used for the rotation anisotropy measurements. The power of the input beam was controlled by rotation of the $\lambda/2$ plate placed in the beam path between the laser head and the polarizing beam splitter (PBS1). The plane of polarization of the input beam was controlled by rotating the second $\lambda/2$ plate. A beam splitter (BS) was used to direct a small fraction of the input beam into the photodiode (PD) for monitoring the power. The signal from the PD was also used to correct for any fluctuations in the SHG beam caused by any input beam instability. A 20 cm focal length lens (L1) was used to focus the beam to a spot size of ≈ 0.5 mm on the z-cut congruent $LiNbO_3$ sample.

$LiNbO_3$ samples were cut from a wafer purchased from Crystal Technology, USA. A UV blocking filter (UVBF) was placed between L1 and the $LiNbO_3$ to block any SHG signal generated along the optical train before the sample. The sample was held on a rotational stage which allowed the sample to rotate around its surface normal. The incident angle of the beam, θ, was set to be 60^o. A visible blocking filter (VBF) was placed in the path of the reflected beam to block any reflected part of the fundamental beam. The train of optics in both the input and the output paths of the beam was fixed on two separate movable arms which allowed variation of both the incidence and the reflection angles.

The SH was passed through a UV Rochon polarizer (PBS2) for p or s polarization selection. An iris diaphragm, A1, was placed after this polarizer to block any diverted light. The signal was subsequently focused on the slit of a monochromator set to allow

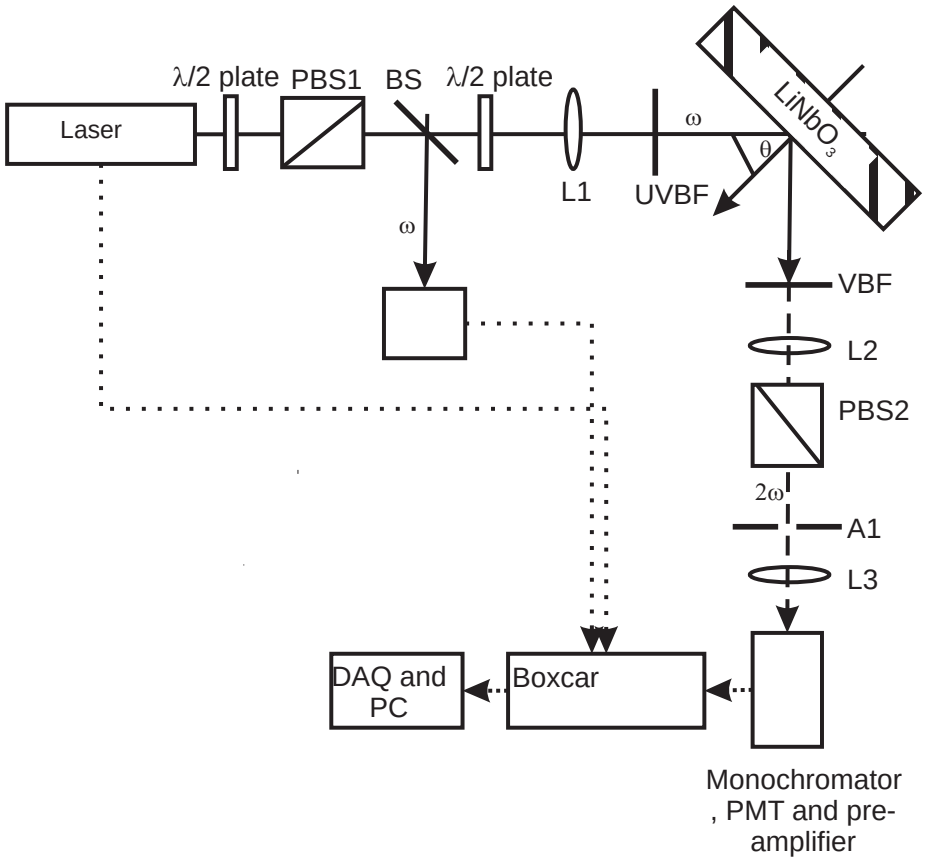

Figure 3.2: Experimental set-up. The dotted line shows the electrical signal path. PBS1 and PBS2 are the input and output polarizer, BS: beam splitter. PD: the photodiode. UVBF and VBF are the UV and visible blocking filters. L1, L2 and L3 are lenses. A1: iris diaphragm. PMT: Photomultiplier tube. DAQ: data acquisition unit. PC: personal computer.

transmission of only 266 nm which was detected by the photomultiplier (PMT). After feeding the signal from the PMT into a preamplifier, the amplified signal and that from the PD were fed into a gate integrator before both were synchronously acquired and analyzed using a data acquisition unit (DAQ) and a personal computer (PC), triggered by the Q-switch signal from the laser.

The crystals used had a slab geometry for which both z face surfaces were parallel. Due to the small thickness ($500\mu m$) and the spot size of the beam, multiple reflections occur between the two z-faces which results in a higher SHG signal being generated. The fundamental beam reflected from the bottom surface thereby generated a secondary SHG signal from the last few atomic layers as it emerged from the top surface. Due to multiple reflections, this contribution from the secondary SHG signal was larger than the

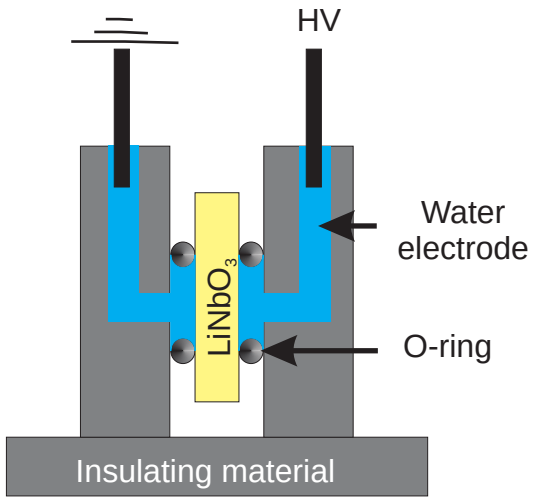

Figure 3.3: A cross-section schematic diagram of the poling cell used to achieve domain invertion in $LiNbO_3$ crystal. A high voltage (HV) just above the coercive field of the crystal is applied across the crystal via the water electrodes. The O-ring are used to contain the water in between the crystal and the insulating material

primary SHG signal, as observed via RSHG. This secondary SH signal was minimized by roughening the bottom surface of the crystal with 600 grit sandpaper.

3.3.2 Poling setup

The crystal was cleaned before being secured in the poling cell shown in figure 3.3. Tap water was used as an electrode material and a high voltage (HV) about 11 kV (the crystal thickness was 500 μm) was applied across the crystal to achieve the reversal of $\mathbf{P}_s$ within an area of the crystal exposed to water. The sample was then removed from the poling cell.

3.4 Conclusion

The theory and the three layer model for the surface second harmonic generation have now been discussed. The three layer model is based on the assumption that the top layer of the $LiNbO_3$ substrate may have different optical properties from that of the bulk. This model will now be used in chapter 4 and 5 where the RSHG technique is used in several specific applications: (1) To reveal the symmetry of the interfacial layer. (2) Used as a non-destructive tool to map the domain-inverted area in the poled $LiNbO_3$ crystals. (3) To characterize the direction of the y-axes following domain inversion. (4) time dependent RSHG is used to study the relaxation of the internal field and point defects within the

crystal following the domain-inversion.

Chapter 4

RSHG: Results and Discussions

4.1 Introduction

In this chapter, RSHG is used to study various properties of the interfacial layer such as the symmetry, the magnitudes of the SH from both polar faces of the crystal and the behavior of the y-axis after the inversion of the z-axis of the z-cut $LiNbO_3$ crystal. This crystal is known to possess a bulk $3m$ point group symmetry, with the x-axis located along the mirror planes. Figure 4.1 shows the relationship between the laboratory and the crystal fixed axes. In this figure the plane of incidence is along the XZ plane. In section 4.2, a sample with a known crystal axis orientation is studied via the RSHG to see if there is any deviation from the known bulk symmetry definition.

For a bulk material, the transmission SHG signal from the -z and +z faces of a polar crystal, such as $LiNbO_3$, is expected to be the same irrespective of which direction the signal is observed from. This is due to the fact that an averaged signal from the bulk is observed. At the surface, one can expect the termination of the -z and +z faces to be very much dependent on the nature of the charge forming a layer just above the surface. This surface termination can in general be different between the two faces. Thus if a signal is obtained from the surface only, the difference in the surface termination can be observed from the SHG signal. If such a difference in signal exists, it is expected to be a function of $(\varphi, \theta, \gamma, \Gamma)$. In section 4.3, θ is fixed while rotational anisotropy investigations are performed at different γ and Γ to see if the two faces, -z and +z face, yield different magnitudes of the SHG signal. In section 4.4, RSHG is used to monitor the orientation of the y-axes following the domain inversion process. In section 4.5, we investigate this relaxation of these point defects that occurs after the forward poling.

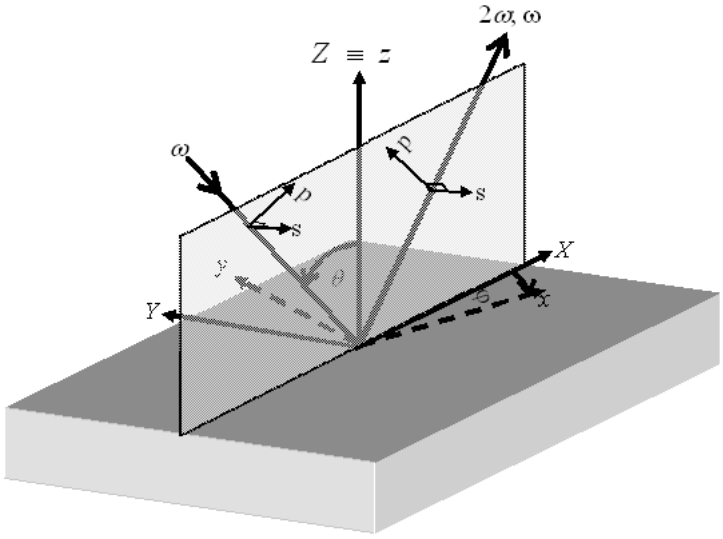

Figure 4.1: Crystal-fixed axes (x, y, z) relative to the laboratory-fixed axes (X, Y, Z). θ and φ are the incident and the azimuthal angles. p and s are the polarization of the beam, as described in the text.

Table 4.1: Summary of the rotational anisotropy results

γ	Γ	Terminology	Figures
s	s	s, s	Figure 4.2
p	p	p, p	Figure 4.3
s	p	s, p	Figure 4.4

4.2 Use of RSHG to reveal the symmetry of the interfacial layer of a z-cut $LiNbO_3$ crystal

Table 4.1 summarizes the rotation anisotropy results on a z-cut $LiNbO_3$ sample. The curves shown in figures 4.2-4.4 have the characteristics of a 3m symmetry with symmetry repetition every 60^o or 120^o over the full 360^o rotation. Each point in these figures is an average of 250 accumulated measurements. The values in figures 4.2-4.3 are normalized to a maximum SHG efficiency value for s,p, (i.e $\gamma = s$, $\Gamma = p$, see also 4.1) shown in figure 4.4.

The same reasoning that is used to account for the bulk SHG null signal in a centrosymmetric medium can be used to put constraints on mirror planes with respect to the plane of incidence. In this case, the SHG signal should vanish when a mirror plane coincides with the plane of incidence, since both the input and output polarizations are perpendicular to the mirror plane. For a 3m material, three mirror planes intersecting each other at 60^o are expected and are clearly represented by the minima in the SHG signal in figure 4.2.

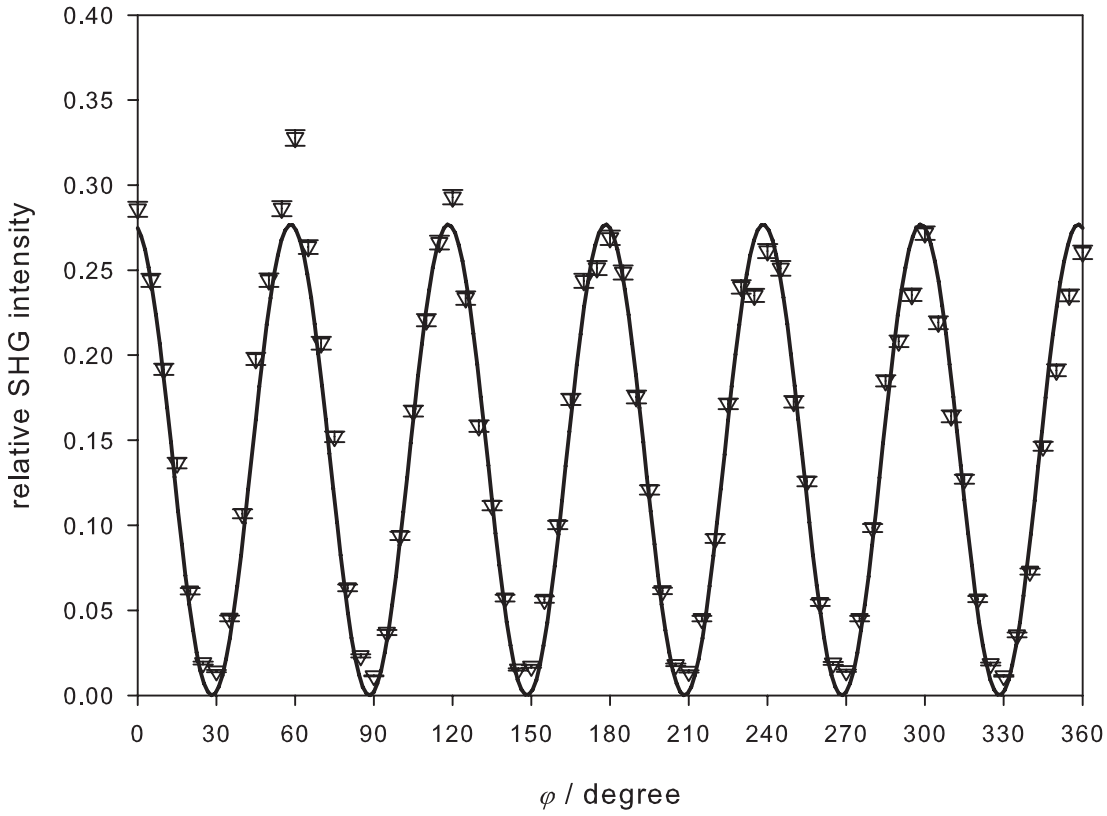

Figure 4.2: The open triangle symbol shows the experimental results of the RSHG rotation anisotropy for s,s input, output polarization and the error bars shows a 1δ standard error of the experimental data. The solid line is the fitted curve using equation (3.31). $\theta = 60^o$.

Table 4.2: Values of φ_0 determined from the curve fitting procedure

	p,p	s,p	s,s
φ_0/degree	-1.9 ± 0.3	-20.0 ± 0.2	-1.6 ± 0.2

By the standard definition of the crystalline axes in $LiNbO_3$ [25], the three equivalent y-axes lie along these mirror planes. With the mirror plane found in figure 4.2, the y-axes locations are determined to an accuracy limited by the azimuthal angle steps chosen. Jung *et al.* [65] have proposed and used $LiNbO_3$ to demonstrate a simple method for the determination of crystalline axes of a non-linear uniaxial crystal via transmission SHG. However, as our underlying motives here are to study intrinsically surface phenomena, we have chosen a reflection-based geometry for our studies.

It was shown in the section (3.2.2) that the rotationally isotropic and anisotropic contributions to the measured SHG signal can be separated as B' and A', respectively. When $|A'| < |B'|$ the isotropic terms dominate and only three major peaks are observed. This result, for the case of p,p is shown in figure 4.3 and is accounted for by the fact that χ_{zzz} for $LiNbO_3$ is the largest coefficient compared to all other components of the $\chi^{(2)}$ tensor, hence making the B' term the largest. As shown in figure 4.4, the magnitude of the isotropic term is reduced compared to that of p,p since there is no contribution from χ_{zzz} and χ_{xzx}, and minor peaks (local maxima) subsequently appear. On fitting the curves for the SHG results, a phase difference was introduced between $|A|$ and $|B|$, as discussed previously by [66]. The phase difference in this case accounts for the different phase contributions between the $\chi^{(2)}$ tensor components in the isotropic and the anisotropic terms in the observed SH signal. The full six-fold symmetry is observed since only an anisotropic term is contributing in this case.

On fitting the curves, φ in equation (3.32) was replaced by $\varphi + \varphi_0$, with φ_0 denoting the offset between the laboratory-fixed axis and the crystal-fixed axis as it was not possible to position the sample on the stage with the required degree of precision. From the curve fitting procedure however, the location of the x and y-axes are thereby determined with the prior knowledge only of the optical axis.

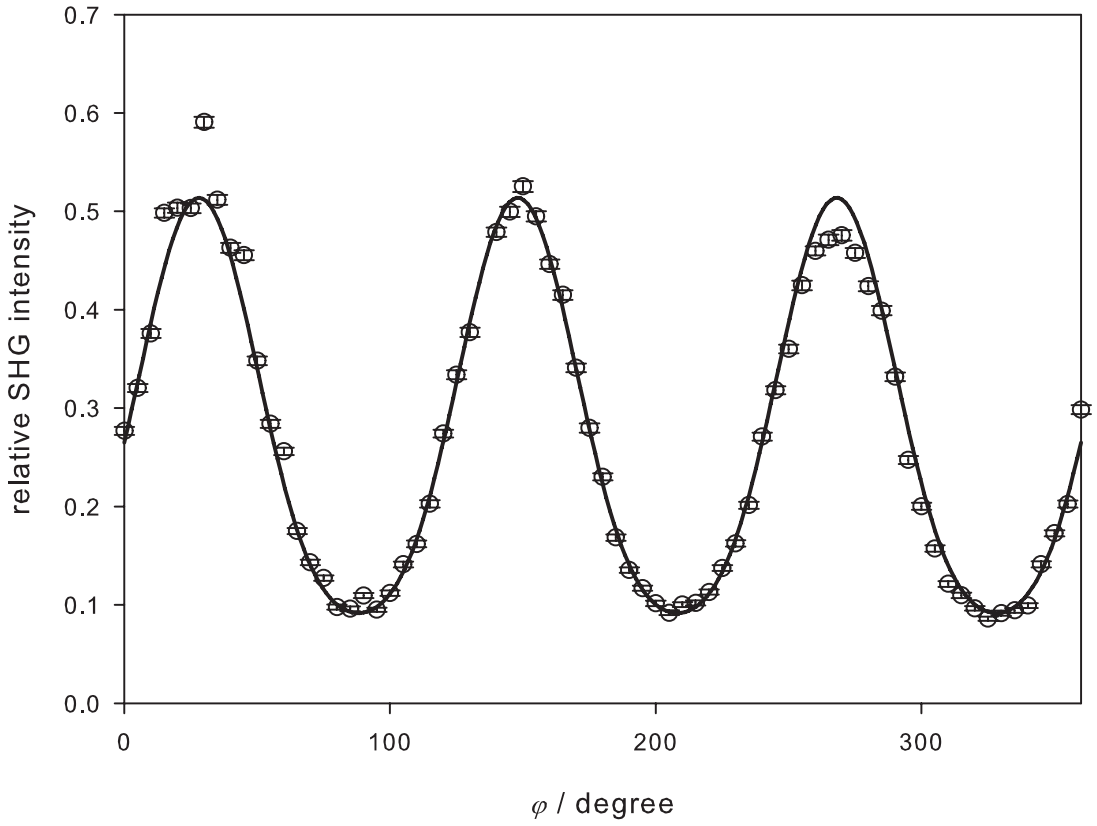

Figure 4.3: The open circle symbols show the experimental results of the RSHG rotation anisotropy for p,p input, output polarization and the error bars shows a 1δ standard error of the experimental data. The solid line is the fitted curve using equation (3.29). $\theta = 60^o$.

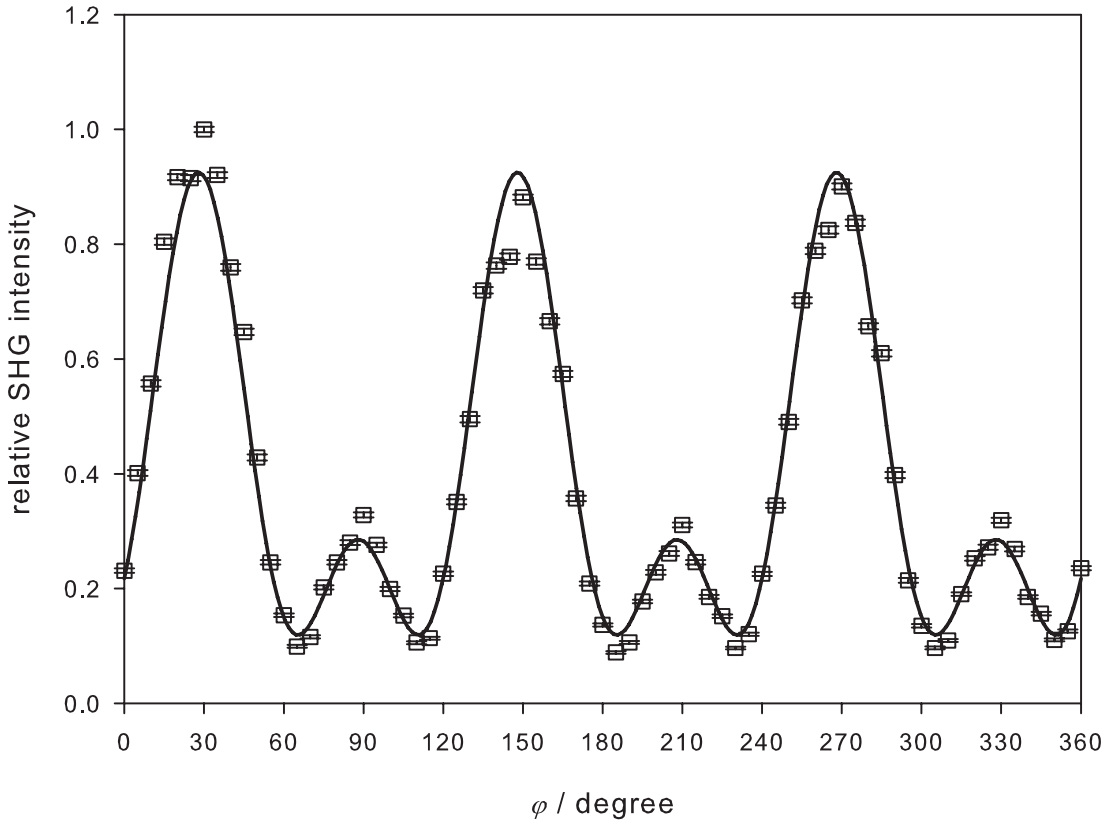

Figure 4.4: The open square symbols show the experimental results of the RSHG rotation anisotropy for s,p input, output polarization and the error bars shows a 1δ standard error of the experimental data. The solid line is the fitted curve using equation (3.30). $\theta = 60^o$.

4.3 Methods for the characterization of the inverted domains

Quasi-phase-matching (QPM), a technique in which the $\mathbf{P}_s$ of the crystal is periodically inverted along the direction of propagation, has led to high efficiency non-linear processes such as SHG. The QPM efficiency is very much affected by the periodicity and the duty cycle. Knowledge of the period and the duty cycle throughout the poled crystal is therefore a primary requirement. The periods of the inverted domain are in the 5-30 μm dimension and hence of their cauterization requires high resolution techniques.

There are several methods used to observe and characterize domains in ferroelectric materials and these include optical birefringence [12], X-ray topography [12, 13], X-ray diffraction (XRD) [14, 15], transmission SHG [12, 16, 17], HF chemical etching [12, 3] and others.

The effectiveness of these methods varies depending on the types and orientations of domains within the sample. For an example, optical birefringence cannot reveal domain structure for crystals possessing 180^o domains and cannot detect the sign of the domains [67, 12]. However it can reveal domain walls formed due to the material birefringence which results due to stress near the domain wall itself [12].

The selective etching technique (SET) followed by a high resolution imaging technique such as scanning electron microscopy (SEM) has been used to reveal the domain structure of $LiNbO_3$, to determine the sign of the domain and also to trace the emergence of domain boundaries on various planes. With SET, the $+z$ domains are found to etch not at all, while the $-z$ domains undergoes chemical etching at the rate of $\approx 1\mu m/h$ at room temperature for an HF:HNO_3 and mixture in the ratio 1:2 [12]. The SET method has one main drawback, in that it is physically a destructive technique. Thus, with this method the surface is destroyed. SET remains the most commonly used method however due to its effectiveness and intrinsic lack of ambiguity.

Miller [16] had shown, via transmission SHG, using the maser as a fundamental beam source, that SHG signal interacts with the domain walls within a ferroelectric crystal to enhance the output generated SHG signal. The reflected SHG beam was too weak due to the low intensity source of the fundamental beam and the interactions between this beam and the domain walls were not studied at that time. We show in this work that RSHG has the potential to reveal and characterize the presence of 180^o domains in $LiNbO_3$

4.3.1 Differences in SHG signal between the $+z$ and $-z$ domains of a z-cut $LiNbO_3$ crystal

For centrosymmetric material, it is known that the bulk material does not yield any SHG, however its surface can, and does, yield SHG due to inherent the discontinuity. So, in general, the surface and the bulk of any material can yield different SH signal characteristics as they originate from different sources. If we take the generation of SHG as due to the oscillation of the components of $\chi^{(2)}$, then, at the surface these components will be different from that of the bulk material.

The atomic arrangement of the metallic ions, defining the magnitude and the direction of $\mathbf{P}_s$, along the $+z$-face and that of the $-z$-face are inverted relative to each other, hence the surface discontinuity is not necessarily the same on both faces. Within a microscopic view, the oscillation of certain equivalent components of $\chi^{(2)}$ on both faces will not necessary be the same. This difference is in terms of the magnitudes rather than the phase. From the bulk, the difference along the $+z$ and $-z$ axis cannot be observed as the signal will be averaged over and should yield the same value. At the surface, however say the top ten atomic layers, the surface discontinuity should give a different average for both faces. Note however that, if the bulk-like properties dominate the observed signal, then such a difference will be minimized or lost entirely.

We want to use our method of separating the bulk and the surface SHG signal, to see if the SHG signals from both faces are indeed the same or not. Rotation anisotropy experiments are ideal for this investigation as they will allow us to probe different components of $\chi^{(2)}$. It is then expected that at given incident angle(s) θ_d and azimuthal angle(s) φ_d, the signal from both faces will be different in amplitude. Therefore, at θ_d and φ_d and a given set of γ and Γ, an RSHG scan along the propagation direction of PPLN will result in an amplitude-modulated RSHG mapping the start and the end of the domain.

Figure 4.5 shows the rotation anisotropy results with different input/output combinations of the polarization angle (see the caption and the legend for more details) from both faces of the poled samples. In obtaining this data, rotation anisotropy measurements were carried out as above (section 4.2) to obtain the full surface symmetry with the spot of the beam focused on the re-poled area, the crystal was then flipped over about the y axis such that $-z \rightarrow +z$ and $-x \rightarrow +x$ and the rotation anisotropy was repeated. The results in figure 4.5 are therefore for the domain inverted area of the poled samples. The set of results, for each input/output polarization angle combinations was then compared as shown in figure 4.5.

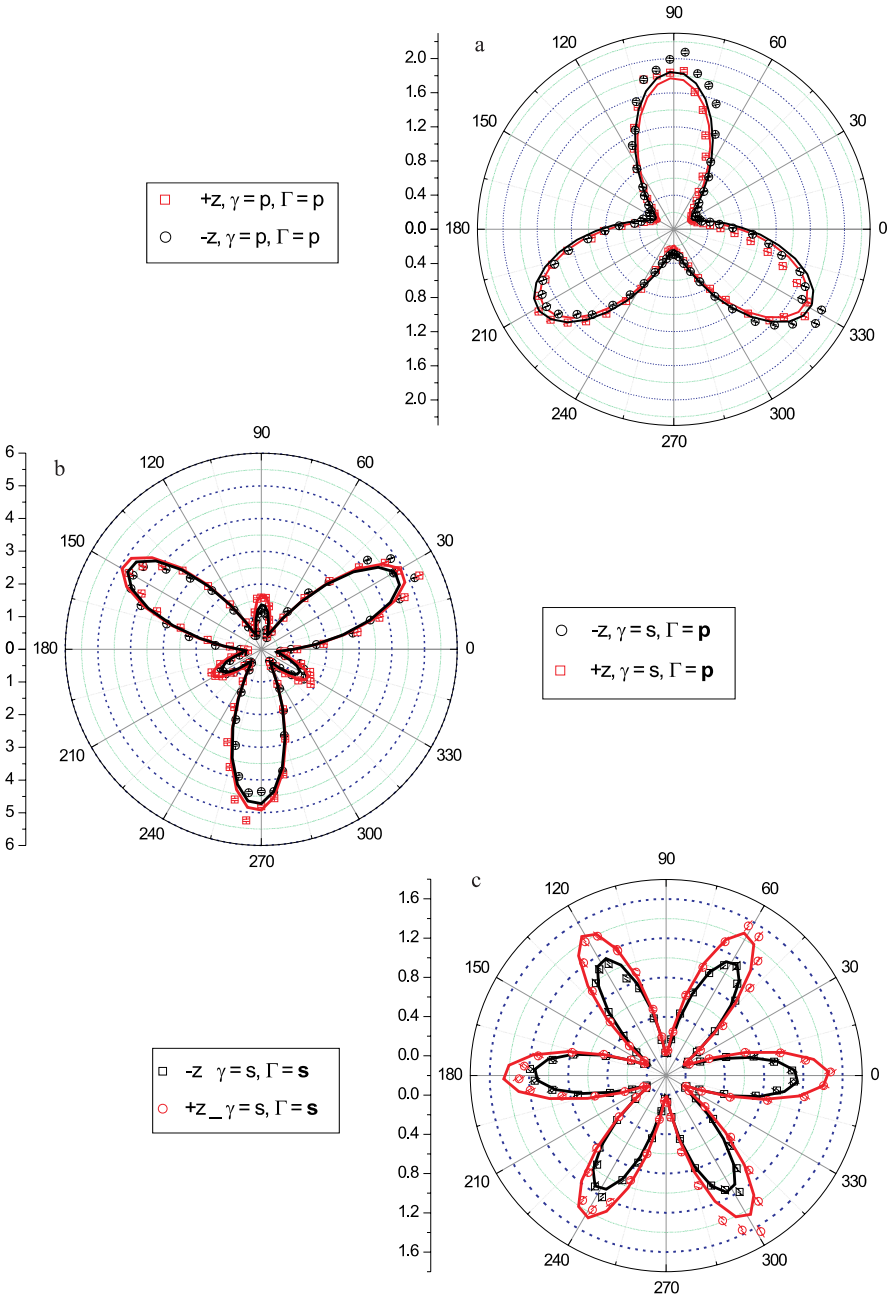

Figure 4.5: Rotation anisotropy results for domain inverted samples from both $+z$ and $-z$ of z-cut $LiNbO_3$ with: (a) $\gamma = p$ and $\Gamma = p$, (b) $\gamma = s$ and $\Gamma = p$, and (c) $\gamma = s$ and $\Gamma = s$. The solid lines are the fitted curves obtained by using equation (3.32), respectively. The plane of incidence lies along 90^o and 270^o line.

The results are from different poled samples which do not necessarily have the same composition though all were from congruent samples. Figure 4.5 (a) and (b) are from the same sample but taken at different times. This needs careful analysis as the results seem to differ, for even the same sample, after an elapsed period of one month.

For $\gamma = p$ and $\Gamma = p$ there seems to be no difference in SHG intensity as the sample is rotated around its normal surface. However a small difference is observed for $\gamma = s$ and $\Gamma = s$ and $\gamma = s$ and $\Gamma = p$, with the latter combination showing the difference only in the small peaks.

From figure 4.5 b-c, the SH from the $+z$ face is greater in magnituded than that from the $-z$ face for a specific γ, Γ, φ (i.e at $\varphi = 0^o, 60^o, \ldots$ for $\gamma = \Gamma = s$). If SH($+z$) is greater than SH($-z$) for a given γ, Γ, φ, then the RSHG method can be used to reveal the poled and nonpoled parts from the poled sample.

The trend of these results was not reproducible and this may point to the fact that the SHG signal of the interfacial region is more dominated by the bulk properties than by the surface properties. In future, the same experiment should be attempted at different incident angles as that can affect the contribution of the bulk and the surface on the SHG signal.

4.4 Use of RSHG to detect the inversion of the y-axis $+y \Leftrightarrow -y$ on reversal of the spontaneous polarization

The remaining part of the chapter focuses on the use of RSHG to detect changes in the y-axis polarity caused by domain inversion along the z-axis. The standard sign convention for the y and z axes is related to (and defined by) the piezoelectric effect: compression of either y or z faces results in a negative voltage appearing on their positive faces. There is a direct relationship between the sign of these faces and the relative atomic arrangement order along these axes within the crystal. The atomic arrangement is of interest here since it directly influences any atomic polarization within the medium and hence any changes within this order can therefore be detected, for example through the SHG technique. Within $LiNbO_3$, the cation order along the z-axis from the + z to the - z face is Nb^{+5}, Li^+, Vacancy, Nb^{+5}, as shown in Figure 4.6(d).

Along the y-axis, also shown in Figure 4.6 (d), there is also a corresponding direction-dependent order of cations, sandwiched between the two planes of oxygen ions forming

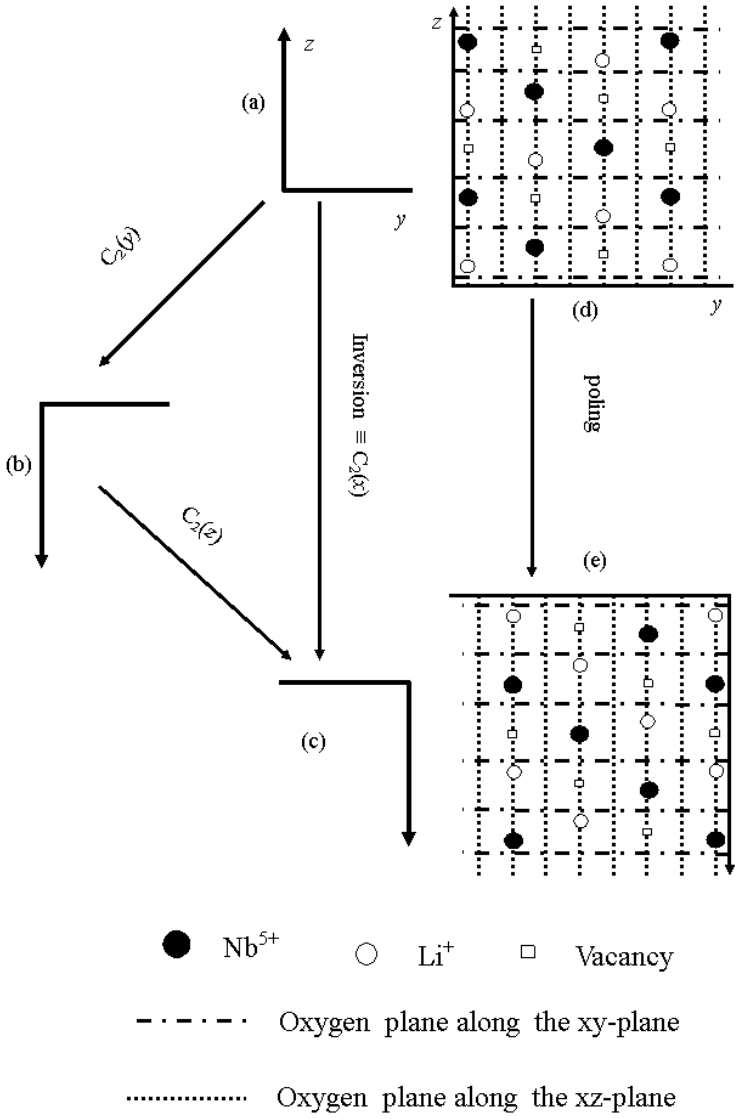

Figure 4.6: Possible physical operations to achieve inversion of a system with mirror planes along the yz plane. (a) and (d) are the coordinate system and the $LiNbO_3$ atomic arrangement in a virgin state. (b) Shows the coordinate system rotated by 180^o around the y-axis ($C_2(y)$) from the virgin state. (c) Shows the coordinates system rotated by 180^o around the x-axis ($C_2(x)$), which is similar to the inversion of the whole crystal. (e) $LiNbO_3$ atomic arrangement following domain inversion.

octahedron complexes with the cations (NbO_6 and LiO_6). The reversal of ($\mathbf{P}_s$) is a result of the forced relative displacement of the cations along the z-axis and, in the case of $LiNbO_3$, the cationic order reverses which also reverses the ordering along the y-axis, as shown in Figure 4.6 (e). It is these latter changes along the y-axis that we wish to investigate here via RSHG.

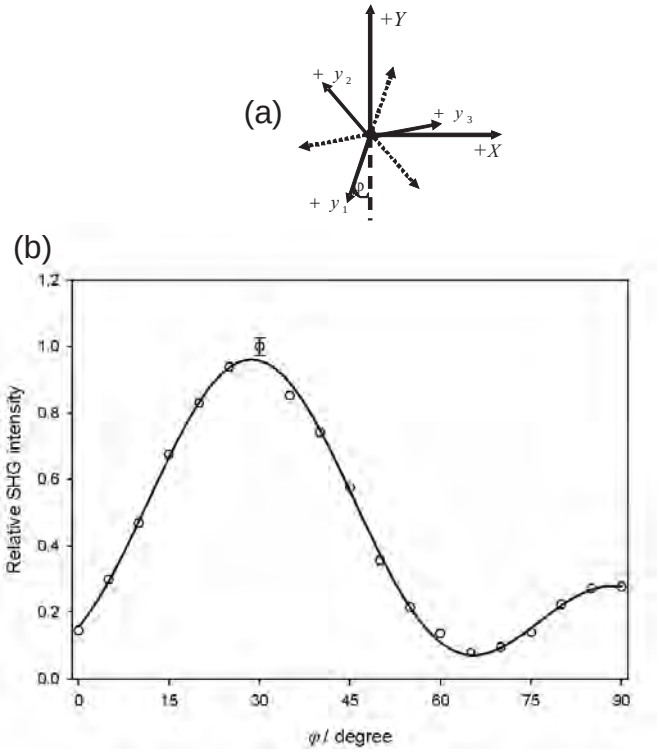

Figure 4.7: (a) The labeled y-axes with the + z direction pointing out of the page and also showing the direction of rotation. (b) RSHG curves with the global maximum value ($\varphi = 30^o$) corresponding to the alignment of the + y_3 direction along the + X direction. The SHG signal was normalized to the value at ($\varphi = 30^o$) and the error bars are calculated as in the previous figures in this chapter.

The reversal of ($\mathbf{P}_s$) and hence the reversal of the z-axis within $LiNbO_3$ can be pictured by the physical operation on a system of Cartesian coordinates with the same point group properties as $LiNbO_3$, as shown in figure 4.6(a). In this figure, the x-axis is not explicitly shown, since any effects on it upon inversion or rotation by 180^o around any axes (C_2(axis of rotation)) will be masked by the mirror plane that exists along the yz plane. Therefore, inversion of all three (x, y, z) crystal axes can also be achieved by $C_2(x)$ on figure 4.6 (a). From figure 4.6 (a), the reversal of the z-axis can be achieved in several ways, either by rotating the crystal $C_2(y)$, as shown in figure 4.6 (b), or by

inversion of the whole crystal relative to the laboratory-fixed axes as shown in figure 4.6 (c). All these operations result in the reversal of the z-axis ($+z \Leftrightarrow -z$) but, as shown in figure 4.6 (b), $C_2(y)$ on figure 4.6 (a) leaves the direction of the y-axis unchanged. Although this $C_2(y)$ operation on figure 4.6 (a) results in $+z \Leftrightarrow -z$, it cannot lead to the physical domain inversion along the z-axis since it would leave the sign of the y-axis unchanged and hence leave the order of cations along the y-axis intact. Domain reversal is therefore equivalent to the operation shown in figure 4.6(c), in which both the y and z axes are reversed ($+y \Leftrightarrow -y, +z \Leftrightarrow -z$) within the poled area, which is equivalent to the inversion of the whole crystal or just the $C_2(x)$ on figure 4.6(a) for a crystal with the mirror planes along the yz plane.

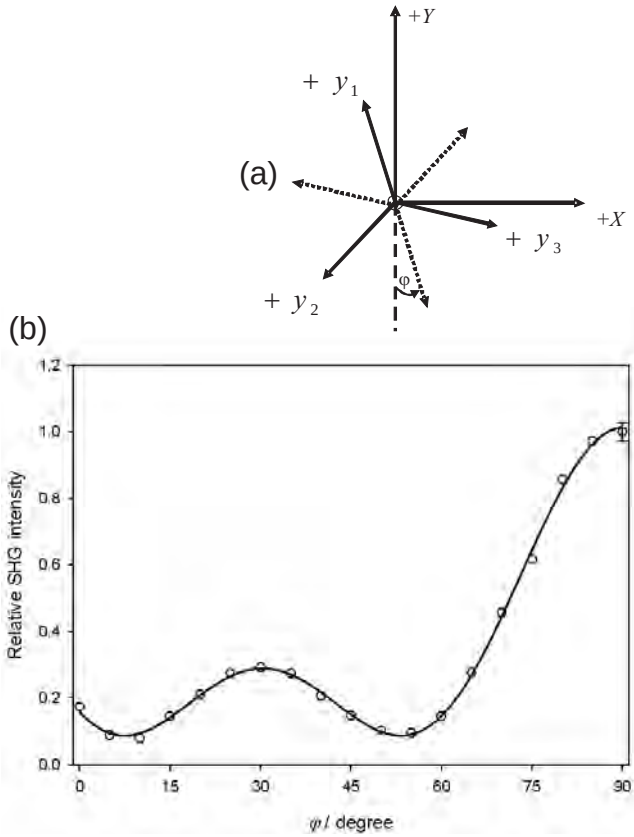

Figure 4.8: (a) The labeled y-axes with the $-z$ direction pointing out of the page (b) RSHG curves with the local maximum value ($\varphi = 30^o$) corresponding to the alignment of the $+y_3$ direction along the $+X$ direction. The SHG signal was normalized to the value at ($\varphi = 90^o$) and the error bar are calculated as in the previous figures in this paper.

The information about the polarity of the y-axes cannot be determined from the curves, which shows the location of the mirror planes and hence of the y-axis, with respect

Table 4.3: Summary of the RSGH results for both faces of the virgin $LiNbO_3$ for *s, p*

Crystal face	$\varphi = 0^o$	Global maxima	Local maxima	figure
+z	$+y_1$ along $-Y$	$+y_3$ along $+X$	$-y_1$ along $+X$	figure 4.7
-z	$-y_1$ along $-Y$	$-y_1$ along $+X$	$+y_3$ along $+X$	figure 4.8
-z	$-y_1$ along $-Y$	$-y_2$ along $+X$	$+y_1$ along $+X$	figure 4.9

to the incidence plane, by the minimum SHG signal, and therefore other polarization combinations must be used. With $\Gamma = p$, the interaction between the rotationally isotropic and anisotropic components of the $\chi^{(2)}$ tensor should reveal the polarity of the crystalline y- and z-axes relative to the input and output geometry. As shown in figure 4.4, the locations of the global and local maxima coincide with the minima and hence yield information about the polarity of the y direction.

The relationship between the sign of the y and z axes with respect to the plane of incidence was investigated using rotation anisotropy RSHG experiments on a virgin $LiNbO_3$ sample having known crystalline axes and polarities. Though the three y-axes are identical, they will contribute to the observed SHG anisotropy at different azimuthal angles. We therefore argue below from the SHG results, that it is crucial to label these three equivalent y-axes in order to detect any polarity changes after z-axis inversion. During the experiment, the positions of the y-axes were known for any azimuthal angle.

Table 4.3 shows the summary of the results on both faces of the virgin $LiNbO_3$ for s, p. The direction of rotation around the z-axis on the + z and - z faces was clockwise and anticlockwise as shown by figure 4.7(a) and figure 4.8 (a), respectively. The reversal of the z-axis was achieved through $C_2(x)$ such that $+y_1 \Leftrightarrow -y_1, +y_2 \Leftrightarrow -y_3, +y_3 \Leftrightarrow -y_2$and $+z \Leftrightarrow -z$ while the sign of the x-axis was left unchanged relative to the plane of incidence, as shown by the previous figures. From table 4.3, it is then straightforward to make the following conclusions for : On the $+z$ face, the $+y$ direction gives a global maximum for the SHG signal at $\varphi = 30^o$, as shown in figure 4.7(b), under rotation anisotropy when the $+y$ directions are aligned parallel and pointing along the positive direction of the X-axis (referred to as $+X$ in Table 4.3). On the $-z$ face, the $-y$ direction gives a global maximum for the SHG signal at $\varphi = 90^o$, as shown in figure 4.8 (b), from rotation anisotropy when the $-y$ directions are parallel and pointing along the positive direction of the X-axis.

It is clear from the labeled y-axes, in figure 4.8 (a), and the summary, in Table 4.3, that rotating the crystal clockwise while probing the $-z$ face will result in the same SHG curve, figure 4.9 (b), as the one in figure 4.7 (b) where the experiments were performed

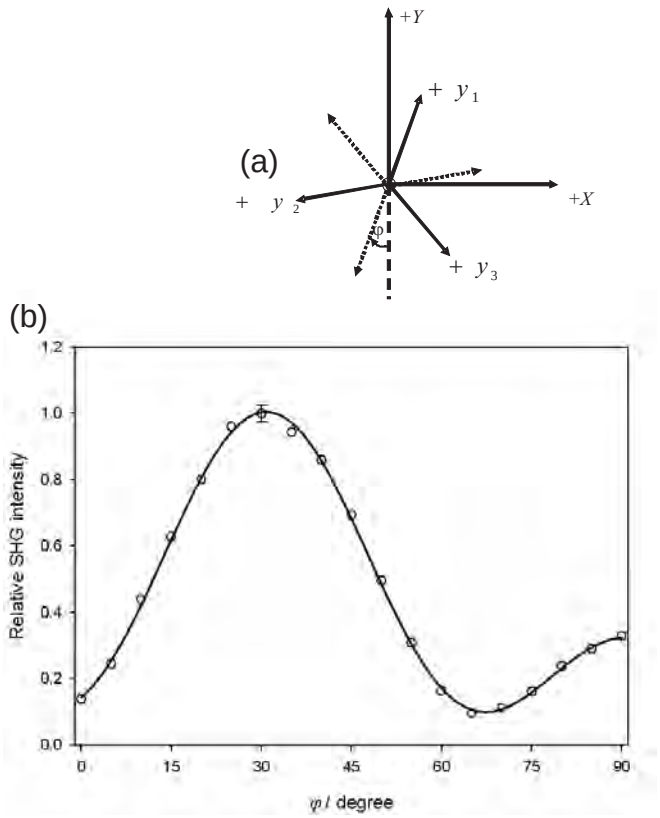

Figure 4.9: (a) The labeled y-axes with the -z direction pointing out of the page. (b) RSHG curves with the global maximum value ($\varphi = 30^o$) corresponding to the alignment of the $-y_2$ direction along the $+X$ direction. The SHG signal was normalized to the value at ($\varphi = 30^o$) and the error bars are calculated as in the previous figures in this paper.

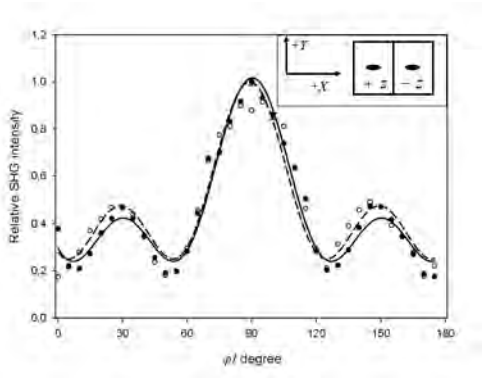

Figure 4.10: Inset diagram shows the schematic top-view of a half re-poled $LiNbO_3$ sample. SHG results from the + z face of the virgin part (filled circles) and - z face of the poled area (open circles). The SHG signal was normalized to the value at ($\varphi = 90^o$)and the error bars are calculated as in the previous figures in this paper.

on the + z face. However, the contributing y-axes for global maxima, as an example, in these two cases possess opposite signs. The effect of the direction of rotation on the same crystal face for these SHG experiments is to shift the azimuthal angle by 180^o, therefore, figure 4.9 (b) is just the continuation of figure4.8 (b) from $\varphi = 180^o$ onward. Thus, performing rotation anisotropy SHG experiments with the same sense of rotation on different faces must result in similar curves.

The above conclusions were then used to detect changes of the sign of the y-axis imposed by the reversal of ($\mathbf{P}_s$). The inset diagram in figure 4.10 shows a schematic top-view of a $LiNbO_3$ sample that has had half its area domain inverted. The face of the virgin part is pointing out of the page and that of the domain inverted (- z face) is pointing into the page. RSHG rotation anisotropy experiments were performed on the virgin part and the crystal was then translated along the $+X$ direction and the same experiment was repeated on the poled area with the same rotation direction. The results are shown in figure 4.10 and their clear similarity show conclusively that the sign of the y-axes must have been reversed in the poled area (- z face) relative to that in the virgin area (+ z face) since similar curves are observed from both the - z and + z faces. These results show conclusively the use for RSHG for the detection of the reversal of the y-axis as a result of the domain reversal procedure.

4.5 Time-dependent Surface Second Harmonic Generation effects

As discussed before the Nb^{+5} and Li^{+1} ions of $LiNbO_3$ in the ferroelectric phase are displaced from their equilibrium positions, attained in paraelectric phase, leading to the presence of $\mathbf{P}_s$ below T_c. The magnitude of $\mathbf{P}_s$ is affected by the compositional ratio of the Li^{+1}/Nb^{+5} of the $LiNbO_3$ crystal. Congruent $LiNbO_3$ (composition: $Li^{+1}/[Li^{+1}]+[Nb^{+5}]$=48.4%) crystals are used in many applications due to the reproducibility of their composition. The remaining percentage is occupied by the intrinsic defects which lead to an asymmetric hysterisis curve for the forward and backward poling of this crystal. These intrinsic defects are involved in the formation of an internal electric field (E_i) pointing parallel to $\mathbf{P}_s$ in a virgin sample. During forward poling, at room temperature, $\mathbf{P}_s$ is inverted but E_i does not invert immediately.

Following the forward poling, realignment of E_i towards the new direction of P_s can be accelerated by annealing the poled sample at a temperature above 200 ^oC. Without annealing, there is a longer-time relaxation period for which the point defects and E_i will relax to their equilibrium "virgin like" position. This behavior has already been discussed by several authors and the time constant for relaxation has been determined [18, 19, 20].

It is known that the presence of point defects affects the second-order nonlinear optical (NLO) tensors of the crystal with the greatest contribution coming from the Li-O bond [28, 68]. After forward poling, the NLO tensor coefficients of the crystal are different from that of the virgin sample and they may relax back after a suitably long period of time. In this section, we investigate this relaxation of these point defects that occurs after the forward poling. We describe the sample preparation before we show the results on the time-dependent RSHG.

Poling of the samples was achieved via the application of a high voltage across the z-faces of the crystal, placed in a water cell as described in chapter 3. Within two minutes after the sample was poled, one side of its face was abraded, using a 600 grit sand paper, to minimize reflection from the bottom surface before being placed on the stage. The same experimental setup as described in chapter 3 was used for this measurement. Rotation anisotropy measurements were done to locate the correct azimuthal axis. Two spots on the sample, one from the non-poled virgin area and the other from the poled area were selected for measurements, as shown in figure 4.11. The determination of the y-axis and post sample preparation took less than 20 minutes in total. An x-y micro-positioning

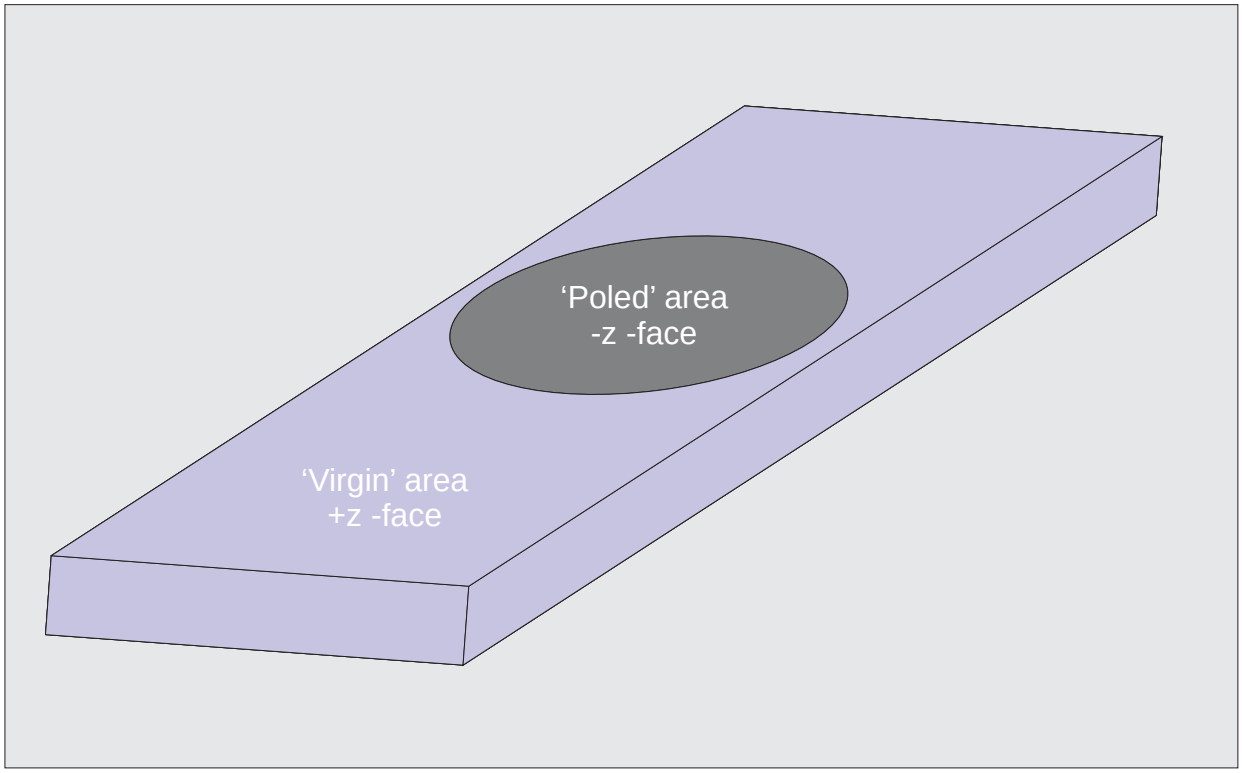

Figure 4.11: A schematic picture showing the domain inverted area and the virgin area on a domain inverted sample. Two spots were selected from the two areas for the collection of the RSHG data as a function of time

stage was used to move between the two spots. At a given input/output polarization, the two samples were examined one after the other in 1 minute intervals for a given period of time. To minimize thermal effect on the sample, low energies per pulse (but enough to give a good any signal-to-noise ratio) were used and the repetition rate was some times further reduced from 10 Hz to 1 Hz. At a given spot, 250 points were collected to make a final data set for that time. The data was collected for as periods long as 4 hours.

The data from the virgin area was used as a reference as no relaxation is expected from that area. As the other surface has been abraded, and hence destroyed as far as any meaningful RSHG measurements were concerned, only the top face was then available for investigation. For the virgin area presenting a + z face of the virgin crystal then the domain inverted area will present a - z face.

Figure 4.12 shows the SHG signal from the virgin and the domain-inverted areas of the poled sample. In this case, the y-axis of the crystal was placed parallel to the plane of incidence which gives rise to the maximum SHG signal. The signal from the $+z$

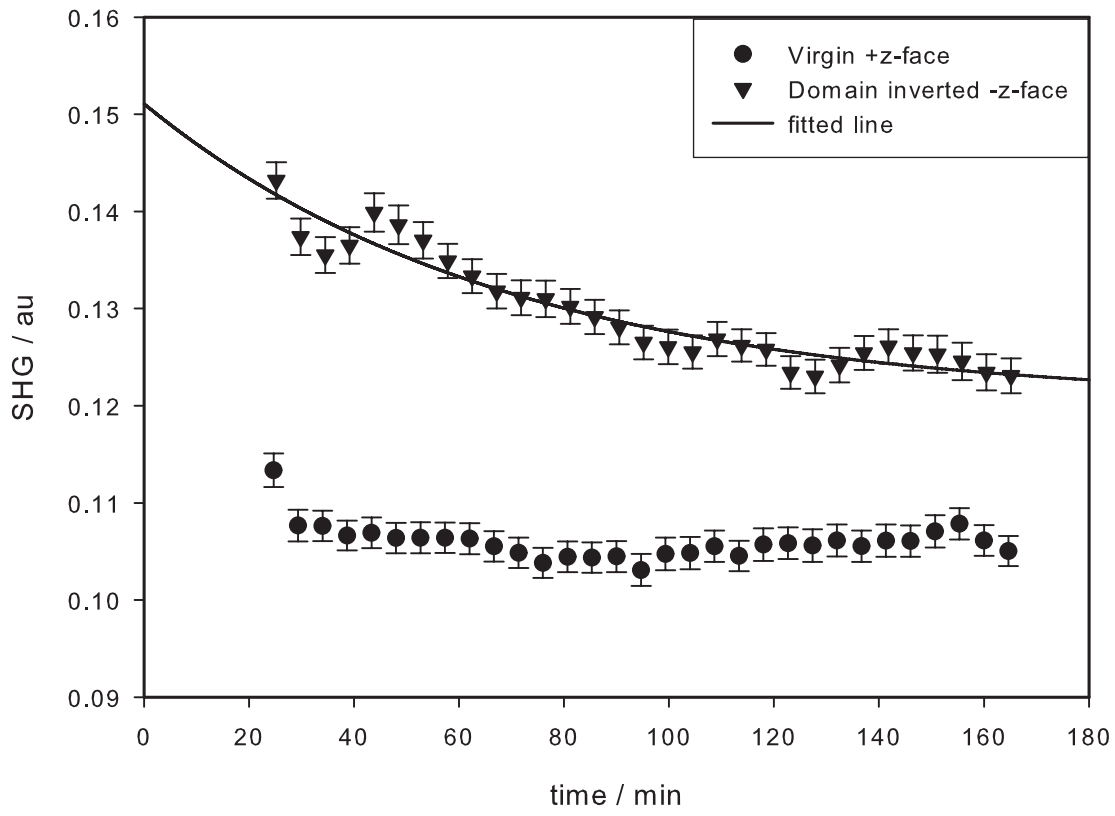

Figure 4.12: SHG signal vs the time after the sample was poled. The y-axis was placed parallel to the incidence plane and $\gamma = s$ and $\Gamma = p$.

face of the virgin part of the sample does not seem to change over the duration of the experiment. However an exponential decay of the -z face of the domain inverted part of the sample is observed. This observed decay seems to stabilize at a point which is still higher than that of the +z-face of the virgin sample. This trend is not surprising based on the results presented in section 4.3.1 in which it was shown that the +z and the -z face do not necessarily show the same strength of SHG signal.

Figure 4.13 shows the SHG signal for the case where the x-axis was placed parallel to the plane of incidence. This corresponds to the signal giving rise to the local maximum as seen from the rotation anisotropy result. Also, in this case, only the signal from the -z face of the crystal seems to be relaxing. However, the relaxation in this case is an admittedly noisy growth behavior with the time constant of approximately 40 min.

The above results could not be reproduced however and, in fact, data of this quality

was never observed again when the experiments were repeated. Instead, a non-relaxing signal was observed from both the poled and the virgin area. We have used nanosecond pulses, which may have a sufficient local thermal effect similar to annealing the sample above 200^oC. This annealing effect has been shown to accelerate the relaxation of the internal field to a period of about 30 sec [18]. However, it required about 1 minute to accumulate one point on the presented graph. Thus, if the laser itself had some thermal effect, maybe via random intensity fluctuations, the relaxation could have disappeared even within the data collected.

Houe and Townsend have demonstrated thermal polarization reversal of lithium niobate through the use of heat pulses generated by a laser beam [69]. They have preheated their samples to 400 ^{o}C and applied an external field of 187 Vcm^{-1} while irradiating the sample with the laser beam with energies in the range 40-90 mJ with a pulse duration of 5ns at 532 nm to achieve poling. At this wavelength, $LiNbO_3$ is transparent and hence not much heat is expected from the laser beam with this pulse duration. To achieve the desired thermal effect from the laser beam, they have used a 90 nm thickness copper film deposited on the -z face of the crystal to absorb the energy from the beam, convert it into heat energy which is then conducted into the crystal to locally increase the temperature. However, they have also observed that the copper film was evaporated within 50 ns of irradiation and that poling did occurs even at places were there was no copper deposited. They did not specify the geometry of the optical setup but, the heat generated at place where there was no copper film to start with may have resulted from the induced SHG within the surface. At 266 nm, lithium niobate is very absorptive and heat can accumulate to have given them a sufficient increase in temperature to achieve poling with the applied external field.

The above discussion suggests that the generated SH beam in our experiment may have had enough accumulative energy to raise the local temperature at the sampling spot to above 200^o and thus annealing the sample. We have limited the average energy of our fundamental beam to less than 25 mJ. Annealing the sample at this temperature has been shown to accelerate the reversal of the internal field after poling. To avoid this possible heat effect, the experiment should be performed in the infrared region such that the generated SHG beam has a wavelength in the transparent range. Also, a low repetition rate of about 1 Hz is suggested.

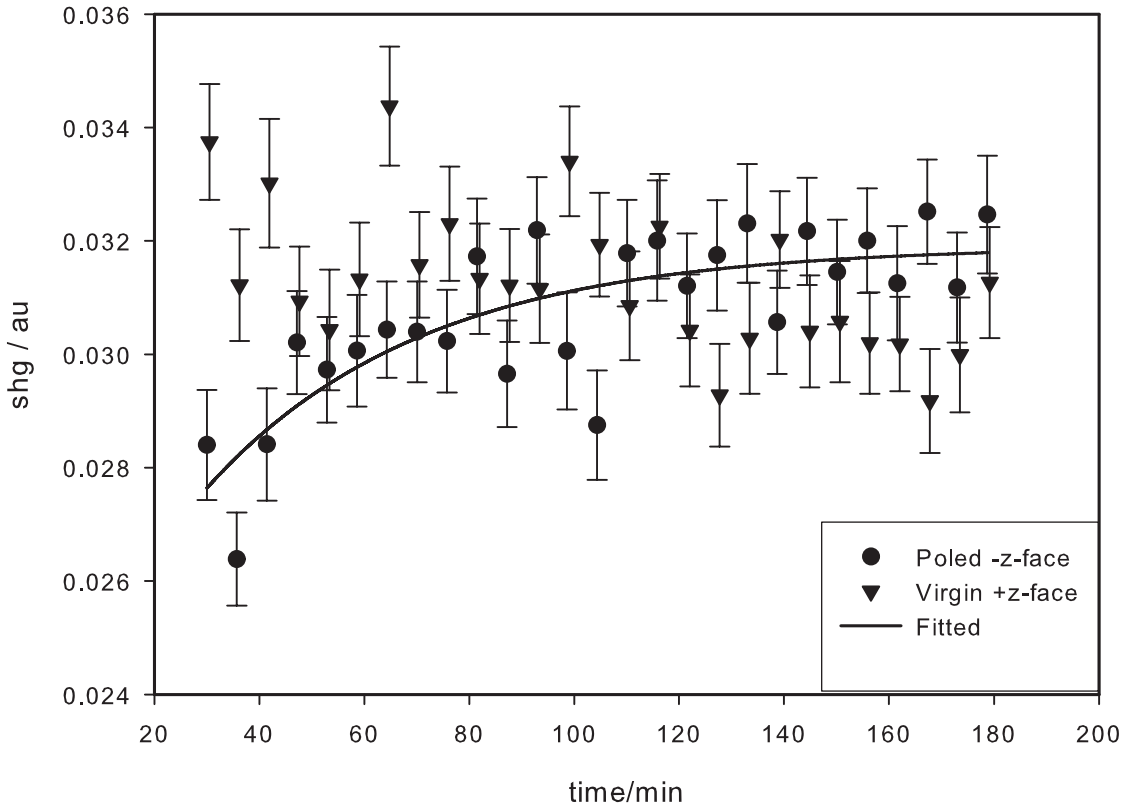

Figure 4.13: SHG vs time after the sample was poled. The x-axis was placed parallel to the incidence plane.

4.6 Conclusion

RSHG experiments were used to reveal the interfacial layer symmetry and to determine the crystallographic axes of a z-cut congruent lithium niobate crystal. The high UV absorption within this material has been used effectively to limit the generation of the SHG signal to the interfacial layer and hence to extend the use of RSHG to the non-centrosymmetric materials. Based on the absorption depth of the medium, careful choice of the fundamental wavelength, and hence the variation of the interfacial layer thickness, should result in the approach used in this chapter being sensitive to a monolayer. As a special case, RSHG was also used to detect the reversal of the y-axis caused by the domain inversion along the z-axis. This effect is made possible by the interaction between the isotropic and anisotropic second-order susceptibilities and hence it is dependent on the input and output polarization angles.

Due to the non-reproducibility and inconsistency of the time dependent results, it seems fair to conclude that our present RSHG system cannot reveal the internal field relaxation within the domain inverted area of the poled $LiNbO_3$ crystal. It is unlikely that the fundamental beam is causing any thermal effect within the sampling spot, but the induced SHG signal can have accumulative thermal effects which can have temperatures above 200 ^{o} C, enough to accelerate the relaxation of the internal field. It is therefore suggested that the use of the infrared fundamental beam can resolve this problem as the induced SHG signal will be outside the absorption range of the crystal and hence have minimal thermal effects.

These effects, if reproduced, would show that RSHG is indeed a valuable tool for such surface relaxation phenomena. Due to the lack of time to further investigate these effects, it is not possible to conclude either way, and also no publication has been forthcoming.

Chapter 5

Optical MicroCavity design and modeling

5.1 Introduction

In this chapter the designs and applications for optical microcavities are introduced. Specifically, the properties and behavior of a hexagonal microcavity will be dealt with in detail in preparation for the next chapter where this optical device will be used for the production of efficient nonlinear optical processes.

An optical cavity is simply an optical setup that allows guidance and the build-up of the optical signal within it. One such cavity implementation is the basic two plane-parallel mirror set-up placed at a fixed distance apart. In this example, the guidance of the optical beam is achieved by multiple reflections between the two mirrors. The signal build up, and cavity resonance, occurs if constructive interference of the multiply reflected beams (per round trip) takes place. On resonance, the intensity of the light beam trapped between the two mirrors grows. Thus the separation between the two mirrors, relative to the wavelength of the optical beam, controls the resonance condition within the cavity. This particular example of the optical resonator is called the Fabry-Perot cavity and the two mirror set-up can have any combination of plane or curved mirrors to suit the desired geometry and properties [51].

Optical cavities are aimed at trapping light, ideally without any loss, until they are triggered to release the stored light out of the cavity. Practically, nulling the losses within a cavity is very hard and a more efficient optical cavity is one that can store a large fraction of the light compared to that lost during the cavity lifetime. A figure of merit,

used to describe the energy stored in the cavity, relative to that lost by the cavity per round trip, is called the quality factor (Q). Effective optical cavities will therefore possess high Q. A gain medium can be placed between the two mirrors to enhance the cavity oscillation and such optical cavities are called active optical resonators, as opposed to the passive cavity which does not have a gain medium.

In optical applications, such as optical communications, the integration of different optical components is required. In this integration, size and packaging of optical components plays an important role in the practicality of the final devices. This then imposes a size and compactness requirement on any optical devices, such as optical cavities, for them to form part of any optical integrated circuits. Thus, a high Q is not enough unless the corresponding cavity is small enough to integrate with other micro-optical systems such as optical fibers for any device to form part of a practical optical 'circuit'.

Optical cavities with micrometer dimensions, termed optical microcavities, have therefore attracted much research attention for their inclusion and role in integrated optical circuits. They are normally placed near to at least one coupling waveguide device which then allows in-coupling and out-coupling of light [70]. Microcavities have been used for various applications such as micro lasers, optical filters, and non-linear devices, amongst others [21, 22]. Light confinement and resonance within the microcavity is achieved via total internal reflection of the light beam between the guiding medium and the surrounding medium and mode wavefront matching per round trip. With mature technologies for waveguide fabrication available, microcavities with high modal confinements and low modal volume have started to emerge and several geometries of the cavities including microspheres, polygonal cavities, and photonic crystal resonators have been investigated so far for a range of applications.

Here, we focus our attention on the optical microcavity devices with the potential for use in nonlinear applications such as nonlinear frequency generation. The motive behind this work is to utilisz the signal stored at resonance within the cavity to enhance the efficiency of the nonlinear optical process. For a second order nonlinear optical process, the conversion efficiency is proportional to the square of the propagation length within the optical device. Obviously, higher efficiency for this kind of process in traditional linear devices requires longer lengths that imposes a limitation for integration with any other micro-optical systems. However, high Q within a microcavity implies an effective longer integration-length within a small volume. Hence multiple round trips within the microcavity can equate to the longer length of bulky devices.

The nonlinear intensity is also proportional to the square of the fundamental intensity. Since microcavities can be made to resonate the input beam, they can serve as platforms for effective nonlinear optical process while at the same time maintaining small devices size. Thus these devices are both compact and integratable with other devices. Intensity-dependent nonlinear optical processes such as all-optical switching have shown efficiency improvements due to the enhancement of the fundamental power in the cavity which resulted in the reduction of the required switching power in semiconductor microcavities [23].

Full details of this specific application will be given in the next chapter, in which, a hexagonal microcavity will be explored for its nonlinear optical application. To appreciate the potential application for these devices in nonlinear optics we first review the relevant linear optical processes and mechanisms governing its operation. In doing so, we will expose critical issues which need to be considered when designing this device. The rest of this chapter focuses only on the study of the linear properties of these microcavities.

5.2 Review of Microcavities

Optical microresonators can be fabricated by exploiting either TIR of light at the interface between a dielectric material and the surrounding medium such as air, or distributed Bragg reflection (DBR) from periodic multilayered structures or array of holes in a periodic crystal (PC).

A microsphere resonator utilizes TIR for mode confinements around the circumference of the sphere. Their dominants modes are WGMs and have ultra-high Q-factor of order of 10^9, they have large modal volume and dense modal spectrum. Most organic and non organic liquids are highly transparent and have a high refractive index contrast when surrounded by air, for these reasons they have been used for microsphere resonator. Application of liquids resonator is however limited because of the difficulty in manipulation and the lifetime of the droplets is short due to evaporation. Solid spheres on the other hand are easy to handle [71].

Amorphous materials like fused silica are good candidates for microsphere resonator as they have a very small optical attenuation from the UV to the infra red (1.5 μm. Silica micro spheres have ultra-high Q factor of order of 10^9, however, they also have high density degenerate modes which cannot be easily separated [72]. These degenerate

modes complicate their application for spectral analysis and make it tricky for on chip integration with other components.

Several authors [21, 73, 74, 75] have recently proposed micro-toroidal resonators. Micro-toroidal resonators demonstrate a very high WGM Q-factor of about 10^8 [74] which is comparable to that of the microspheres but with the advantage that micro-toroidal resonators have less modal volume and higher FSR and they are easy connected to the other components.

Circular high index contrast microring and microdisk resonators based on planar waveguide technology have been widely demonstrated. Diameter as small as 1-10 μm are able to support WGM with high Q-factor of 10^5 and are used as add/drop filters for WDM networks [76, 77, 78, 79] for example. Circular micro cavity belongs to a broad range of polygonal microcavities. Polygonal microcavities can attain different shapes such as, racetrack resonator [53], square/rectangular [80, 81], triangle, hexagonal [82, 83, 84] and octagonal microcavties.

The Q-factor is lower on other polygonal microcavities as compared to the circular ones due the sharp corners which introduce the losses. The Q-factor in these cavities can be improved by rounding corners. These other non-circular microcavities, also tend to guide other non-WG modes such as four-bounce or six bounce modes in the case of a square and a hexagonal, respectively. These later modes also have a defined path within the cavity and hence a preferred incident angle guided by TIR between the facets of the devices. The incident angle preference reduces the mode degeneracy, for example, hexagonal microcavity prefers modes with 60^o angle of incidence within the cavity. With the propagation path known, manipulation of the mode like phase matching the fundamental mode with the harmonic modes is possible.

Other kinds of microcavities utilize Bragg reflection either alone or with TIR. Photonic crystal (PC) cavities made by drilling holes on slab waveguide have been demonstrated with a moderate Q-factor 10^4 [85].

5.2.1 Material

As the need increases for smaller optical devices, for dense optical integrated circuits, the selection of the material for the device becomes a crucial factor as this choice affects the device's physical size, fabrication steps and behavior during operation. Device size

depends on the index contrast between the optical guide and the surrounding medium and therefore on the cross-section of the waveguide. Higher index contrast allows the optical beam to be bent more sharply, and hence a small bending radius can be achieved with tolerable bend losses, thus allowing very small size microcavities to be designed [86, 54]. A large free spectral range ($FSR \propto 1/n_{eff}L$) is required to avoid signal cross talk, for example in the third telcom window, where a FSR of at least 30 nm is required [70]. This then requires a smaller cavity round trip length (L) for a given effective index (n_{eff}).

Glass materials are inexpensive, have a moderate index contrast and are compatible with most standard fabrication technologies [87]. Silica glass has a wide transparency window, low intrinsic loss and is used extensively for optical fibers. However this material has poor second-order nonlinear properties. Semiconductor materials have the highest index contrast compared to that of glass materials and thus can attain even smaller devices. This type of material has attracted much interest for microcavity fabrication with both passive and active functionalities possible in a single material, thus serving as a potential candidate for monolithic devices. Polymer materials have also demonstrated much potential due to their index tunability, low cost fabrication and good optical properties.

Many material ranging from, liquids droplets, amorphous material such a fused silica, crystalline material, polymer and semiconductors have been demonstrated as good materials for microresonator applications [71]. However, most of them are only suited for the linear optics application as they have low nonlinearities or are difficult to handle. Semiconductors have the highest nonlinearities, but, they are often not compatible with the phase matching process due to the high dispersion and the fact that they are cubic.

However, we are interested here in the nonlinear optical properties and we therefore require a material which is intrinsically nonlinear. One choice will be semiconductor materials as they have inherent high nonlinearities, as has already been demonstrated. Materials such as lithium niobate are also known for their nonlinear applications and they also allow manipulation of these domain properties via conventional electric field poling (see ref [4]). In the next section, coupling of light in and out such cavities will be reviewed.

5.3 Theory of a Microcavity

Figure 5.1a shows a geometrical layout of a microcavity with two waveguides, one to couple light into (input bus) the cavity and one to couple light out of the cavity (output

bus). Ideally, both of the bus guides are arranged such that they are not multimoded, to avoid excitation of different cavity modes. The following description is general and it holds for every microcavity with any geometrical shape and refractive index. Only the one direction of propagation within the cavity is considered.

A beam of light with wavelength λ and amplitude E_1 is launched at port A and the resulting bus mode is allowed to propagate along the input bus. At the coupling point, where the separation between the input bus and the microcavity is small enough to allow the tail of the evanescent wave from the input bus to extend in the vicinity of the cavity, part of the mode in the input bus given by $\zeta_a E_1$ is evanescently coupled in the cavity leaving behind $t_a E_1$ which continues to propagate along the bus. ζ_a is the coupling coefficient between the input bus waveguide and the cavity and $t_a = \sqrt{1-\zeta_a^2}$ is the transmission coefficient [88, 89].

Within the cavity, the resulting cavity mode propagates around the cavity via total internal reflection (TIR). After traveling a distance equaling half the cavity round trip, part of the cavity mode whose evanescent wave extent in the vicinity of the output bus given by $(\zeta_b\sqrt{\tau}(\zeta_a E_1)exp(i\frac{\phi}{2}))$ is coupled out of the cavity into the output bus thus leaving behind a mode with amplitude of $E' = t_b(\zeta_a E_1)\tau exp(i\phi)$. τ is the total attenuation per round trip and $\phi = \frac{2\pi n_{eff}}{\lambda}L_{eff}$ is the phase shift per round trip accumulated by the mode. L_{eff} is the total effective path traveled by the mode in the ring and $t_b = \sqrt{1-\zeta_b^2}$ is the transmission coefficient where ζ_b is the coupling coefficient between the cavity and the output bus waveguide [88, 89].

After one round trip, part of the mode that had survived a trip around the microcavity is coupled out into the input bus while the remaining part continues around the ring. This continuing cavity mode will only reinforce the newly coupled cavity mode from the input bus provided that the phase difference between these two modes is $\phi = 2\pi m$, where $m = 1, 2, 3, \ldots$ and that they have the same cavity propagation constant.

The evanescent modes from the multimoded input bus will excite all cavity modes that have the same cavity propagation constant matching that of the evanescent one. However, the strength of the excited cavity modes will differ and only those which satisfy TIR and survive the cavity attenuation over one cavity round trip will make it around the cavity. That is, if the cavity has very high optical losses, the surviving modes with correct ϕ relative to the newly coupled modes, will make no contributions to the cavity build-up due to its lower amplitude.

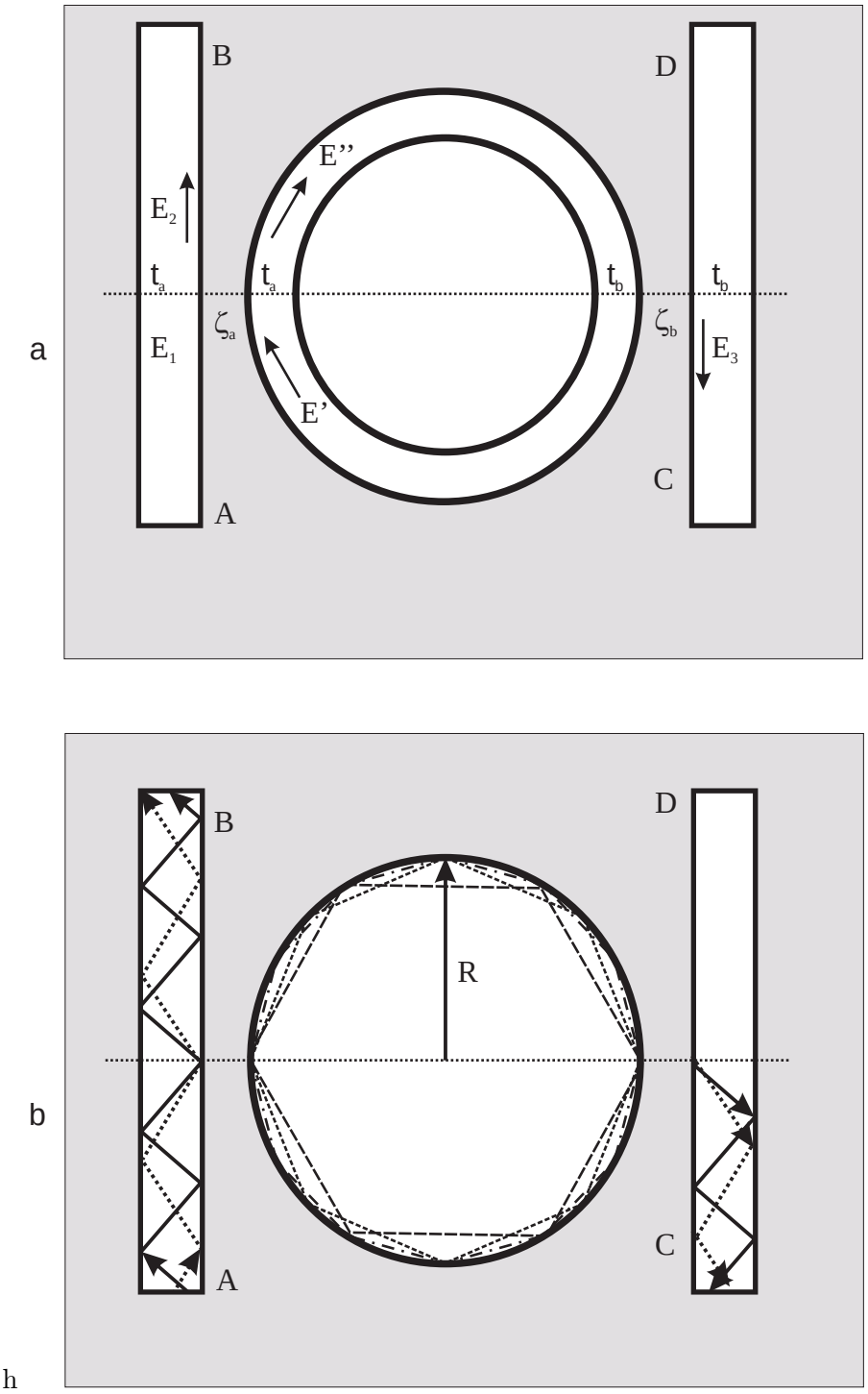

Figure 5.1: a) geometrical layout of a ring resonator in general parameters, b) multimoded ring resonator confining 12, 8 and 6 bounces laterally coupled to a multimoded input and output bus

After a cavity round trip, however, if $\phi \neq 2\pi m$ there will be no reinforcement on the modes in this cavity and this ensures that only the resonating modes survive multiple cavity round trips. Figure 5.1 b, shows a multimoded ring microcavity in which cavity modes with 12, 8 and 6 bounces are phase-matched and therefore they will survive if excited. Hence, it is necessary to use a single mode input bus especially when the microcavity geometry has a potential of being multimoded, as such for rings. The amplitudes at different parts of the microcavity can be summarised as shown in the following equations [88, 89].

$$E_2 = t_a E_1 + i\zeta_a E' \tag{5.1}$$

$$E" = t_a E' + i\zeta_a E_1 \tag{5.2}$$

$$E' = t_b E"\tau exp(i\phi) \tag{5.3}$$

$$E_3 = i\zeta_b E"\sqrt{\tau} exp(i\frac{\phi}{2}) \tag{5.4}$$

At any time, the intensity at the throughput and the drop positions can be written as shown below.

$$|S_{21}|^2 = \left|\frac{E_2}{E_1}\right|^2 = \frac{t_a^2 + (t_b\tau)^2 - 2t_a t_b \cos(\phi)}{1 + (t_a t_b \tau)^2 - 2t_a t_b \tau \cos(\phi)} \tag{5.5}$$

$$|S_{31}|^2 = \left|\frac{E_3}{E_1}\right|^2 = \frac{(\zeta_a\zeta_b)^2\tau}{1 + (t_a t_b \tau)^2 - 2t_a t_b \tau \cos(\phi)} \tag{5.6}$$

ζ is a function of the coupling properties such as the coupling gap and the coupling length and τ is a function of the material and fabrication process while ϕ is a function of the geometrical size of the cavity, and it is this function that defines resonance within a microcavity with a given refractive index. Thus, for a given refractive index, the properties of the cavity at resonance can be achieved by studying ϕ alone. Figure 5.2 shows a typical normalized intensity output spectrum (normalized to the input E_1^2) from port B and C in figure 5.1 given by equations (5.5-5.6) for $\zeta_a = \zeta_b$. τ is fixed at 0.98 for a ring with $R = 20\mu m$ and $n_{eff} = 3.2$. These intensities are functions of the input/output coupling strength and can be varied by changing the coupling coeffiecints. For example, the normalised throughput intensity at resonance ($\lambda = 1550nm$) can be made to be zero by varying the input coupling coefficients until $t_a = t_b\tau$, a condition referred to as *"critical coupling"* as shown in figure 5.3 [90, 91, 92]. At critical coupling the value $|S_{21}|^2 = 0$ and $|S_{31}|^2$ attains its maximum value. Figure 5.3 also shows that a typical symmetrically coupled ($\zeta_a = \zeta_b$) resonator does not achieve critical coupling.

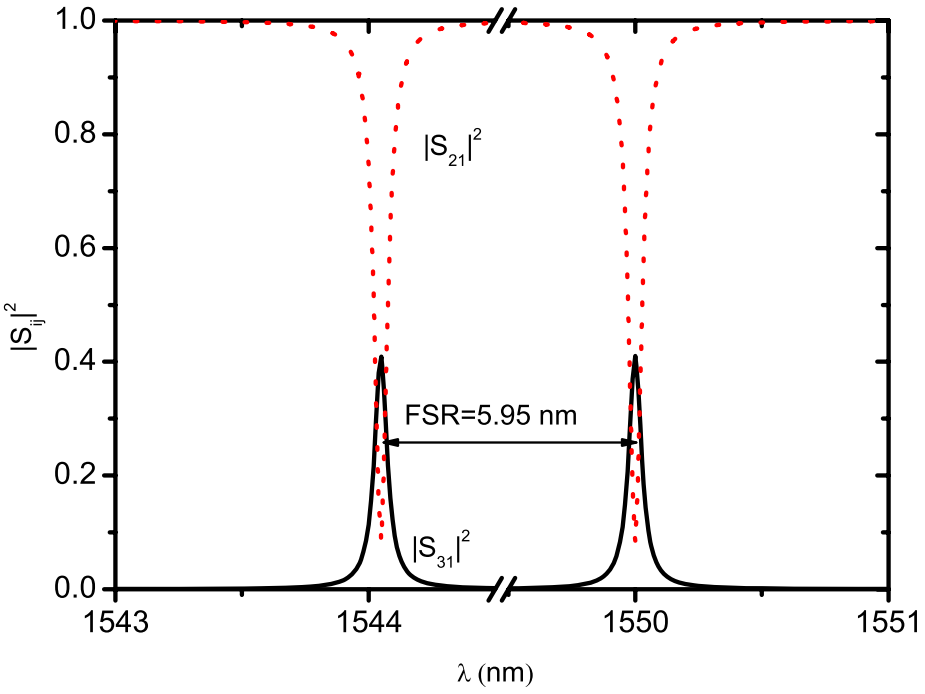

Figure 5.2: Typical normalised intensity profile from port B (dotted line) and port C (solid line) as a function of the wavelength at different output coupling constants ($\zeta_b = \zeta_a = 0.1$ and $\tau = 0.98$ calculated using equations (5.6,5.5), respectively. $R = 20\mu m$ and $n_{eff} = 3.2$.

The behavior of the resonator can be charcaterised by its Q-factor. The Q-factor of the cavity can be approximated as [88]

$$Q \approx \frac{\lambda_0}{\Delta\lambda_{3dB}} = \frac{2\pi^2 n_{eff} R}{\lambda_0 \arccos(\frac{1+(t_a t_b \tau)^2 - 4t_a t_b \tau}{-2t_a t_b \tau})} \tag{5.7}$$

Equation 5.7 is plotted in figure 5.3 as a function of the input coupling coefficient, which shows the drop in Q-factor as the input coupling strength increases. For a symmetrically coupled resonator, the Q-factor is high but the throughout intensity is also high, and this condition does not favour the use of a microcavity as a filter as the signal is still present in the throughput. For a filtering application, the coupling is better at critical coupling as the dropped intensity is at its maximum but it presents a compromise on the cavity Q-factor. However achieving critical coupling is in practice very difficult compared to symmetric coupling so an array of symmetrically coupled ring resonators are used for nulling $|S_{21}|^2$ [93].

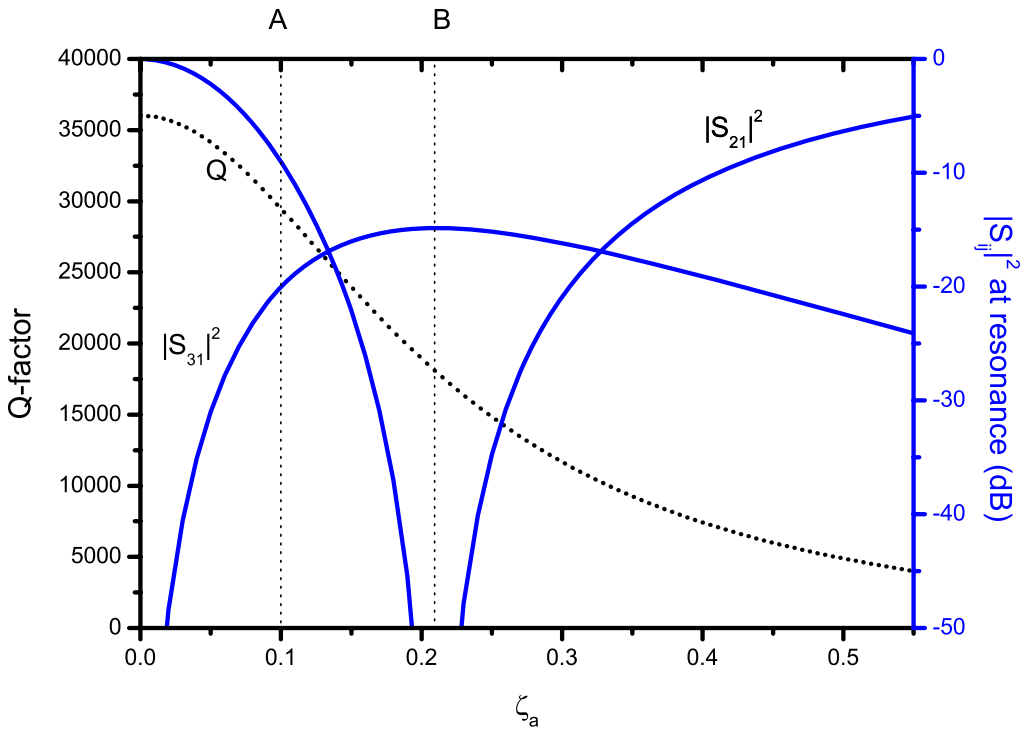

Figure 5.3: Cavity Q-factor and waveguide output intensities at resonance ($\lambda = 1550nm$) as a function of the input coupling coefficient for a lossy ($\tau = 0.98$) ring resonator with $R = 20\mu m$ and $n_{eff} = 3.2$ and $\zeta_b = 0.1$. From the left, the first vertical dotted line (A) marks symmetric coupling while the second one (B) shows critical coupling.

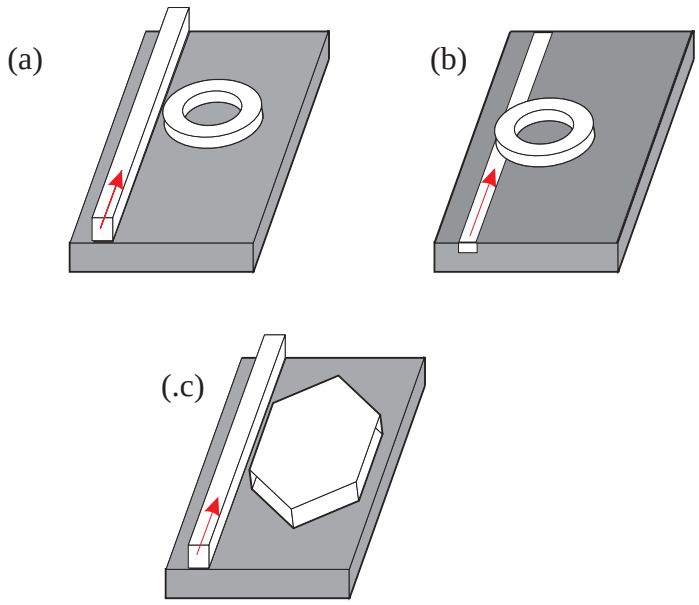

Figure 5.4: lateral coupling for (a) ring resonator, (b) vertically coupled ring/disk microcavity and (c) hexagonal resonator

5.3.1 Input and Output Coupling Mechanism

Mostly, the input and output coupling in and out of the microcavities is achieved via evanescent field coupling. Coupling light into the resonator is achieved by allowing the tail of the evanescent field to extend into the guiding structure of the resonator from a bus waveguide. For coupling out, the evanescent field tail from the resonator is allowed to couple into an output bus guide. Coupling of light in and out in this way is achieved either by lateral or vertical coupling. Figure 5.4 shows a typical geometry for these coupling methods.

When a straight waveguide is brought into the vicinity of the other waveguide, for example ring waveguide, preferential coupling of the mode from the straight waveguide into the ring occurs if the following are satisfied: The propagation vector in the waveguide denoted by k_{wg} must match that in the in cavity denoted by k_{cav} [80, 94]. Since $n_{eff} = f(W_b, ng, ns)$, for example as shown by the normalised frequency ($V = \frac{2\pi W_b}{\lambda}\sqrt{(n_g^2 - n_s^2)}$) and guide index $b = \frac{n_{eff}^2 - n_s^2}{n_g^2 - n_s^2}$ for TE modes [95, 96], tuning either W_b, n_g, n_s will selectively a input mode with a different Θ into the cavity. Normally, both n_s and n_g are fixed while W_b is varied to achieve suitable mode-coupling in the cavity. This is because it is easier to fabricate a waveguide with a variable w rather than to vary the other two constants. Therefore, to couple a mode with $k_{cav}(60^o)$, W_b is varied until $k_{wg}(60^o)$ is achieved [94]. Tuning of the incident angle can also be achieved by the variation of the effective index of

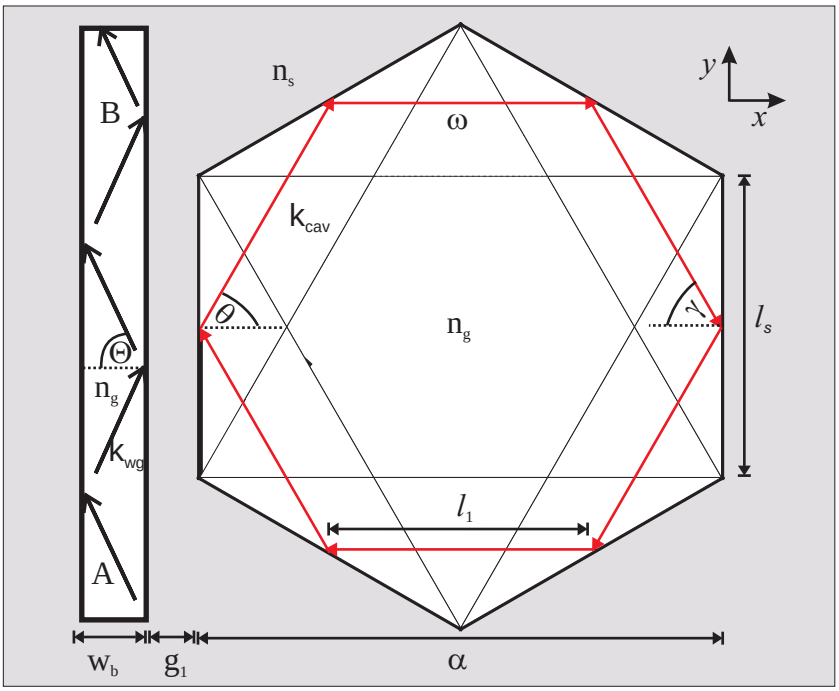

Figure 5.5: Schematic top view of a waveguide-coupled hexagonal microcavity. A bus waveguide of width W_b is displaced from the flat side of the hexagonal microcavity by a distance g_1. Both the cavity and the bus waveguide, with refractive index n_g are immersed in a background medium with refractive index n_s. $k_{wg}(k_{cav})$ is the waveguide (cavity) mode propagation vector. Capital letters A and B denote, respectively, the input and output port of the device

the waveguide for a given W_b.

$$\theta_c < \theta < (120^o - \theta_c) \tag{5.8}$$

Lateral coupling is a popular method since it is easily achievable with the standard fabrication technology such as lithography followed by dry etching. Vertical coupling requires either growth of material on the top surface or wafer bonding before using the standard fabrication tool. However, the latter method does have merits over the lateral coupling when it comes to defining the separation between the guide and the resonator. For vertical coupling, the coupling gap is defined during material growth or bonding and this gap is well controlled and very reproducible. Control over the coupling gap is very crucial as it is one of the factors affecting the coupling strength between the two guides [97].

High confinement of the modes in the bus waveguide and the resonator guide leads to a limited short tail of the evanescent field away from the guide resulting, therefore, for the need for a very small coupling gap and/or a long coupling length.

For micro-ring resonators, aiming for a long coupling length, while maintaining the small radius required for long FSR, is not an option therefore leaving only the option for a very small gap. A microcavity with a long coupling length, see figure 5.4(b) does not need a very small coupling gap as the coupling occurs along the entire flat surface.

Besides the dependence on the coupling gap and coupling length, the coupling strength depends also on the relative width, the relative index contrast between bus guides and resonator guides and also on the wavelength. We mention here this dependence for the lateral coupling, as it affects the coupling efficiency and therefore needs more consideration for the resonator design.

For the case where the index of refraction of the bus guides and the resonator are different, the guide with higher index will tend to confine the modes more than the other one resulting in a very short tail of the evanescent field, hence leading to a small κ from the high index guide to the lower one, for a fixed width and coupling gap. This effect can be used to obtain a high Q microcavity by making the bus waveguide have a low effective index, hence becoming a weak guide and a good coupler to the resonator but not the opposite [97].

Where the width of the bus guide and the resonator guides are comparable, the guide with a small width is effectively a weak guide and the coupling strength out of this guide is high resulting in the same effect as the small index guide discussed above. In the next section the general theory of the whole microcavity is discussed.

5.3.2 Ray optics approach for a hexagonal microcavity

Figure 5.5 shows the schematic top view of a waveguide-coupled hexagonal optical microcavity where W_b and α are the width of the bus waveguides and the lateral cavity width. g_1 is the gap between the bus waveguide and the microcavity and n_g and n_s are the refractive index in the cavity and the surrounding medium, respectively. For this geometrical layout of the microcavity and the bus waveguide, introduction of the optical mode into the microcavity is achieved via lateral evanescent coupling, as discussed in the previous section. In this way evanescent modes from the waveguide, with the correct propagation constant to match the modes of the microcavity, will couple in. The width of the guide and the side length of the microcavity l_s determine the coupling condition while g_1 determines the strength of the coupling. Upon entering the cavity, cavity modes propagate within the cavity via TIR. For these cavity modes, their incident angles θ must satisfy the following conditions, which require that $n_g > n_s$ [94].

In (5.8), $\theta_c = \sin^{-1}(n_s/n_g)$ is the TIR critical angle. Within the cavity, resonance of the optical modes is only possible if the cavity propagating modes complete at least a single cavity round-trip while at the same time, the cavity modes' wavefront is in phase with that of their corresponding source modes.

For the cavity modes to complete a single round-trip, the condition in equation (5.8) has to be satisfied at every cavity-surrounding interface that the mode encounters. If θ is outside the range set by equation (5.8) when arriving on the next interface, the corresponding modes are refractively lost into the surrounding medium. Thus, there exists an even narrower incident angle range which will guarantee at least a six single bounce cavity round-trip in a hexagonal microcavity [98]. We concentrate only on this six bounces partially-confined cavity mode case. For N_c sided polygonal optical microcavity cavities, there are few ideal incident angles, ($\theta_m = \frac{2\pi}{uN_c}, u = 1, 2, \ldots$ and for example $N_c = 6$ for a hexagon) within equation (5.8), for which the cavity loop trajectories are always closed. Closed-loop trajectories refer to ray trajectories that reflect at the same location along the cavity wall after every cavity round trip. In contrast open loop-trajectories drift away from their initial point of reflection along the cavity for every cavity round trip, the so called walk-off condition, until they escape the cavity via refraction [94, 99]. The resulting relative displacement (ΔX) from the starting position, due to the walk-off conditions is given in equation (5.9) [94].

$$\Delta X = 3\sqrt{3\alpha}\frac{\sin(60^o - \theta)}{\cos\theta} \tag{5.9}$$

The material used for the hexagonal cavity ($N_c = 6$)considered in this work has a high refractive index relative to that of the surrounding medium which is enough to avoid refractive transmission outside the cavity when the beam is incident on the cavity wall for $\theta \approx \theta_m$ [100]. When θ drifts away from θ_m, open-loop cavity trajectories result and these cavity modes can only lead to cavity mode resonance provided that they are wavefront matched [94]. For a hexagonal microcavity, the total path traveled by the six-bounce wavefront-matched cavity modes, open or closed, over a single cavity-round trip, is given in equation (5.10) [94].

$$L(\theta) = 3\alpha\sin(30 + \theta) \tag{5.10}$$

Open-loop cavity mode life-time, measured as the number of bounces (N) the modes undergo before refracting from the cavity into the surrounding medium, has been shown to increase as θ approaches θ_m[94]. $L(\theta)$ is independent of the starting position of the propagation mode along the cavity side. For open-loop trajectories, a different N for

a given θ has been shown to give rise to multiple modes which results in an undesired broadening of the resonance line width [99].

For a given free space wavelength (λ_o), resonance of the given mode, defined by θ inside the hexagonal cavity, has to satisfy the wavefront matching condition (5.11) [94, 99].

$$k_o n_g L(\theta) + 3\Phi_F(\theta) + 3\Phi_F(120 - \theta) = 2\pi m_\omega,\ m_\omega = 0, 1, 2, 3, \ldots \tag{5.11}$$

In equation (5.11), k_o is the free space propagation constant ($k_o = 2\pi/\lambda_o$) and m_ω is an integer representing the number of resonating wavelengths along $L(\theta)$ within the cavity. In cavity mode terms, m_ω is referred to as the azimuthal mode order. $\Phi_F(\theta)$ is the Fresnel phase shift, upon a single reflection on the cavity wall, experienced by the mode when undergoing TIR and it is given as equations (5.12, 5.13) for a given mode polarization [51].

$$\Phi_p(\omega, \theta) = 2\tan^{-1}\frac{n_c\sqrt{\sin^2\theta - \sin^2\theta_c}}{n_g\cos\theta} \tag{5.12}$$

$$\Phi_s(\omega, \theta) = 2\tan^{-1}\frac{\sqrt{\sin^2\theta - \sin^2\theta_c}}{\cos\theta} \tag{5.13}$$

In equation (5.12, 5.13), p and s refer to the polarization angle (γ) of the plane wave parallel and perpendicular to the plane of incidence, respectively. Referring to the laboratory coordinate system in figure (5.5), the plane of incidence lies along the x-y plane. $\Phi_F(\theta)$ is a function of θ, γ, n_g and n_c at a given angular frequency ($\omega = 2\pi/\lambda_o$) and it can attain any value between zero and $|\pi|$ for the values of $\theta > \theta_c$ [101]. Only when the condition in equation (5.11) is satisfied can a signal build up within the cavity. We focus on the solution of equation (5.11) for $\theta = 60^o$, for which the condition in equation (5.8) is satisfied. At this angle, the round trip trajectory will always be closed, hence avoiding the walk-off condition. Also, by choosing the correct launching position along the cavity side wall, an equal interface to interface length ($l_1 = L(\theta)/6$) traveled by the wave during TIR can be found.

The choice of the hexagonal shape microcavities has been justified in the introduction section, however the sharp corners of this geometrical shape introduce loss as compared to those cavities without sharp corners, such as the circular ones. High losses will lead to a broader resonance line-width ($\Delta\lambda_{FWHM}$) and hence to a lower Q factor

$$Q = \frac{\lambda_R}{\Delta\lambda_{FWHM}} \tag{5.14}$$

thus lowering the efficiency of the device. In equation (5.14), λ_R is the resonance wavelength. However, side length for a hexagonal cavity

$$l_s = \frac{\alpha}{\sqrt{3}} \tag{5.15}$$

relaxes the small coupling gap bottleneck, which proves to be a challenge during fabrication. Only part of l_s, which is still bigger than that of the microcircular resonator, will be effective during couping. Therefore the actual corners of the hexagonal cavity can be rounded off without affecting many of the cavity properties, while lowering the losses and hence increasing the Q factor.

The main aim of this work is to harness the enhanced optical power within the microcavity for nonlinear applications. In the following section we therefore link the above known microcavity behavior with the requirements for the effective nonlinear phenomena to occur. We will focus on second harmonic generation in nonlinear optical materials.

5.4 Simulations

The demand for all-optical-circuits to be an equivalent to electronic circuits has forced the size reduction of many optics components into the micrometer range, and lower, such that the integration between these components is effective. At the same time, the geometrical shape of these micrometer sized components becomes more complex and so too is the theoretical description of their operation. Experimental work on this scale proves to be more challenging and therefore numerical methods such as the beam-propagation-method (BPM) and finite-difference time domain (FDTD), amongst others, have found widespread application in studying these components prior to their experimental realisation. The choices of which method to use depends on the nature of the component functions, for example the BPM is applied for components with low index contrast along the direction of propagation and therefore does not include reflection during propagation. BPM is therefore not applicable to cavity studies where back propagation and high-index contrast form the basis of the device.

The FDTD approach solves, numerically, the direct solution of Maxwell's time-dependent curl equations over space and time. As the FDTD does not have the above limitation it is suitable for most complex structures and arbitrary propagation schemes. This numerical method was therefore selected for our studies of the hexagonal microcavity. The FDTD formulation is outlined below.

5.4.1 FDTD formulation

Consider a loss-less structure, which assumes the absence of volume current and finite conductivity. Let its optical properties be time-independent throughout. The Maxwell

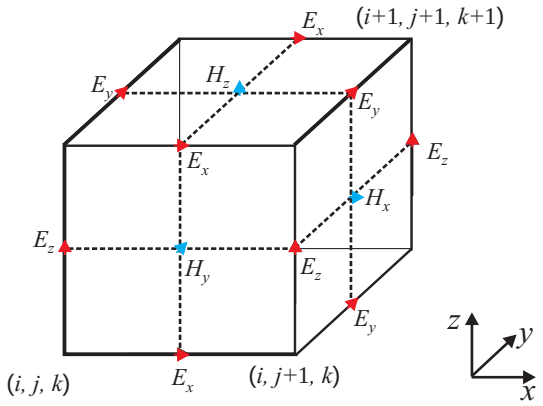

Figure 5.6: Yee lattice used for FDTD unit cell

curl equations are written as

$$\mu \frac{\partial \mathbf{H}}{\partial t} = -\nabla \times \mathbf{E} \tag{5.16}$$

$$\epsilon \frac{\partial \mathbf{E}}{\partial t} = \nabla \times \mathbf{H} \tag{5.17}$$

The Maxwell curl equation implies that the time variation of the **H**-field (**E**-field) in time depends on the space variation of the **E**-field (**H**-field). As an example, with the knowledge of the spatial **E**-field local distribution at a given time and the stored value of the **H**-field, the value of the **H**-field for a future time can be determined. At time $t = 0$, the field distribution is given and known everywhere in the structure. The structure is placed in a discrete spatial volume domain represented by equation (5.19) and a discrete time interval domain ($n\Delta t$), where i, j, k are integers and $\Delta x, \Delta y$, and Δz are space increments while the time increment is $k\Delta t$ for an integer values of n. The field functions in this discrete domain take the form shown in equation (5.19).

$$(x, y, z) = (i\Delta x, j\Delta y, k\Delta z) = (i, j, k) \tag{5.18}$$

$$f(x, y, z, t) = f(i\Delta x, j\Delta y, k\Delta z, n\Delta t) = f^n(i, j, k) \tag{5.19}$$

For the computation of the FDTD algorithm, in the Cartesian computational grid, the **H** and **E**-fields are staggered in the spatial domain such that the **H**-field component is halfway between a pair of the **E**-field components, as show by the Yee lattice in figure 5.6. The **E**-field and **H**-field occupy the edge and the face of the cube respectively.

The central differential approximation is then used to approximate the partial differentiation in the above Maxwell curl equation and the solutions are given for example by

[102, 103] and reproduced below for completeness. The FDTD procedure is as follows: the stored component of the $\mathbf{H}^{n-\frac{1}{2}}$-field and the spatial variation of the $\mathbf{E}$ -field in the present time, $t = n$, are used to determine the $\mathbf{H}$-field components at $t = n + \frac{1}{2}$. This will give the known spatial distribution of the $\mathbf{H}$-field components in the new time, which are then used to determined the $\mathbf{E}$-field components in time.

$$
\begin{aligned}
H_x^{n+\frac{1}{2}}(i,j,k) &= H_x^{n-\frac{1}{2}}(i,j,k) \\
&+ \frac{\Delta t}{\mu \Delta z}\left(E_y^n(i,j,k) - \left(E_y^n(i,j,k-1)\right)\right) \\
&- \frac{\Delta t}{\mu \Delta y}\left(E_z^n(i,j,k) - \left(E_z^n(i,j-1,k)\right)\right) \qquad (5.20) \\
H_y^{n+\frac{1}{2}}(i,j,k) &= H_x^{n-\frac{1}{2}}(i,j,k) \\
&+ \frac{\Delta t}{\mu \Delta x}\left(E_z^n(i,j,k) - \left(E_z^n(i-1,j,k)\right)\right) \\
&- \frac{\Delta t}{\mu \Delta z}\left(E_x^n(i,j,k) - \left(E_x^n(i,j,k-1)\right)\right) \qquad (5.21) \\
H_z^{n+\frac{1}{2}}(i,j,k) &= H_x^{n-\frac{1}{2}}(i,j,k) \\
&+ \frac{\Delta t}{\mu \Delta y}\left(E_x^n(i,j,k) - \left(E_x^n(i,j-1,k)\right)\right) \\
&- \frac{\Delta t}{\mu \Delta x}\left(E_y^n(i,j,k) - \left(E_y^n(i-1,j,k)\right)\right) \qquad (5.22) \\
E_x^{n+1}(i,j,k) &= E_x^n(i,j,k) \\
&+ \frac{\Delta t}{\epsilon \Delta y}\left(H_z^{n+\frac{1}{2}}(i,j+1,k) - \left(H_z^{n+\frac{1}{2}}(i,j,k)\right)\right) \\
&- \frac{\Delta t}{\epsilon \Delta z}\left(H_y^{n+\frac{1}{2}}(i,j,k+1) - \left(H_y^{n+\frac{1}{2}}(i,j,k)\right)\right) \qquad (5.23) \\
E_y^{n+1}(i,j,k) &= E_y^n(i,j,k) \\
&+ \frac{\Delta t}{\epsilon \Delta z}\left(H_x^{n+\frac{1}{2}}(i,j,k+1) - \left(H_x^{n+\frac{1}{2}}(i,j,k)\right)\right) \\
&- \frac{\Delta t}{\epsilon \Delta x}\left(H_z^{n+\frac{1}{2}}(i+1,j,k) - \left(H_z^{n+\frac{1}{2}}(i,j,k)\right)\right) \qquad (5.24) \\
E_z^{n+1}(i,j,k) &= E_z^n(i,j,k) \\
&+ \frac{\Delta t}{\epsilon \Delta x}\left(H_y^{n+\frac{1}{2}}(i+1,j,k) - \left(H_y^{n+\frac{1}{2}}(i,j,k)\right)\right) \\
&- \frac{\Delta t}{\epsilon \Delta y}\left(H_z^{n+\frac{1}{2}}(i,j+1,k) - \left(H_z^{n+\frac{1}{2}}(i,j,k)\right)\right) \qquad (5.25)
\end{aligned}
$$

The choice of both the spatial and time step size, that is the grid size and time step, affects the accuracy and the stability of the calculation respectively. To achieve the desired accuracy, the grid size needs to be small enough to resolve the smallest feature in the

structure and must be smaller than the wavelength used in the calculation. This grid size requirement is clearly at the expense of computational time as the calculation complexity increases proportional with its reduction. Normally, convergence studies are performed for each problem, in which the grid size is reduced while monitoring the output values until these values approach a limiting value. The stability of the simulation is limited by the choice of the grid size, hence limiting the choice of the time step as shown below, where the time step Δt has to be smaller than the stability limit Δt_s given as

$$\Delta t_s \leq \frac{1}{c}\left(\frac{1}{\Delta x^2}+\frac{1}{\Delta y^2}+\frac{1}{\Delta z^2}\right)^{-1/2} \tag{5.26}$$

Due to the finite nature of the FDTD, care must be taken at the boundary of the calculation window as the FDTD cannot evaluate the field at this location since it will need field information outside the calculation window. At the start plane, this restriction is relaxed by setting every field component before this plane to zero while, at the other five planes of the calculation window, for 3D in general, the field must be absorbed to avoid it being reflected back into the calculation window. For the following simulation results, a perfect matching layer (PML) method was applied to all of the calculation windows. The PML, with a known width and reflectivity is added at the boundary of our calculation window to absorb the radiated field from within the calculation window (see ref [104]).

In the PML region, the electromagnetic wave propagates without reflection and an exponentially decreasing amplitude. PML formularization is governed by the following trasnformation:

$$\frac{\partial}{\partial x} \rightarrow \frac{1}{1+i\frac{\sigma_x(x)}{\omega}}\frac{\partial}{\partial x} \tag{5.27}$$

In 5.7, $\sigma_x(x)$ is the PML absorption coefficeint which is set at is zero in the calculation window but positive in the PML region [105]. $\frac{1}{\omega}$ is there to make the PML effect independent of the wavelength, and for example the attenuation rate in the PML region will be the same for all w for a given $\sigma_x(x)$ function [106]. The effect of the PML for a given waveform $exp(-ikx)$ as shown in figure 5.7, is to replace x by $x(1+i\delta_x)/\omega$. The PML is then defined within the calculation region at the region of interest by making the function δ_x in the x direction to be zero anywhere before the PML layer and greater than zero in the $+x$ axis from the PML layer outward.

The PML absorbs waves with real propagation constants effectively but it fails when it comes to evanescent waves. This is because evanescent waves have an imaginary k value and this wave oscillates on passing through the PML layer [106]. Though the evanescent wave is of a decaying nature, which then suggests putting the PML far from for the wave

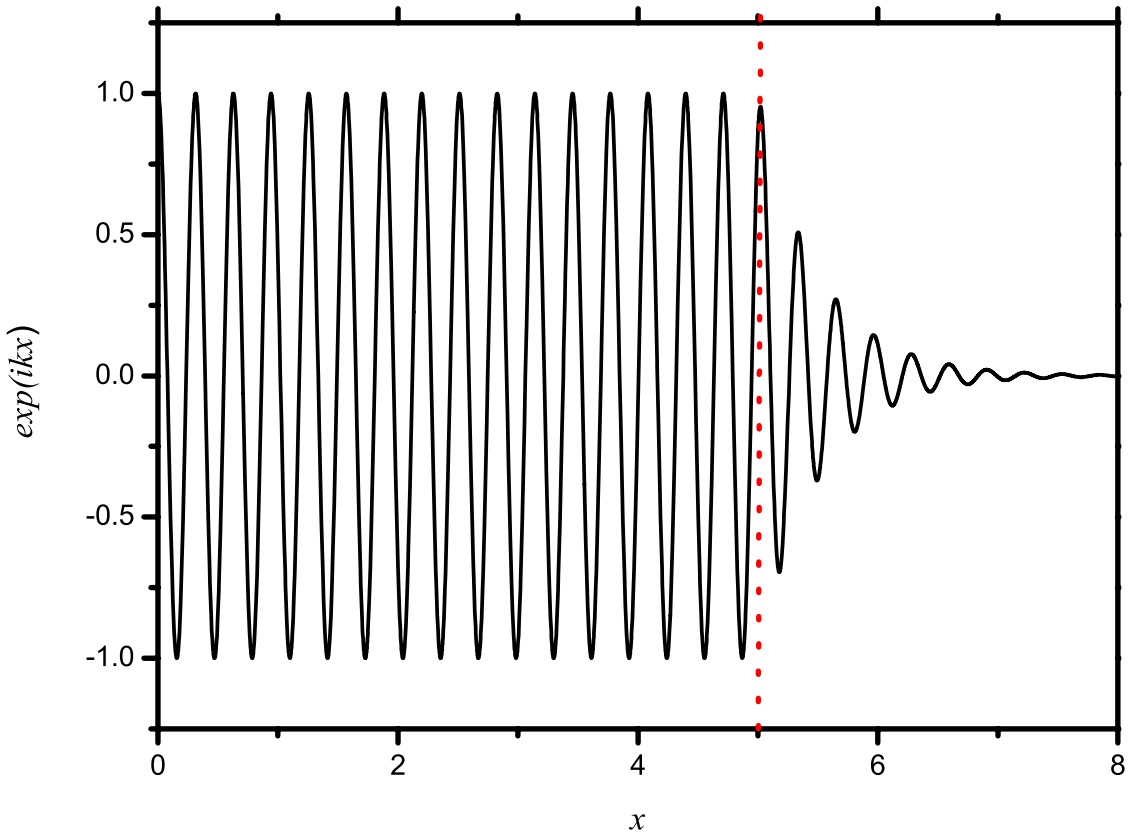

Figure 5.7: Effect of the PML layer on the wavefunction along the propagation direction. The PML starts from $x = 5$ by making $\sigma_x(x < 5) = 0$ and $\sigma_x(x > 5) > 0$

the evanescent wave will propagate and decay completely before getting to the PML, this will be in the expense of the computational window and hence time. A compromised is made in PML formalization to deal with evanescent waves with a fast decay rate by making δ_x complex [106].

The width and reflection coefficient are specified to control the function of the PML. A think width results with a slowly decaying wave as opposed to a perfect conductor with a zero thickness. Perfect conductor force the wave to decay very fast and can cause instability in the calculation. The reflection coefficient is also specified to determine the reflection of the boundary layer. For evanescent wave case, a constant is normally defined which the make the δ_x complex.

In the next section the simulation results for the hexagonal microcavity are shown. Since the aim is to use this hexagonal microcavity for nonlinear applications, the size of the microcavity is carefully selected such that it is also suitable to resonate the resulting nonlinear generated wave. The details of selecting this cavity size will not be discussed in this chapter but will be presented in chapter 7. Therefore, for the remaining sections of this chapter, the focus will be on the simulation results of the linear device.

5.5 Simulation Results for the Hexagonal Microcavity

We have used a commercial FDTD package for our calculations. Here, we only consider 2D calculations of our devices. Our hexagonal microcavities have the same properties as bulk, congruent, z-cut $LiNbO_3$ crystal. The aim here is to study the maximum cavity response without the influence of the input and output coupling condition, such as the coupling length and coupling gap. Therefore, the input and output buses are excluded in the calculation window leaving only the microcavity, as shown in figure 5.8. The refractive index of our hexagonal microcavity at the fundamental wavelength (FW) corresponds to the extraordinary refractive index of $LiNbO_3$, n^e_{LN} [7] for the appropriate value of λ. The refractive index of the surrounding, n_a, is that of air.

To detect the response of the cavity, a monitor was located inside the cavity at one of the sharp corners of the hexagon, as shown in figure 5.8. This monitor allowed measurements of the field components, power, or the energy density at that position in the cavity per time. The length of the monitor $l_m = \frac{2\alpha}{3\sqrt{3}}$ was selected such that the monitor extends to cover the width of the area occupied by the long lived cavity modes, colored white in figure 5.8. In this figure, the whole of the hexagon has the same refractive index including the inner gray part. This inner gray part is not occupied by the long lived cavity modes [82] and the difference in colorings is merely intended to show

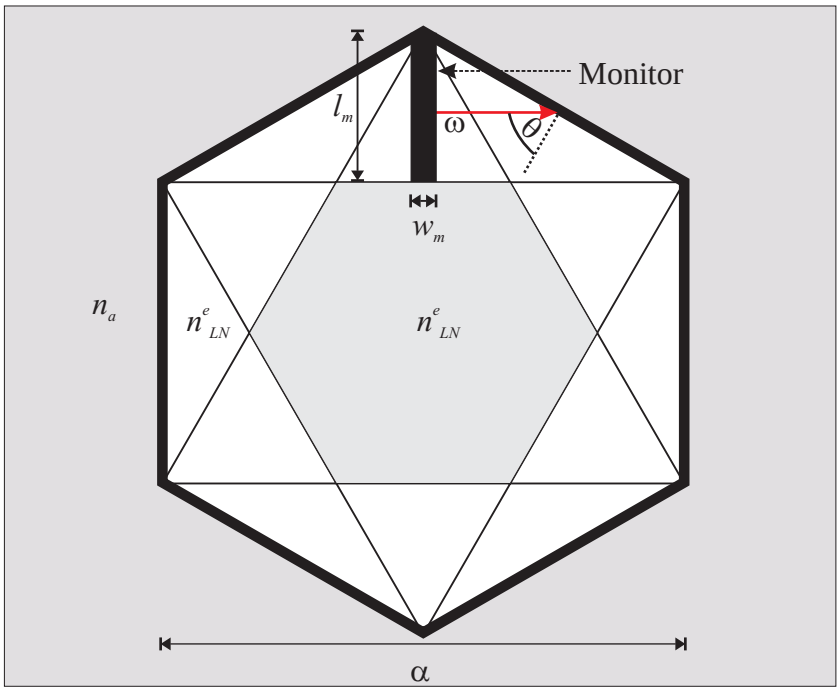

Figure 5.8: 2D schematic layout of the hexagonal microcavity in the FDTD simulation. The launch position of the incident beam is located at the center of the width of the detection monitor as shown by a red arrow representing the k vector of the launch mode

this occupancy effect. The direction of the monitor is such that this monitor is optimised for any signal normal to the plane containing l_m. The width of the monitor w_m was kept at a constant value as this dimension did not influence the monitor response for our calculations. The desired beam type, cw, pulsed or impulse, with transverse width = l_m was launched in the middle of the monitor such that the beam was incident on the next wall, at an incident angle θ, as shown in figure 5.8. We have used an ultrashort pulsed beam type for cavity spectral studies while a cw beam was used for the steady-state simulations.

We have adopted the grid size as $\frac{\lambda}{n_e(\lambda)C}$, C being a constant giving rise to the convergence for a given α. In this work, a suitable value of λ within the Ti:sapphire wavelength-source range (650nm to 1100nm) was used to obtain a corresponding resonating cavity size satisfying equation (5.11). In this chapter, $\alpha = 2.97\mu m$ will be used throughout, which corresponds to the resonance of the s-polarized of the fundamental wave (FW) with $\lambda = 0.959\mu m$. It will be shown in the next chapter that this cavity size also allows resonance of the generated second harmonic and for phase matching to take place. For the rest of this chapter, where α will remain almost constant, $C = 36.81$ was

used throughout.

Smaller structures are preferred for FDTD calculation as they reduce the duration of the simulation for more accurate results. Smaller structures are used for the general cavity properties while in the next chapter, larger structures will be used for estimation of the SHG efficiency as they have lower radiation losses compared to the small ones.

5.5.1 Cavity spectrum

Figure 5.9 shows the cavity spectrum, for the hexagonal microcavity with $\alpha = 2.97\mu m$, designed to resonate an s-polarized FW with $\lambda = 0.959\mu m$. The spectrum was obtained by launching a 10 fs Gaussian pulse centered at $\lambda = 0.959\mu m$ in the cavity and performing a fast Fourier transform on the recorded results. The pulse width used was wide enough to cover at least three multiples of the cavity FSR expected at given values of α and λ. The spectral resolution $\frac{1}{t}$ is limited by the duration of the simulation (t). The FSR of the cavity obtained from figure 5.9 is 49 nm and it is comparable to that estimated by assuming a six bounce wavefront-matched trajectory within the microcavity with $\theta = 60^o$ as FSR= $\frac{\lambda}{3n_e^{\omega}\alpha} = 48$ nm.

The cavity lifetime of the resonating mode is limited mainly by the optical radiation losses due to the corners of the hexagon, which limit the Q factor to about 180 for the above cavity size. The Q factor is obtained by fitting a Lorentzian function on the resonance peak in figure 5.9 and extracting the $\Delta\lambda_{FWHM}$. Since the intention for this optical polygonal microcavity is to utilize the cavity gain to enhance nonlinear processes, then improving the Q factor and minimizing the optical losses is essential. It has been demonstrated that rounding the corners of the polygonal microcavities reduces the optical losses and increases the Q factor [107, 108]. However, it was also shown that rounding the corners shifted the position of the resonance wavelength away from that of a regular non-rounded polygonal microcavity. The latter effect will affect the efficiency of the nonlinear process if the shifts of the resonance wavelength on the individual beams involved in the nonlinear interactions within the cavity are not compensated. In the next section, the effect of rounding the corners of the above hexagonal microcavity on the Q-factor, the resonance wavelength and the FSR is summarised.

5.5.2 Reducing Cavity losses

Figure 5.10 shows a schematic top view of a regular and a rounded hexagonal microcavity. In the simulation domain, rounding of the corners of the hexagonal was achieved by

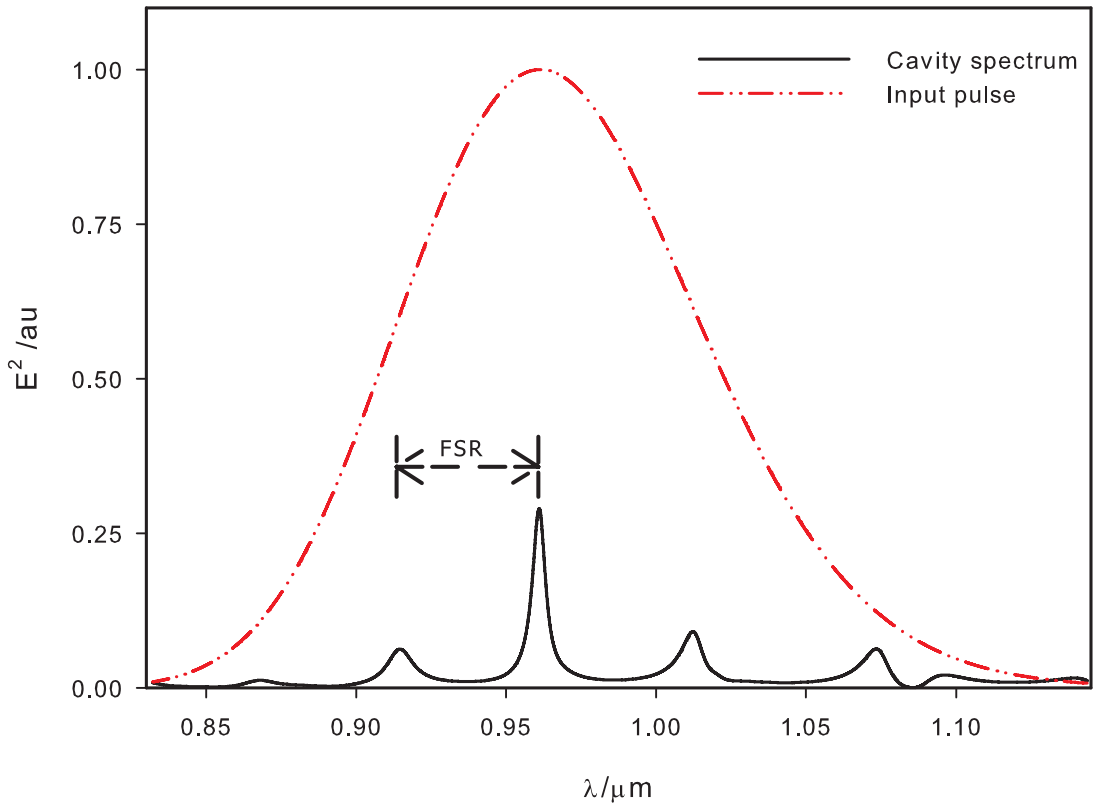

Figure 5.9: Cavity response for s-polarized FW in a cavity with incident $\lambda = 0.959\mu m$ and $\alpha = 2.97\mu m$, FSR = 49 nm

introducing a circle, with the same refractive index as the hexagon, at each corner of the hexagon while reducing l_s such that only an arc with 60^o arc-angle completed the boundary of the hexagon by joining each pair of the straight segments of the hexagon with length l_s given by equation 5.15. R is the radius of curvature of the circle and it varies from 0 to $\frac{1}{2}\alpha$ corresponding to regular hexagonal and circular microcavities respectively. R and l_s are related by equation (5.28).

$$l_s = \frac{\alpha - 2R}{\sqrt{3}} \tag{5.28}$$

When calculating the rounding effects, the launching position was optimised for values of R in 5.28 along the length of the position of the detector, shown in figure 5.8. This was necessary as the launching and the detection point are within the cavity and hence if the launching position does not lie on the path of the returning resonating modes the

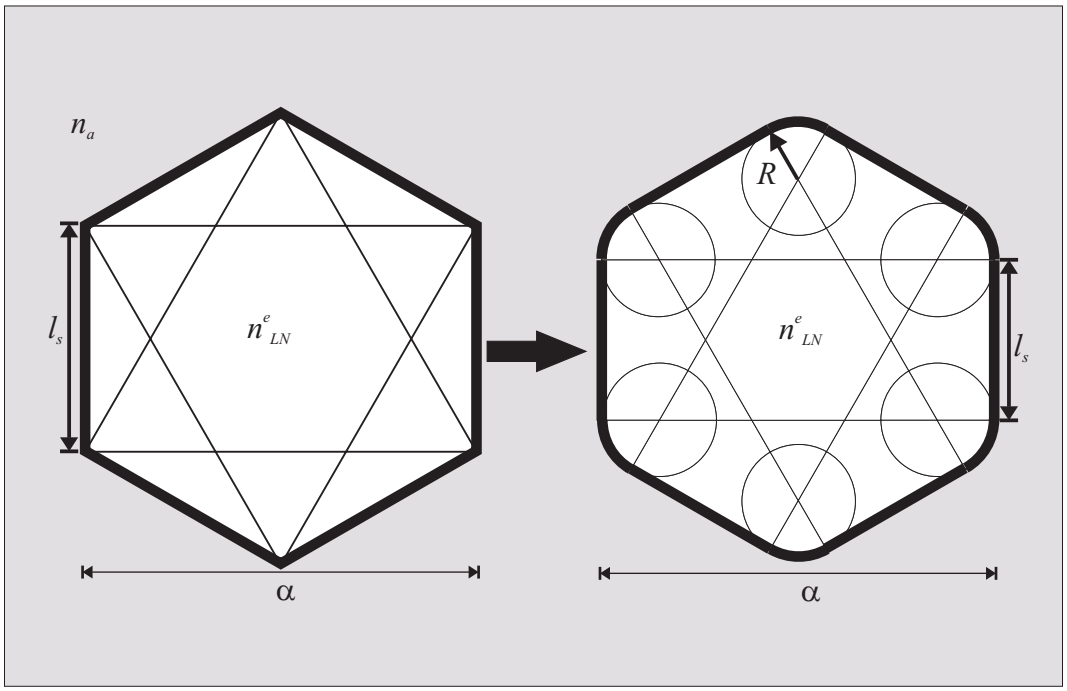

Figure 5.10: Schematic top view of a regular and a corner-rounded hexagonal microcavity

coupling between the two modes will be compromised. The grid size was kept constant at 12 nm throughout the rounding effect studies.

Figure 5.11 shows the curve fitting on the resonance peaks after rounding the corners of the hexagon. The percentage rounding value is also included in this figure either on top of the corresponding peak or color coded to the resonance peak.

With more rounding, the Q-factor rises, which implies that radiational optical losses due to the hexagonal corners are reduced, as shown in figure 5.12. The limitation of the Q-factor at $\frac{R}{\alpha} = 50\%$ is no longer due to the corners but due to the bending losses, which are a function of the index contrast and the size of the cavity. Thus, for the same wavelength, the Q-factor can be increased by increasing the cavity size, which reduces the bending losses. The latter Q-factor dependence will form part of the basis of the next chapter 8 where it will be discussed.

In figure 5.12, there seems to be non-smooth increase of the Q-factor with the rounding near $\frac{R}{\alpha} = 50\%$, this may be due to relationship between the the resonating wavelength and the size of the cavity. Though the correct resonating wavelength was found for values of $\frac{R}{\alpha}$, the cavity size may have not been ideal for resonating wavelength as compared to those with the small rounding values.

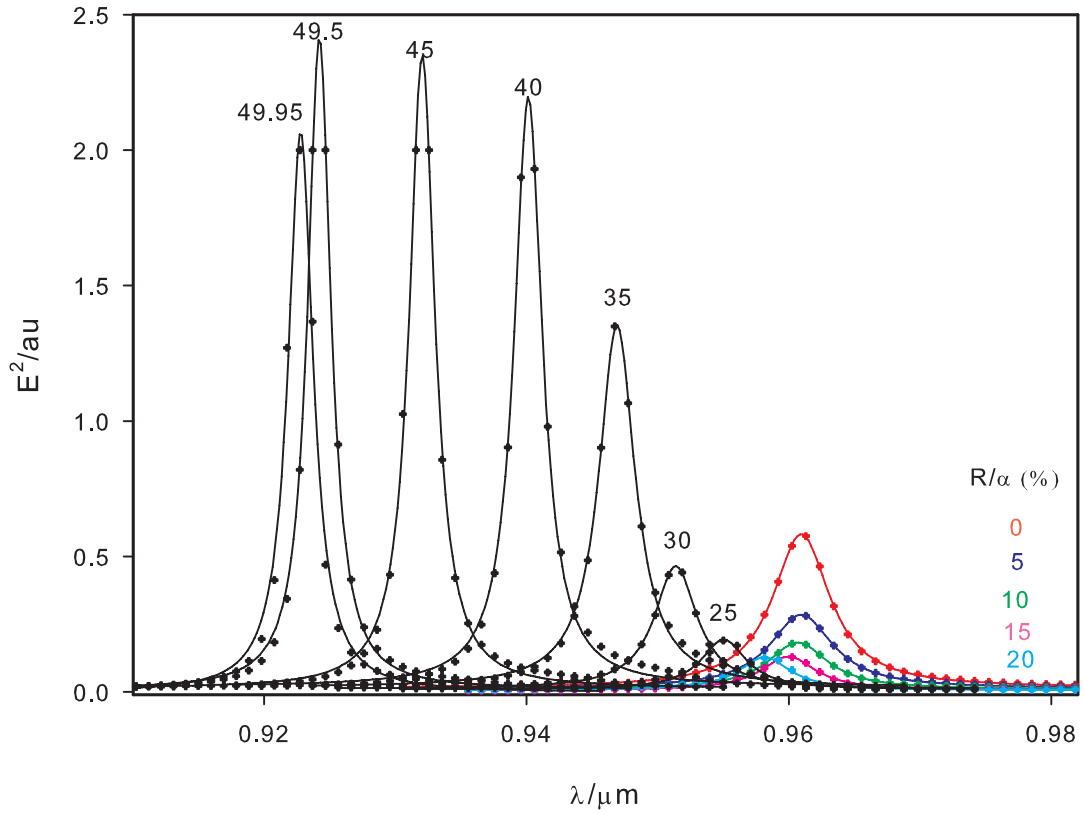

Figure 5.11: Curve fitting for the Q factor determination as a function of the corner rounding. The numbers within the area of the graph are of the corresponding cavity rounding

Due to the increment of the total length traveled by the modes per rounding, the resonance wavelength shifts to smaller values. The wavelength shift extracted from the resonance position in figure 5.11 is shown in figure 5.13. Above 20% rounding the resonance wavelength shifts become more pronounced, which may be due to the migration of the cavity's six bounce modes to a higher number of bounces per round trip until whispering gallery modes (WGM) are formed. WGMs cling to the cavity walls along the propagation direction and are more favoured to have a high Q-factor in a rounded cavity.

With further rounding, more long-lived modes in the cavity are expected, as was shown in figure 5.1b, as compared to a few that must satisfy the six-bounce wavefront-matched behavior in a regular hexagonal cavity. Thus, though the rounding increases the Q-factor, it also increases the number of long lived modes in the cavity. This is shown in figure 5.14

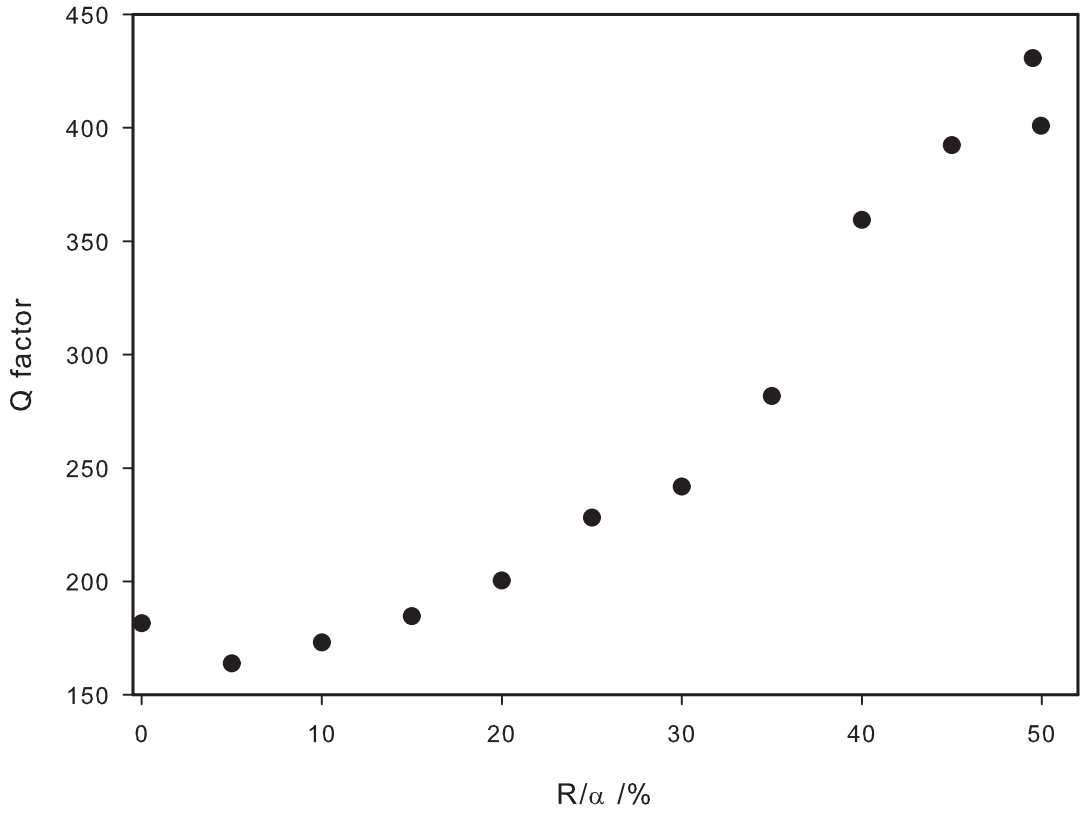

Figure 5.12: Dependence of the Q-factor on the rounding of the hexagonal corners for $\alpha = 2.97\mu m$

by the decrease in the FSR as the rounding is increased so that more long-lived modes are accommodated. The FSR values for $\frac{R}{\alpha} \leq 20$ in figure 5.14 are in between 48 nm and 49 nm and they are comparable to a value of 48 nm predicted before. Also, the decrease in the FSR away from that estimated using the six bounce trajectory estimation confirms the migration to the WGM as shown in figure 5.14. The small error ($1nm$ variation at most) on the FSR values within $\frac{R}{\alpha} \leq 20$ may be due to the insufficient number of points making the resonance peaks in figure 5.11, for this case the resonance are peaks not clearly defined and hence results in more variation between the resonance peaks.

From the above discussion on the effect of the rounding on the wavelength shift and FSR, it can be concluded that the six bounce trajectory is valid up to the $\approx 20\%$ rounding. In the next chapter, the rounding will be limited to this number, as the aim there will be to show the use of a hexagonal microcavity for nonlinear optical processes with six bounce

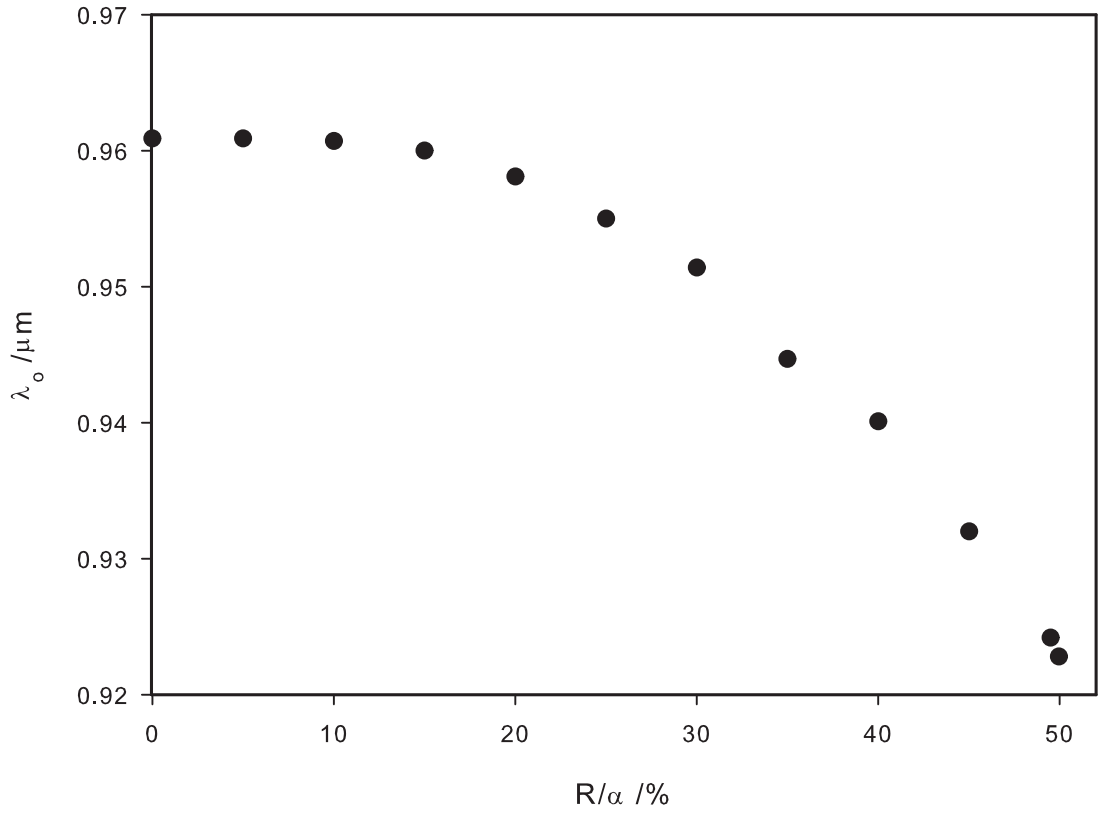

Figure 5.13: Resonance wavelength shift as a result of the rounding of the hexagonal corners for $\alpha = 2.97\mu m$

trajectories per cavity round trip.

5.6 Steady-state simulation

The steady-state of the cavity was obtained by launching a cw wave with a λ values corresponding to the resonance wavelength obtained from figure 5.11. Since the λ corresponds to the resonance wavelength, cavity build-up is expected until the cavity gain balances the cavity loss per round trip whereby the signal within the cavity will be constant. For these simulations, the grid size and transverse width of the input beam were kept the same, as described above.

Figure 5.15 shows the steady state results for a regular hexagonal microcavity with $\alpha = 2.97$ and $\lambda = 0.960\mu m$, obtained from the FDTD simulations. For this cavity, the

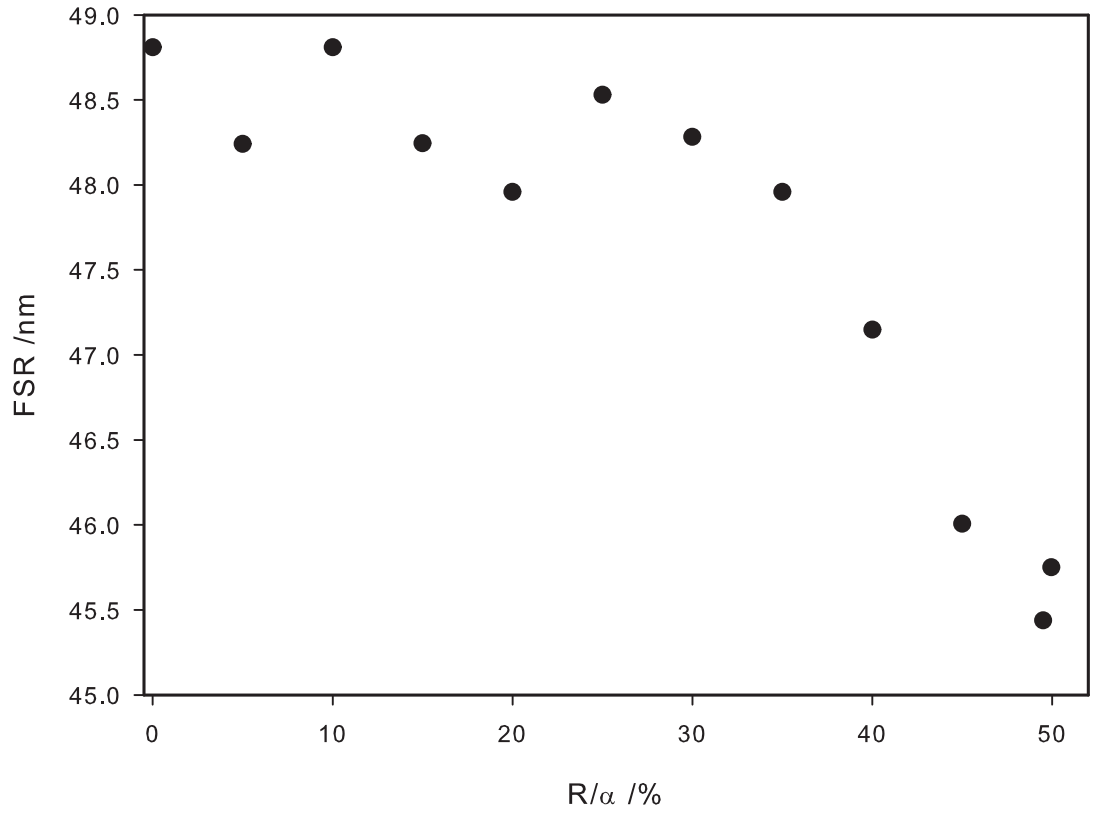

Figure 5.14: FSR as a function of the rounding for $\alpha = 2.97\mu m$

steady state is reached after 10 round trips. With the corners of the hexagon rounded, the number of round trips, before achieving the steady state, is expected to increase.

Figure 5.16 and 5.17 shows the resulting cavity modes at steady state for $\frac{R}{\alpha} = 0, 10, 20, 30, 40,$ and 45.95%. As expected, the cavities show lower optical losses at the corners when the rounding increases. However, due to the small size of the cavity, it can also be seen that the bending losses are also high for these microcavities.

From the launch position in the clockwise direction the intensity field is higher but decrease as mode propagate around the hexagon. The sharp corners are sources of optical loss. For small cavity size, this corner also results with mode reflected into the cavity center than the bigger cavity, thus the mode pattern at the center of the cavity will be less in a large cavity. As R/α increases the mode behave like WGM and clings along the perimeter of the microcavity resulting with less reflection at the center of the cavity.

It is observed from the results that hexagonal corners of a regular hexagon results

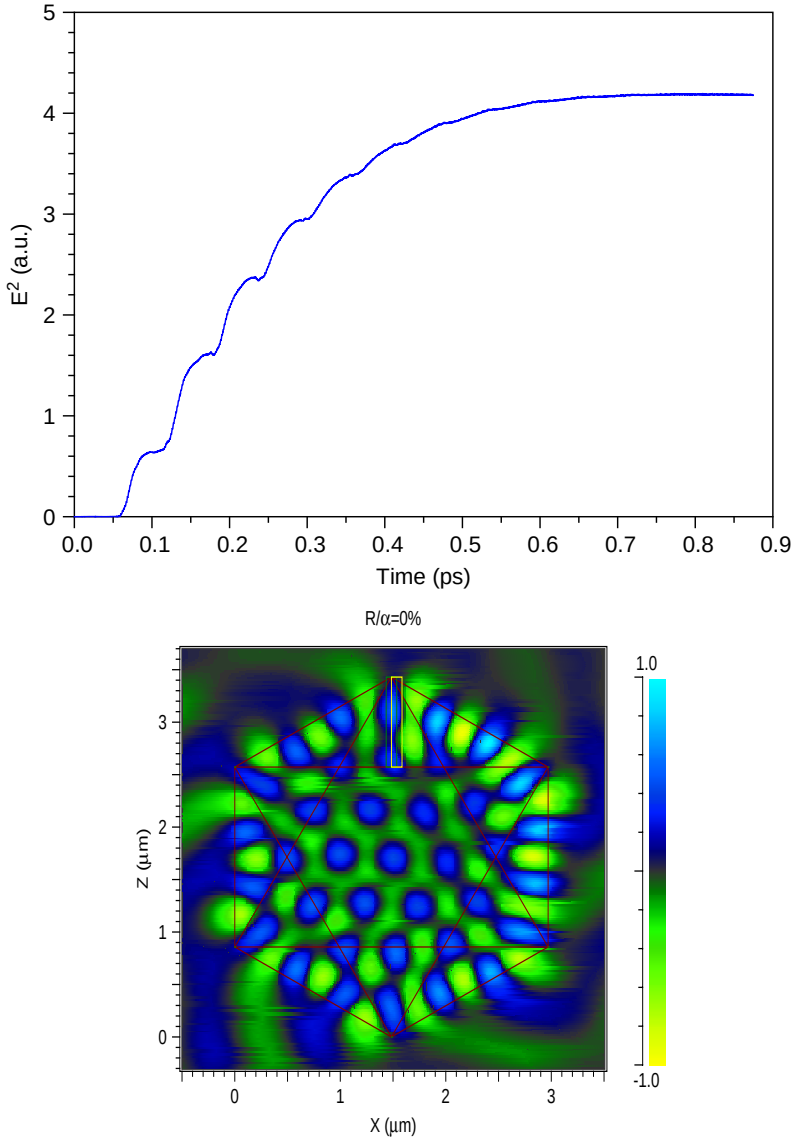

Figure 5.15: Numerical simulation of the regular hexagonal microcavity at resonance with $\alpha = 2.97\mu m$ and $\lambda_o = 0.960\mu m$. Top: intensity build-up within the cavity until steady state is reached. Bottom: Steady state mode field pattern showing increased scattering at the corners of the cavity.

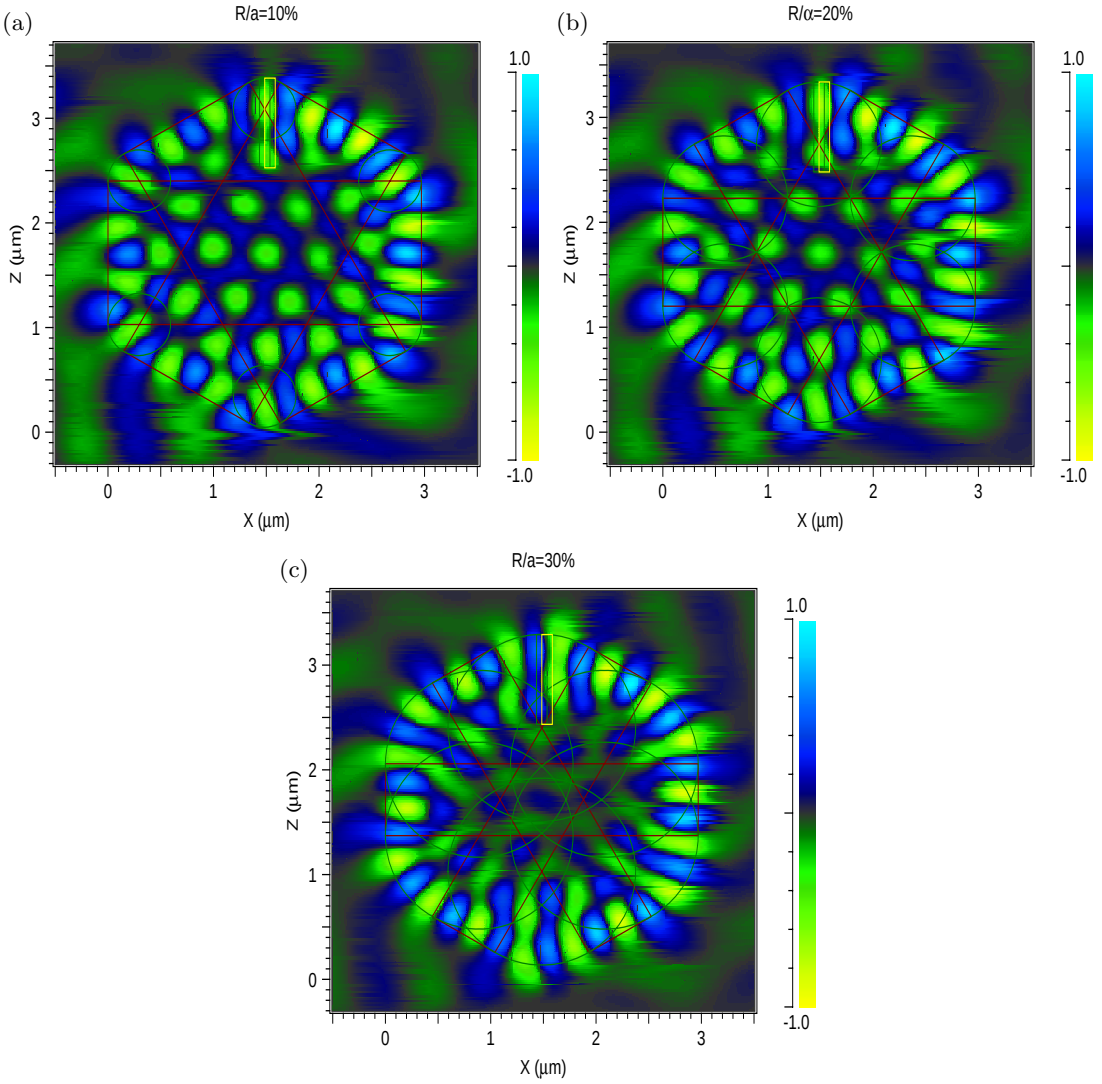

Figure 5.16: Cavity modes for hexagon microcavity with different rounding $\alpha = 2.97\mu m$

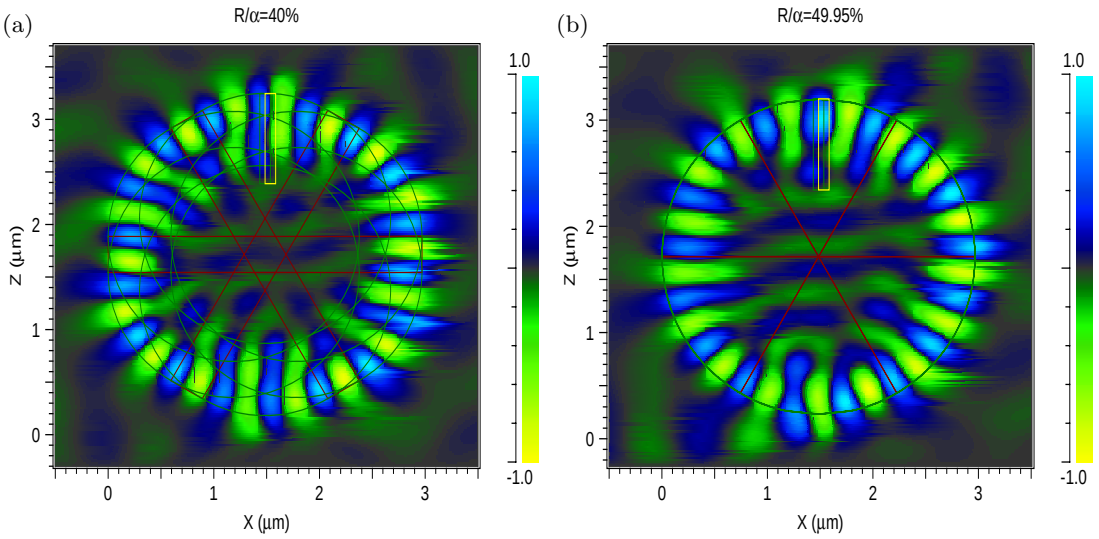

Figure 5.17: Cavity modes for hexagon microcavity with different rounding $\alpha = 2.97\mu m$

in large optical losses and that rounding these corners reduces these undesirable losses. However more corner-rounding also migrates the propagating mode from a six-bounce mode geometry to WGM, thus to maintain the six bounce mode propagation the rounding can only be done until $R/\alpha = 20$

5.7 Conclusion

A general operational principle of optical microcavities was discussed, in which a detailed theory governing the operational modes of a polygonal microcavity was also reviewed. Rounding the corners of the microcavity was shown, numerically, to reduce the cavity optical losses hence increasing the Q factor of the cavity. It was also shown in this chapter that rounding the corners also introduces a decrease in the FSR owing to the multimoded nature of the rounded cavity.

Chapter 6

Nonlinear Optical Hexagonal Microcavities

6.1 Introduction

Nonlinear processes such as SHG have a quadratic dependence on the intensity of the fundamental wave (FW) (I_ω), the total length of interaction during propagation (l) and the nonlinear coefficient $\chi^{(2)}$ (i.e $I_{2\omega} \propto (I_\omega l \chi^{(2)})^2 \ \mathrm{sinc}^2(\frac{1}{2}\Delta k l)$). Therefore, within a medium with high $\chi^{(2)}$, such as $LiNbO_3$ as an example, increasing I_ω and/or l can lead to higher $I_{2\omega}$ when phase matching is achieved (i.e $\Delta k = 0$).

On the other hand, microcavities have attracted much attention due to their small size and high Q-factor, leading to high intensity of the resonating wave with a long cavity lifetime. Such a long cavity lifetime is equivalent to a longer propagation length achievable in non-cavity devices. These micro-structures are promising for implementation in micro-optical circuits and these devices have already been demonstrated, as optical filters and signal routers for example. However, nonlinear processes within microcavities are not yet popular due to the constraints imposed by the required physical mechanisms for effective nonlinear optical processes, such as phase matching. The use of a microcavity for a nonlinear process is a very attractive area, due to the potential enhancement of these processes due to the cavity resonance [109, 110].

The efficiency (η) to convert the FW to the second harmonic wave (SH) in a dispersive medium where $n_{2\omega} \neq n_\omega$ is limited by the inherent phase mismatch, $k_{2\omega} \neq 2k_\omega$, between the FW and SH. Perfect phase matching (PPM), temperature tuning and quasi phase matching (QPM) techniques have been used succesfully to resolve this phase matching

problem [10, 4].

Another technique used to achieve the phase matching between the two waves is via a total internal reflection-quasi phase matching process (TIR-QPM), which uses the induced Fresnel phase shift between the FW and the generated SH upon total internal reflection to balance the dispersion phase shift [10, 11, 5]. TIR-QPM has an inherent advantage as it does not require an inverted domain structure along the propagation length, as is required for QPM, and can be used throughout the transparent window of the material unlike the case of PPM. TIR-QPM can also be used in microcavities, where light is resonantly guided via TIR. When the light is resonantly guided, TIR-QPM can be as efficient as the perfect phase method.

Various approaches for enhancing nonlinear processes via the use of microstructure have been proposed and demonstrated in the past. Schiller and Byer demonstrated simultaneously SHG and parametric oscillation enhancement in a monolithic TIR resonator (MOTIRR) made of bulk MgO:$LiNbO_3$ [111]. The MOTIRR consisted of a heated $11.5mm$ square bulk crystal with one face polished for input/output coupling via prism coupling. Phase matching in their MOTIRR was achieved by Type-I phase matching with a p-polarized FF wave and a s-polarized SH wave, and tuned by varying the temperature of the cavity [111]. Xu *et. al.* had used the tight-binding approximation and the FDTD simulation to analyze two types of coupled-resonator optical waveguides (CROW), namely a coupled-microdisk waveguide and a waveguide composed of coupled defect cavities in a two-dimensional photonic crystal (PC), to demonstrate the enhancement of the SHG efficiency [112]. In PC, it has been shown that enhancement of the SH field can be achieved at the band edge of the photonic crystal where the group velocity goes to zero [113]. On the other hand, defect cavities have been shown to enhance the SHG efficiency by large optical field amplitude of the local defect-cavity mode

Recently, Dumeige and Feron proposed the use of microdisk cavities and their associated WGMs to simultaneously obtain phase matching for III-V semiconductors [114]. They show a strong dependence of the SHG efficiency and cavity Q-factor on the coupling gap separating the disk resonator and the waveguide. At the optimum coupling gap, they predicted a $Q_{2\omega} = 28000$ and $Q_{\omega} = 8700$ for an $Al_{0.28}Ga_{0.72}As$ resonator waveguide and bus waveguide both on a AlAs/GaAs substrate [114].

In this chapter, we propose the generation of a SH, in a hexagonal microcavity made from single crystal lithium niobate, via TIR-QPM [24]. The TIR-QPM process, allows QPM to occur along the propagation length by balancing the dispersion phase shift

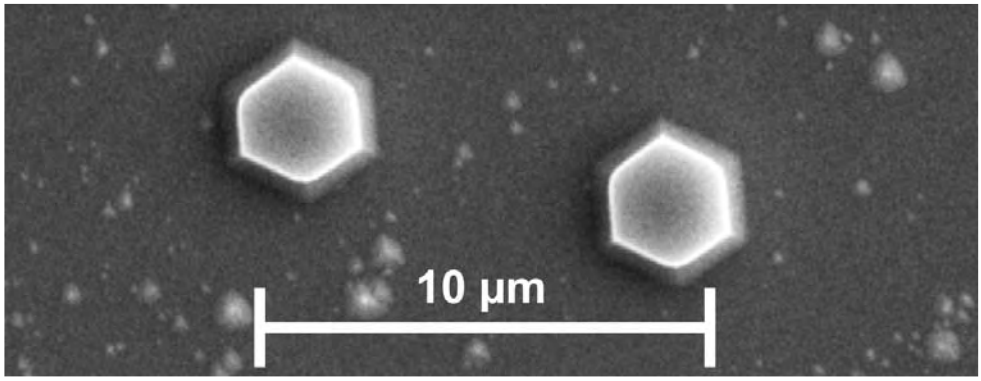

Figure 6.1: Hexagonal superstructure achieved by etching poled z-cut, $LiNbO_3$. The $-z$ face etches away while the $+z$ face remains unetched when the crystal is immersed in an $HF:HNO_3$ acid mixture [3]

with the relative Fresnel phase shift between the FW and SH induced when the two signals undergo TIR at the interface [5]. In the conventional 1^{st} order QPM process, the dispersion phase shift is cancelled after every coherence $l_c = \pi/\Delta k = \frac{\lambda}{4(n_{2\omega}-2n_{\omega})}$, for example, by reversing the sign of the nonlinear coefficient [10].

The choice of the hexagonal geometry is due to the fact that hexagonal optical cavities of superior optical quality can be fabricated by differential etching of inverted ferroelectric domains in lithium niobate, as shown by figure 6.1 [3]. In figure 6.1, the straight segments forming the perimeter of the hexagon are along the y-axes of the crystal. This superstructure is typically achieved as follows: a clean 500 μm thick optically polished z-cut wafer is coated with about 1 μm of Shipley 1813 photoresist, photolithographycally patterned with hexagon features and then developed. The patterned region is then poled to produce antiparallel domains by applying an electric field which exceeds the coercive field (22 $kVmm^{-1}$). The poled sample is then etched in 48% HF acid at about 60^oC. At this temperature the reported etch rate is 80 μm in 15 hours [3].

For TIR-QPM, full control of the orientation of the crystal's axes is crucial as this technique depends on the direction of these axes relative to the plane of incidence.

In the next section, the theory governing TIR-QPM will be discussed and compared with those of the perfect-phase matching and QPM method. In the same section the model for TIR-QPM in a hexagonal cavity will be introduce in which the results from the previous chapter are used in formulating the model. Then, we show and discuss simulation results from the TIR-QPM model.

6.2 Theory

6.2.1 TIR-QPM

The intensity of the generated SH ($I_{2\omega}$), assuming no depletion of the FW, can be written as (see [5])

$$I_{2\omega} = \frac{8\pi^2 d_{eff}^2}{n_\omega^2 n_{2\omega} \lambda^2 \epsilon_0 c} I_w^2(l)^2 \left[\frac{\sin(\Delta k l_1/2)}{\Delta k l_1/2}\right]^2 \tag{6.1}$$

here I_ω is the intensity of the FW, λ_ω is the wavelength of the FW and l is the interaction length between the FW and the generated SH. When l is of the order or longer than l_c, the amplitude of the SH, given by equation 6.1, is modulated between zero and its maximum value at every even and odd number of l_c, respectively, for the NPM case. This is shown by NPM in figure 6.2 [16]. This is because of the difference in phase velocity between the SH and the FW waves which results in destructive interference of the generated SH at every even multiple of l_c [10].

In birefringent materials, this phase mismatch is addressed by launching a polarized FW beam(s) (see below), with an incident angle equaling the phase matching angle (θ^m) at which, $n_{2\omega}(\theta^m) = n_\omega(\theta^m)$ leading to $\Delta k = 0$ and then generating SH signal orthogonally polarized to one of the two possible FW beams [115]. Phase matching in this way is termed perfect phase matching (PPM) and the corresponding $I_{2\omega}$ is shown in figure 6.2. There are two types of PPM possible for SHG: Type I PPM is when both beams of the FW have the same polarization or Type II when both beams of the FW have orthogonal polarization. For a negative uniaxial crystal such as $LiNbO_3$ the following sets of polarization are possible (see ref [116]):

Type	FW_1	FW_2	SHG
I	o ray	o ray	e ray
II	o ray	e ray	e ray

However, the PPM method suffers from the transverse walk-off of the SH pointing vector away from that of the input polarized FW if the phase matching angle is not normal to the optical axis, and this then degrades the conversion efficiency. Also, the phase matching angle requirement cannot be routinely satisfied for all nonlinear interactions and hence it is not possible to access all nonlinear coefficients throughout the whole transparent window of a nonlinear material. However, for the case where the transverse walk-off is resolved, the PPM technique is the most effective method for achieving high efficiency because it allows for perfect SHG throughout the whole crystal, as shown in

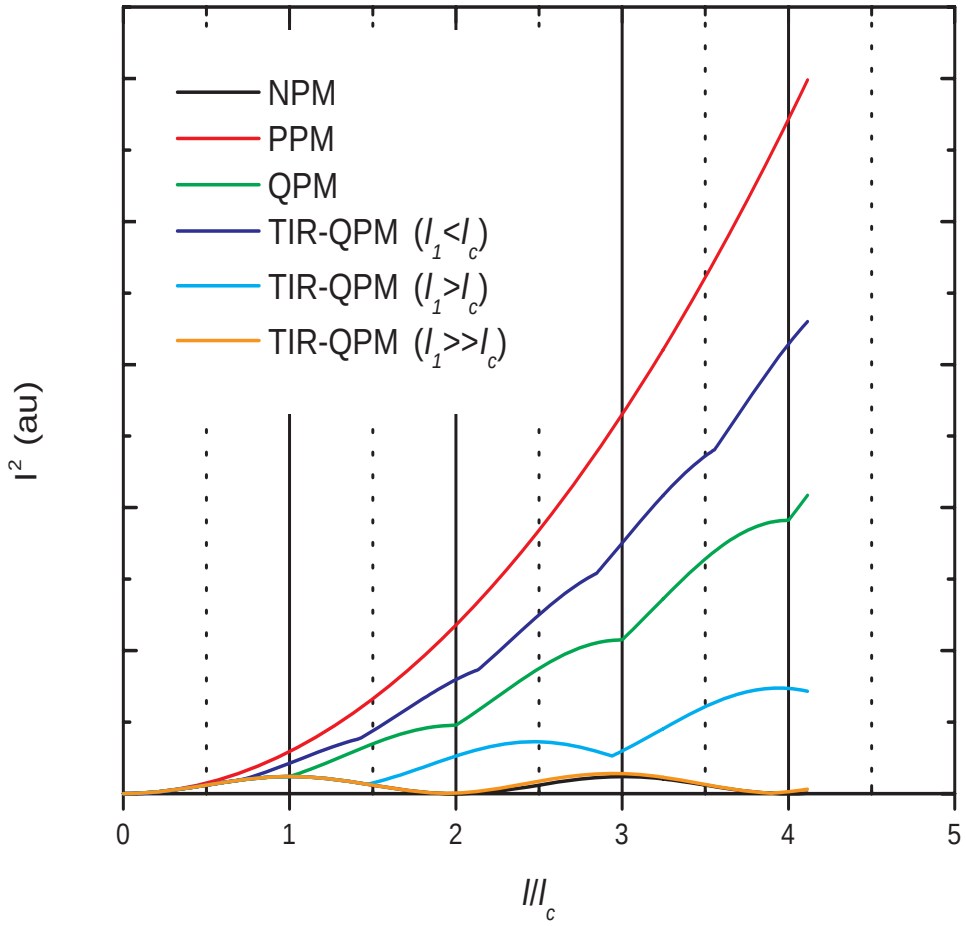

Figure 6.2: Growth of the SH along the propagation length within a nonlinear crystal. PPM: perfect phase matching in a single domain crystal. $I2\omega$ in this figure is normalized to that of PPM. QPM: first-order QPM in a periodically poled crystal and NPM: non-phase-matched interaction see ref [4]. TIR-QPM: total internal reflection-QPM see text and ref [5, 6]. For TIR-QPM, the overall phase matching occurs not necessarily at at l_c but at a length (l_1) where the Fresnel phase shift balances the dispersion phase shift

figure 6.2.

QPM is a technique commonly used to enhance the efficiency of nonlinear interactions, such as SHG, in cases where PPM cannot be applied [4]. One example of QPM is by periodic poling in $LiNbO_3$ or KTP where the sign of the relevant nonlinear second-order coefficient, $d_{ijk} = \frac{1}{2}\chi^{(2)}_{ijk}$, is inverted after each length l_c (for the case of first order QPM as shown in figure 6.2) to compensate for the phase shift between the FW and the SH (see ref [4]). The inversion of d_{ijk} at every l_c, *prevents* the down conversion of SH into FW at every odd number of l_c and enables the growth of SH, as shown in figure 6.2.

The QPM technique has several advantages over the PPM technique however. For QPM, the whole window of optical transparency of a nonlinear material can be used for effective nonlinear interaction provided that the desired QPM period (Λ) can be achieved. This is in contrast to PPM where the walk-off condition can only be minimized at certain frequencies. Also, QPM allows the use of the largest nonlinear coefficient of $\chi^{(2)}$ which for $LiNbO_3$ is $\chi^{(2)}_{zzz}$, as an example, since the input incindent angle of the FW is not limited to θ^m. For a given l, the SHG effecincy of PPM is $\frac{4}{\pi^2}$.

However, in the QPM process, $\Lambda \propto \lambda$ where Λ is the period of the inverted domain pattern, which implies the requirement of short periods for low values of wavelength which are not always possible to fabricate via conventional methods.

Another way to achieve QPM is by utilizing the relative Fresnel phase shift ($\Delta\Phi_F$) given in equation (6.2) between the FW and the induced SH, that occurs upon TIR of the two waves at a cavity-surrounding interface after propagating for a length l_1, to compensate for the dispersion phase mismatch ($\Delta k \cdot l_1$) [10, 5]. In this method, referred to as "TIR-QPM", both the FW and the induced SH are made to reflect via TIR on a surface as shown in figure 6.3 for the case of propagation in a parallel sided plate. In doing so they experience a relative phase difference that can cancel that due to dispersion.

The relative Fresnel phase shift is given as

$$\Delta\Phi_F = \Phi_\gamma(2\omega) - 2\Phi_\gamma(\omega) \tag{6.2}$$

where $\Phi_\gamma(2\omega)$ and $\Phi_\gamma(\omega)$) are the Fresnel phase shifts of the SH and FW, respectively, which occurs after each TIR. γ is either p or s as shown in equation (6.11 − 6.12) depending on the polarization of both FW and SH. The effective nonlinear coefficient (d_{eff}) can also change sign following reflection depending on the input/output polarizations of both FW and SH relative to the crystal symmetry, denoted by the azimuthally angle (φ in figure 3.1b). The possible change of sign of (d_{eff}) results in an extra phase shift ($\xi\pi$),

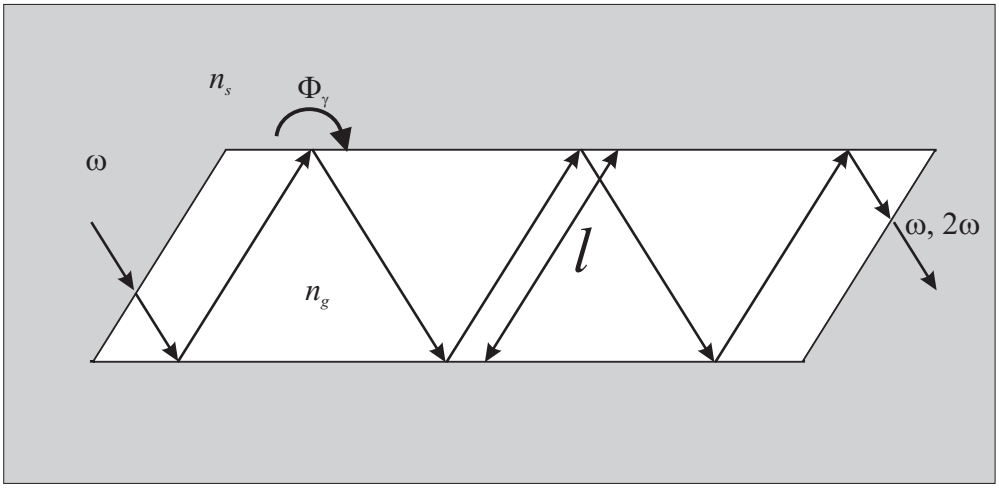

Figure 6.3: Schematic diagram demonstrating the TIR-QPM technique within a parallel plate device

with ξ being either 1 or 0, respectively. For values of θ above θ_c, $\Delta\Phi_F$ can take any value from 0 and 2π, as θ increases towards 90^o. Thus, the combination of $\Delta\Phi_F$ and $\xi\pi$ can, in general, compensate for any dispersion phase shifts and allows for a more flexible choice of the propagation length, between adjacent reflections, as compared to the periodic poling case where the $2l_c$ period constraint is strict. The global phase shift ϕ, between the FW and SH during TIR, is therefore the combination of all these phase shifts and is given in equation (6.3) [5].

$$\phi = \Delta k l_1 + \Delta\Phi_F + \xi\pi = 2\pi m,\ m = 0, 1, 2, \ldots \tag{6.3}$$

For a given ω, θ and set input/output polarization state of the waves, the condition in equation (6.3) is only possible at certain values of l_1. The intensity of the generated SH ($I_{2\omega}$), for no reflectivity loss, can be written as [11]

$$I_{2\omega} = \frac{8\pi^2 d_{eff}^2}{n_\omega^2 n_{2\omega}\lambda^2\epsilon_0 c} I_w^2 (N l_1)^2 \left[\frac{\sin(\Delta k l_1/2)}{\Delta k l_1/2}\right]^2 \left[\frac{\sin(N\phi/2)}{N\sin(\phi/2)}\right]^2 \tag{6.4}$$

where I_ω is the intensity of the FW and λ_ω is the wavelength of the FW. In equation(6.4), the first trigonometric part represents a parametric conversion on each path, l_1, traveled by the mode between two bounces, while the second trigonometric part represents the interaction of all input and generated fields after each reflection. For the case when l_1 is exactly an odd number of l_c, the combination of $\Delta\Phi_F$ and $\xi\pi$ has to sum up to π for QPM to occur, in which case both trigonometric functions in equation (6.4) are maximized [5]. This case is termed resonant TIR-QPM and is found

to be practically more efficient as compared to the non-resonant case, l_1 can take any value but not even multiple orders of the l_c, while satisfying equation (6.3). Though the resonant TIR-QPM is more effective than the non-resonant case, it is also more restrictive due to the requirement that the length between the reflections has to be exactly an odd multiple of the coherence length. This requirement is, practically, very difficult, to achieve for example in planar devices where the length in between each reflection is controlled by the angle of incidence at the input face of the device [5]. Figure 6.2 compares the efficiency of the PPM, QPM and TIR-QPM methods. In this work we focus on the non-resonant case and we will use TIR-QPM to refer to this case from now on, whereby the resonant case is generalized as a special form of the non-resonant case.

The other advantage of TIR-QPM is that l_1 can take up any values but not limited to the integral multiple of l_c. For the case where $l_c > l_1$ the efficiency of the TIR-QPM is ideally comparable to that of the higher order QPM process while for $l_c < l_1$ the efficiency approaches that of PPM as shown in figure 6.2 [6]. For large values of l_1 relative to the l_c, the TIR-QPM efficiency drops to that of NPM. The limitation to this ideality is mostly due to the reflection losses that occur at each reflection. In figure 6.2, three values of $l_1 = 1.72, 7.35, 12.71\mu m$ were used and the reflection coefficients were set to be 100%.

I_ω in 6.1 is defined at the input and it stays at that value throughout l, so the value $I_{2\omega}$ increased mainly do to l. Within a singly-microcavity where FW resonates, I_ω increases after each round trip until the steady state condition is met. Basically, I_ω is amplified until steady state. Therefore, $I_{2\omega}$, increase not only due to increment of l but also due to the amplification of I_ω. In a doubly-resonant microcavity where SH also resonate, $I_{2\omega}$ is further amplified.

Since the idea is to use the stored and cavity-enhanced FW (by the cavity) to increase the efficiency of the SHG, equation (6.10) has to be solved simultaneously for FW and SH, together with equation (6.3), for an ideal cavity size α_s. Such a cavity, with $\alpha = \alpha_s$, will allow resonance of both the SH and the FW via TIR and will also allow TIR-QPM to occur. To achieve an ideal cavity size for this doubly resonant situation, we follow the approach by Haidar [6] used for determining the ideal thickness for the case of TIR-QPM in a semiconductor plate, as shown in the next subsection.

6.2.2 The Model of TIR-QPM in a hexagonal cavity

First, we consider the requirement for the FW to resonate in a hexagonal microcavity, as given by equation (6.10). The angle of incidence within this cavity is set at 60^o and is

fixed at this value for the entire model. Our model is based on a $LiNbO_3$ crystal as a bulk platform and, since this crystal is both uniaxial and dispersive, we have to pay attention to the polarization of the FW and use the corresponding refractive index.

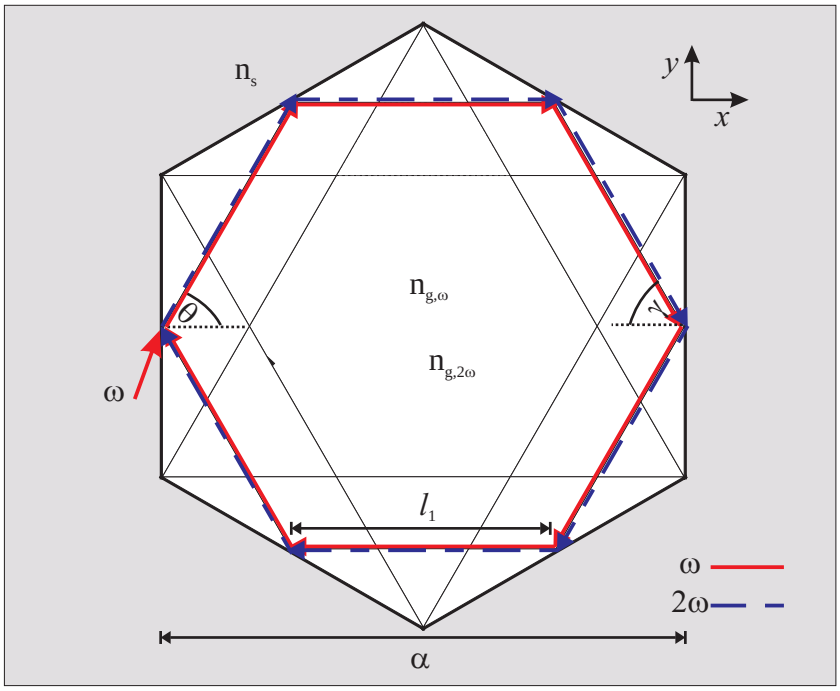

Figure 6.4: Hexagonal cavity showing schematic resonance propagation of both the FW and SH. $n_{g,\omega}$ and $n_{g,2\omega}$ are the refractive indices of the material experienced by FW and SH respectively

For the reasons which will be apparent very shortly, the plane of polarization of the FW will be set at s-polarization. For example in figure 6.4 the plane of incidence is parallel to the page and hence, for the s-polarization, make the electric field components of the beam normal to the plane of the page. The s-polarized FW will see the extraordinary refractive index (n_e^ω). The corresponding Fresnel phase matching is then Φ_s^ω, given by equation (6.12). For dispersion calculation, the Sellmeier equations introduced in section 2.4.6, were used to determine the corresponding indices of refraction. As far as the resonance of the FW is concerned, what remains is to find the correct cavity size $\alpha^\omega = \frac{L(60^o)}{3}$ at the given wavelength, such that the LHS of equation (6.10) equals an integer multiple of 2π ($\phi_R = 2\pi m$). Since $\cos(m\pi) = \pm 1$, for integer values of m, the resonance condition in equation (6.10) for FW can be rewritten as

$$f_\omega = \cos(\frac{1}{2}\phi_R^\omega) = \cos(\frac{1}{2}[k_o n_e^\omega L(\alpha^\omega) + 6\Phi_s^\omega]) = \cos(m^\omega \pi) = \pm 1 \tag{6.5}$$

.

Likewise, the resonance condition for the SH can be written as

$$f_{2\omega} = \cos(\frac{1}{2}\phi_R^{2\omega}) = \cos(\frac{1}{2}[k_o n_e^{2\omega} L(\alpha^{2\omega}) + 6\Phi_s^{2\omega}]) = \cos(m^{2\omega}\pi) = \pm 1 \tag{6.6}$$

.

where $\alpha^{2\omega}$ is the resonating cavity size for SH. For a doubly resonating cavity size for both the FW and the SH, equations (6.5-6.6) must be satisfied simultaneously, in which case $\alpha^{\omega} = \alpha^{2\omega}$. Also for the TIR-QPM process, the global phase shift in equation (6.3) can be written as

$$f_{\phi} = \cos(\frac{1}{2}[\Delta k l_1(\alpha^{\phi}) + \Delta\Phi_F + \xi\pi]) = \cos(\pi m^{\phi}) = \pm 1 \tag{6.7}$$

where α^{ϕ} is the cavity size at which the dispersion phase shift will be balanced by the Fresnel phase shift. The ideal cavity size is $\alpha^m = \alpha^{\omega} = \alpha^{2\omega} = \alpha^{\phi}$. Within the ideal cavity, all the functions in equations (6.5-6.7) have values of ± 1 and so will be their products. Equation (6.8) shows the resulting products of the above three equations.

$$f = f_{\omega}(\alpha^m) \times f_{2\omega}(\alpha^m) \times f_{\phi}(\alpha^m) = \pm 1 \tag{6.8}$$

Figure 6.5 shows the variation of the functions $f_{\omega}, f_{2\omega}, f_{\phi}$ and f in equations (6.5-6.8) for the s-polarized FW and SH in z-cut $LiNbO_3$ at $\lambda = 0.959\mu m$. Each of these functions has a maximum values of ± 1, at which resonance of the corresponding wave is achieved. For example at $\alpha = 2.907\mu m$, $f_{2\omega} = -1$ while $f_{\omega} \approx 0.1$ which means SH will resonate in the cavity of this size while FW will not.

In calculating equations (6.5-6.8) an s-polarization was selected so to make it possible for use of largest of the nonlinear coefficients (d_{33}) of the $z-$ cut $LiNbO_3$ to be used for generation of SH. This implies that Fresnel phase given equation (5.12) was used instead of that equation (5.11). The two equations will results with different (α^i) and hence with different (α^m), thus the ideal cavity for s-polarized mode will not be ideal for p-polarized mode.

Figure 6.5 displays six values of $\alpha^{2\omega}$ shown by ± 1 values of the blue dash curve, three values of $\alpha^{2\omega}$ shown by ± 1 values of the red long-dash curve, and a single value of α^{ϕ} shown by a black arrow. From figure 6.5, $\alpha^m = 2.98\mu m$, since it is at this value that $\alpha^{2\omega} = \alpha^{\omega} = \alpha^{\phi}$.

Figure 6.6 shows a broad variation of f and $f_{\phi}(\alpha^m)$ against the cavity size, which shows the locations of other smallest possible α^m at $\alpha_1^m = 2.98\mu m$, $\alpha_2^m = 12.73\mu m$, and

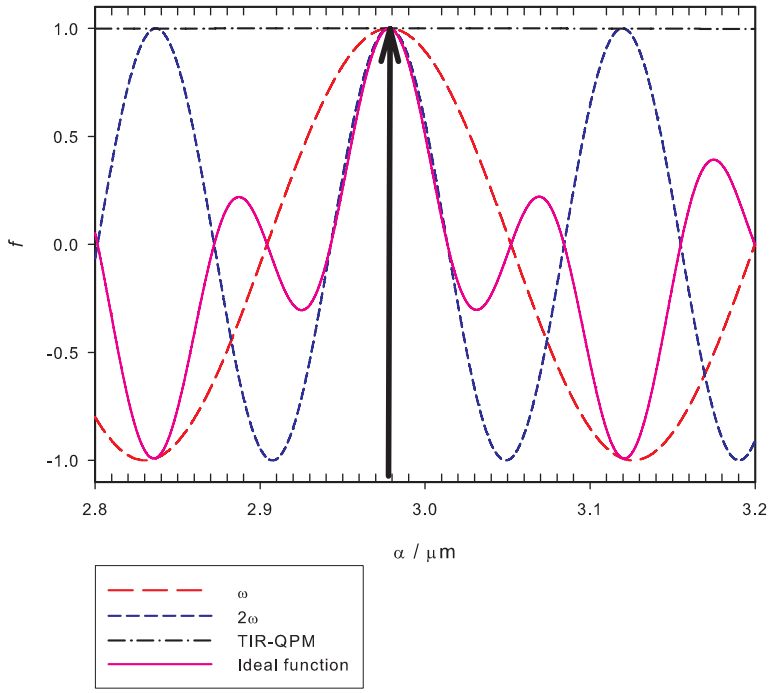

Figure 6.5: Plot showing the dependence of the cavity resonances of the FW, SH, TIR-QPM condition and the ideal condition on the cavity dimension α. The ideal cavity size is therefore at $\alpha^m = 2.98\mu m$ for $\lambda = 0.959\mu m$

$\alpha_3^m = 22.35\mu m$, for $\lambda = 0.959\mu m$. These three ideal cavity sizes will have different values of l_1 and hence different SH efficiency, as shown in figure 6.2 where the smaller the value of l_1 corresponds to the high SH yield.

The value of α^m is determined from the constraints formulated above and will be used in the next section as a guide to locate the ideal cavity size from the FDTD simulation results. Also, the cavity characteristics, i.e repetition of the solution of the FW in figure 6.5, will be used as a benchmark to validate the FDTD solutions.

6.3 Simulation Results

We have used our FDTD simulation to study the response of an ideal hexagonal microcavity for both the FW and the SH. The focus is firstly on the individual propagation of the FW and SH within the microcavity. The SH here does not refer to the second harmonic signal generated by the FW, but simply a mode launched at half the wavelength of the FW. The evolution of this mode within the microcavity will have similar properties to the

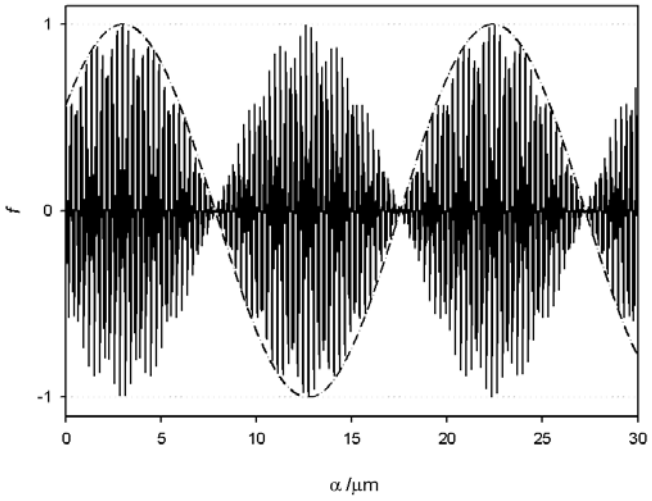

Figure 6.6: Plot showing the dependence of the global phase shift on the cavity size. Three ideal cavity sizes are shown at $\alpha_1^m = 2.98\ \mu m$, $\alpha_2^m = 12.73\ \mu m$, and $\alpha_3^m = 22.35\ \mu m$ i.e, all the solutions in figure 6.5 belong to the first lobe in this figure while the other lobes show the location of the other ideal cavity sizes. The dashed line represents the global phase shift.

SH generated by FW. Thereafter we make use of the cavity response from both FW and SH to estimate the SHG efficiency of the cavity, when the FW is converted into the SH via equation 6.4.

The refractive index of the cavity at FW and SH corresponds to the extraordinary refractive index of congruent $LiNbO_3$, as given by the Sellmeier equations described in chapter 2 for λ and $\frac{\lambda}{2}$ respectively. The polarization of the launched mode was set to TE (E-field is perpendicular to the cavity plane).

6.3.1 Determination of the ideal cavity size using FDTD simulation

With the FDTD simulation, we seek a value of α^m for which both FW and SH will resonate. In the previous chapter, we mentioned the dependence of the cavity response on the grid size and we have used a rule of thumb that grid size$= \frac{\lambda}{nC}$, where C is a constant determined to give a convergence value of α^m for a given λ. Within the convergence range for both FW and SH simulation, the values of α^m approach their true value. This procedure was used to determine $\alpha^m \approx 2.98\ \mu m$ in figure 6.7 from the TIR-QPM model.

For a given λ, long-lived cavity modes have similar properties. Hence, a full study of

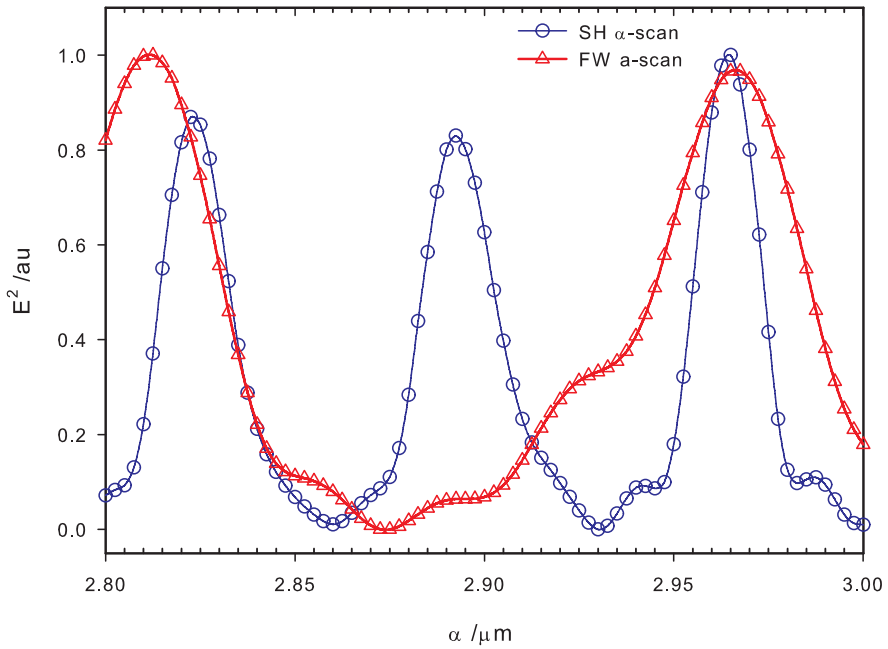

Figure 6.7: FDTD simulation α scan results for $\lambda^{\omega} = 0.959\mu m$ and for $\lambda^{2\omega} = \frac{\lambda^{\omega}}{2}$. $\alpha_1^m = 2.98\mu m$ because it is at this value that $\alpha^{2\omega} \approx \alpha^{2\omega}$.

the cavity at the FW and SH can be achieved by long- lived cavity modes of the individual cases. If, in our simulation, the FW was generating the SH in situ, then all the studies from now on should be done in that ideal cavity size. Here, the SH is estimated based on the FW power amplification and on the Q-factor of both the FW and SH launched individually in the cavity. Therefore, variation of the grid size, which becomes computationally expensive for large α, to obtain a well-resolved ideal cavity size, is not necessary.

Figure 6.7 shows the scan of the FW (SH) for $\lambda^{\omega} = 959nm$ ($\lambda^{2\omega} = \frac{\lambda^{\omega}}{2}$). The refractive indices of the FW and the SH were set to $n_e^{\omega} = 2.1627$ and $n_e^{2\omega} = 2.2632$, respectively. From the above defined TIR-QPM model it was shown that an ideal cavity size can be located for $f(\alpha^m) = \pm 1$, at a given wavelength. In figure 6.7, the ideal cavity size corresponds to the value $\alpha^m \approx 2.98\mu m$ where $f_{\omega} \times f_{2\omega} \approx 1$. Based on the results of the TIR-QPM model in figure 6.5 about a broad range for which $f_{\phi} = 1$, i.e $f_{\phi} = 1$ for for all six values of $\alpha^{2\omega}$ and three values of α^{ω}, the phase matching condition is assumed to cover a broad range also in figure 6.7.

The location of the ideal cavity size from the FDTD simulation in figure 6.7 is justified

by comparing this figure with figure 6.5 that was obtained from the TIR-QPM model. From figure 6.5, the period of the FW resonating cavity size, denoted by the separation between the adjacent $f_\omega = \pm 1$, is about $\alpha^\omega_{i+1} - \alpha^\omega_i$ =140 nm, which is similar to the separation of the FW modes in figure 6.7. The same is true for the SH, where the period is about half that of the FW. This direct comparison between the FDTD simulation of the α scan results and the TIR-QPM model results validates our theory in terms of the six-bounce propagation trajectory in a hexagonal microcavity.

6.3.2 Steady-state Cavity Response

In order to obtain the cavity response on resonance, the steady-state simulations were performed at the resonance wavelength. This was achieved by launching the fundamental mode and measuring the cavity response as a function of time until the cavity response reached the steady state, at which point the cavity loss per round trip and the cavity amplification per round trip are equal.

A moderate cavity (not too small and not that big either), was used to minimize the cavity losses due to the sharp corners and also to minimizes the large computational time required by a large cavity size. Also, from figure 6.6, three ideal cavity sizes were shown:$\alpha^m_1 = 2.98\ \mu m$, $\alpha^m_2 = 12.73\ \mu m$, and $\alpha^m_3 = 22.35\ \mu m$. The equivalent l_1 values of these three cavity sizes were used in figure 6.2, it was shown that for a value of l_1 equivalent to α^m_3 the SH yield was comparable to that of the NPM method. Therefore, a moderate cavity size for $\lambda = 959$ nm, corresponds to α^m_2 in figure 6.6. Though it was shown in figure 6.2 that for $l_1 < l_c$, this is practically difficult to achieve as the cavity losses increases with the reduction of the cavity size.

For $\lambda = 955$ nm, the corresponding suitable ideal cavity size is found to be $\alpha^m_2 = 13.95$ μm which is equivalent to the second solution for $\lambda = 959\mu m$ in figure 6.6. Here, the value of α^m_2 is for $\lambda = 955\mu m$ instead of $\lambda = 959\mu m$ due to the fact that $f_m(955)$ was closer to a unity value than $f_m(959)$.

Figure 6.8 shows the cavity build-up for λ and $\lambda = \frac{\lambda}{2}$ for a perfect hexagonal cavity. For this ideal cavity size, the cavity has a higher Q for $\lambda/2$ than for λ, as shown by maximum number of round trips (N^{max}) before steady-state. For example, the FW reaches the steady state after only 13 round trips, i.e $N^{max}_{FW} = 13$ while $N^{max}_{SH} = 33$. Figure 6.9 shows an exponential growth curve fitted to the cavity power profile of FW in figure 6.8 and the following power profile was determined with the variation of the round trips.

$$P_\omega(N) = P^{max}_\omega(1 - exp(-bN)), \tag{6.9}$$

where P_{ω}^{max} is the maximum amplified power of the FW and $b = 0.330$ represent the cavity loss per round trip. The implication of equation (6.9) for the hexagonal cavity modeled in figure 6.8 is that the FW amplification follows this equation. However, if the right, appropriate FW is coupled from the bus waveguide to excite the ideal cavity mode ($\theta = 60^o$) , P_{ω}^{max} will be lower than that when the mode is launched from within the cavity but the number of round trips before steady state will still be the same.

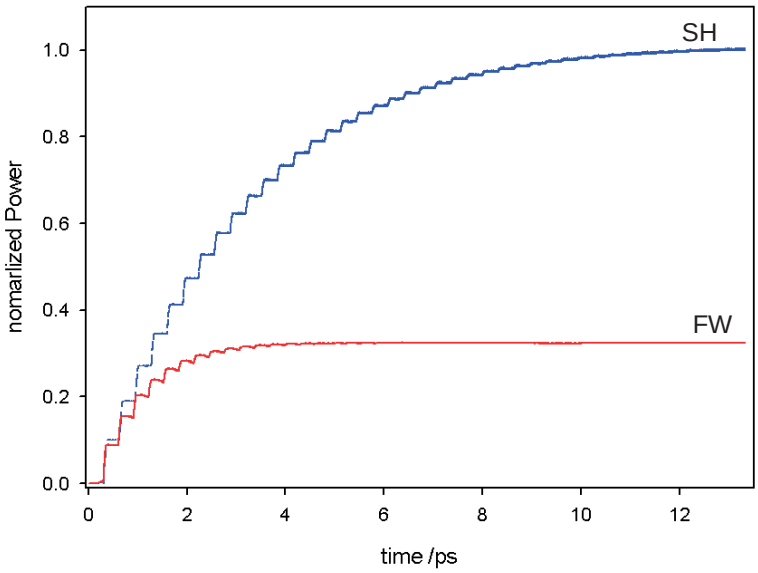

Figure 6.8: The cavity response for both FW and SH at a moderate ideal cavity size of $\alpha_2^m = 13.95$ μm. The power output is normalized to that of SH at steady state

We use the values in figure 6.8 for N^{max} and amplification values for FW given by equation 6.9 and estimate the SHG output from the cavity in the next section.

6.3.3 SHG efficiency via TIR-QPM in a hexagonal cavity

Due to the complexity of our TIR-QPM set-up and the time constraints that we had, we did not use the FDTD simulation engine to estimate the SH conversion yield with the cavity. Instead, we use the TIR-QPM model, together with values obtained from the simulation to estimate the SHG efficiency. We assume that the ideal cavity size obtained from the FDTD simulation has equivalent properties to those obtained from the model above. Our assumption has been justified above by comparing the cavity size, the scan obtained from the FDTD simulation, and that obtained by using the six-bounce wavefront matched trajectories. To summaries these comparisons: It was found that the separation between the -1 and +1 solution in the TIR model is similar to the separation

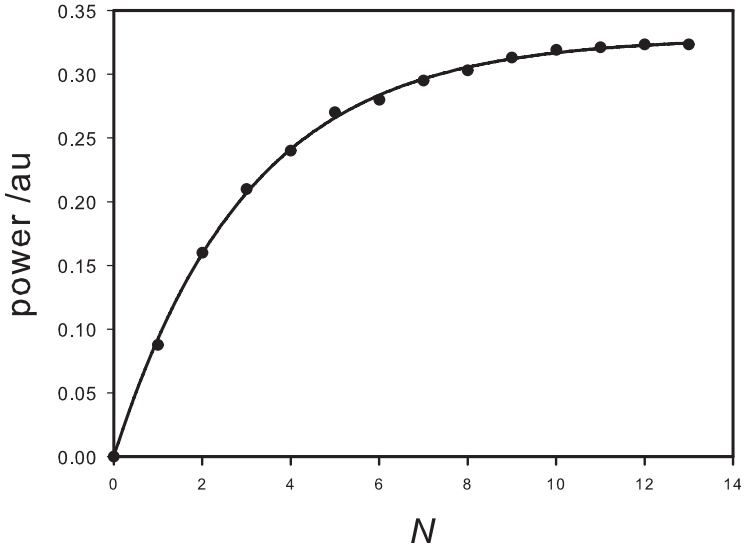

Figure 6.9: A curve fitting to the power profile for the FW within a hexagonal microcavity to determine the cavity loss per round trip for an deal cavity size of $\alpha_2^m = 13.95$ μm $b = 0.33$.

between the resonating cavity size from the FDTD simulation, for both the SH and FW.

With this assumption we can then use the cavity Q factor and the number of round trips for both FW and SH together with the value of the power for each of the FW round trips up until the steady state obtained from the FDTD simulation to estimate the SH growth in the cavity.

For the SHG efficiency estimation, we will need to know the cavity Q factor for both the FW and SH and also the cavity amplification for FW. The cavity Q factor for SH, which is different from the FW, defines the maximum number of the SH round trips (N_{SH}^{max}). We will assume that, when the FW has reached the steady state (N_{FW}^{max}), there will be no more SH build-up within the cavity once the N_{SH}^{max} is reached. That is, the SH will grow in the cavity until its growth is balanced by its loss, at which point the SH output will be constant for the case where $Q_{FW} < Q_{SH}$.

In our case, the SH growth is due to the combination of two mechanisms: firstly, the conversion growth due to the presence of the FW over the entire length of the FW propagation with the cavity and secondly, the gain growth of the SH as it builds up within the cavity. The latter growth contribution is due to the fact that the cavity resonates

both the FW and SH. If, for example, the cavity did not resonate the SH, the only SH growth mechanism would be that due to the presence of the FW similar to the normal QPM. This individual conversion growth mechanism, must lead to high SHG efficiency per volume of the hexagon via the quadratic dependence of the SH on the resonated FW. In other words, this conversion mechanism will be the dominant one, however it will not be effective on its own as most of the SH signal will be radiated out if the latter signal is itself not resonated.

Equation (6.4) was used to estimate the SH build-up within the cavity until it reaches the steady state, determined by N_{SH}^{max}. The angle of incidence was fixed at 60^o and only the six-bounce trajectory per round trip, with equal propagation length between the bounces was considered. This is because, though these modes are wavefront matched, the SHG will not be the same when the lengths per bounce (l_1) are not the same. The longer path length between the bounces will undergo the TIR-QPM later than the shorter path ones, leading to different SHG efficiency per length.

Figure 6.10 shows the estimation of the growth of the SH in a regular hexagonal cavity, i.e with no rounding ($\frac{R}{\alpha} = 0\%$), via the use of equation (6.4) for different values of the reflection coefficient (r). In equation (6.4) I^{ω} is not a constant value up until 13 round-trips but takes the values of FW from figure 6.8 for TIR-QPM. For PPM and QPM, I^{ω} was constant and equal to the starting I^{ω} used for TIR-QPM because there is no resonance of the FW in these condition. The SH was allowed to propagate until it reached the steady state, after which no buildup is expected. After 13 round trips, the growth in SH is due mostly due to the resonance of the SH but not the conversion from FW. I^{ω} is amplified after each of the round trips by the resonance of FW within the cavity. This **amplification**, boosts the SH efficiency (via the TIR-QPM) to be more efficient than that via PPM and QPM methods. Without this amplification, TIR-QPM method will never be more efficient than the PPM method, and for our choice of the cavity size $\alpha_2^m = 13.95$, it will be less efficient as compared to the QPM method (see figure 6.2). The total length of the devices used to estimate the SH growth for PPM and QPM is $NL = 3N\alpha = 1.25mm$, about 90 time longer than the hexagonal microcavity used for TIR-QPM. The use of a resonant cavity has boosted the efficiency of the TIR-QPM method.

The effective number of bounces inside the microcavity is limited by the Goos-Hanchen shift and by the surface roughness on the side of the cavity which controls the value of r [5]. There is an effective number of round trips for a given r after which there will be no

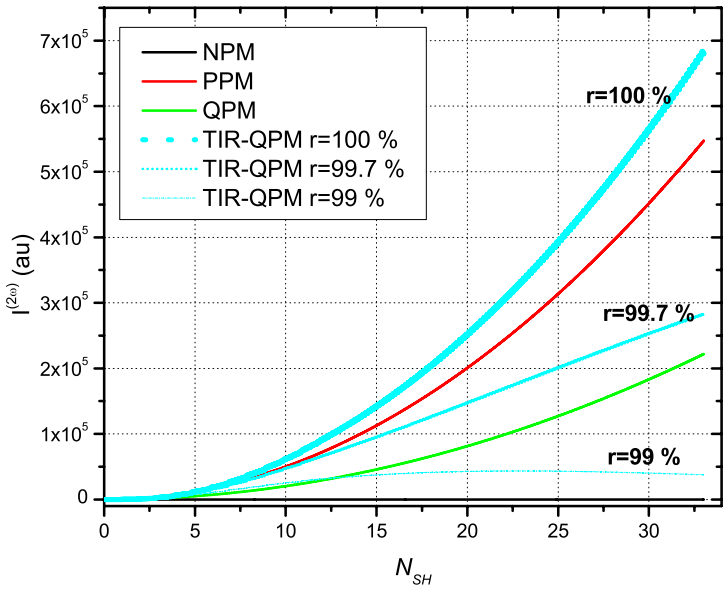

Figure 6.10: Estimated SH growth for a regular hexagon with no rounding, for $\lambda = 0.955\mu m$ with $\alpha_2^m = 13.95\ \mu\text{m}.r$ is a reflection coefficient. The total length of a linear devices used to estimate the SH growth for PPM and QPM is $3N\alpha = 1.25mm$. For $r = 100\%$, the TIR-QPM in a hexagonal cavity greater than that from PPM method for an equivalent length. For $r = 99\%$ N_{SH}^{max} is limited to about 15 round trips before the SH signal starts to degrade down toward that of NPM

signal-build-up. This effect is shown by the factor contained in the second trigonometric function of equation 6.4 as

$$\left[\frac{\sin(N\phi/2)}{N\sin(\phi/2)}\right]^2 = \frac{r^N}{N^2}\frac{1-2\sqrt{r^N}\cos(N\Delta\phi)+r^N}{1-2\sqrt{r}\cos(\Delta\phi)+r} \tag{6.10}$$

where $\Delta\phi$ is the global phase shifting given in equation 6.7 and it is zero for a TIR-QPM structure. The effect of r is shown in figure 6.10 where $I^{(2\omega)}$ drops as the reflection losses increase.

As $\frac{R}{\alpha}$ increases, the Q factor increases, leading to longer cavity lifetime for both the FW and the SH and hence the SH efficiency will increase. It has been shown that increasing $\frac{R}{\alpha}$ results in the resonance wavelength being blue-shifted. This was attributed to be due to the growth of the cavity size per rounding resulting in a longer cavity path length. Hence, to keep the resonating wavelength constant, the cavity size has to be reduced per rounding for the cavity path length to remain constant. As our TIR-QPM does not see any rounding applied to the cavity within the six-bounce trajectories, we keep the wavelength and cavity size constant and use the rounding effect results.

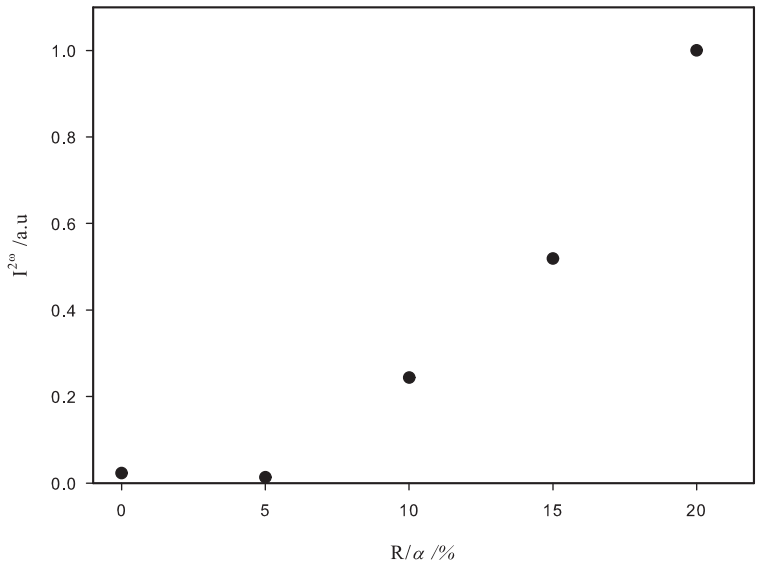

Figure 6.11: Growth of the SH with the rounding of the hexagonal corners, for $\lambda = 0.955$ μm with $\alpha = 13.95\mu m$.

Figure 6.11 shows the estimated normalized SH signal with cavity rounding. The SH increases with smoothing of the corners of the cavity owing to the increasing Q-factor at resonance. It is expected that the SH would be at its maximum in the cavity with

more smoothing of the corners. We do not show the results in which $\frac{R}{\alpha} > 20\%$ as the propagation within the cavity migrates from a six-bounce trajectory a to WG type.

So far we have only mentioned the simulation results for a cavity in which the mode is launched from within the cavity. We have not said anything about the expected detectable signal. To do that we will need to estimate the coupling efficiency of the mode from the bus guide into the cavity, which was beyond the scope of this study. A measurement of the coupling efficiency of hexagonal microcavity can be found in ref [94]. They have measured a Q-factor of about 1300 for a hexagonal microcavity with $\alpha = 50\mu m$. For small cavities like the one simulated in our work, the losses are higher. So these studies should be extended for a bigger cavity size where the modes are also launched from outside to have a feel for the expected SH signal.

6.4 Conclusion

In this chapter, the TIR-QPM model for a hexagonal cavity was introduced. The model was based on the six-bounce trajectory introduced in chapter 5 and phase-matching of the FW and SH via the TIR-QPM technique. The FDTD simulation method was used to validate the model and also to demonstrate its capability for SHG in a hexagonal microcavity in $LiNbO_3$. The TIR-QPM method is shown to be limited mostly by the reflection losses which limits the number of round trips to an effective number of round trips and hence compromises the build-up of the SH per cavity. However, TIR-QPM is capable of a high SH efficiency, even greater than that of perfect phase matching, thanks to the resonance of both the FW and SH within the same cavity. If FW was not at resonance, higher efficiency TIR-QPM (greater than that of QPM) can be obtained by lowering the length l_1 in between the bounces to be lower than l_c. TIR-QPM is by far the most efficient compared with the non-phase-matching.

Chapter 7

Feasibility studies of a nonlinear micro-ring resonator on a Ti:indiffused $LiNbO_3$ waveguide

7.1 Introduction

In chapter 5, it was shown that microcavity structures can lead to the enhancement of nonlinear processes within their small volume if phase matching conditions between the fundamental and the harmonic waves are met. In that chapter, the TIR-QPM method was used, whereby the Fresnel phase shift was used to balance the dispersion in order to achieve phase matching within a hexagonal microcavity [24]. In this chapter, another approach is proposed to enhance nonlinear processes within a mircoring waveguide resonator via the use of periodic domain inversion.

This QPM method requires the reversal of P_s along the propagation length [10, 4]. Ilchenko *et al.*, demonstrated a periodically poled toroidal disk resonator made of $LiNbO_3$ [110]. Their device was, however, periodically poled along a specific direction, hence limiting the QPM to two specific areas of the resonator. This device requires a large Q factor in order to be efficient. In this work, we propose creating a periodic inverted domain structure along the circumference, such that the light propagating along this path length experiences a constant Λ, as shown in figure 7.1.

Due to the 3m symmetry of the $LiNbO_3$, the induced inverted domains on the $-z$ face have the hexagonal shape oriented along a specific direction. These preferential hexagon shaped domains have their walls parallel to the crystal y-axes [117].

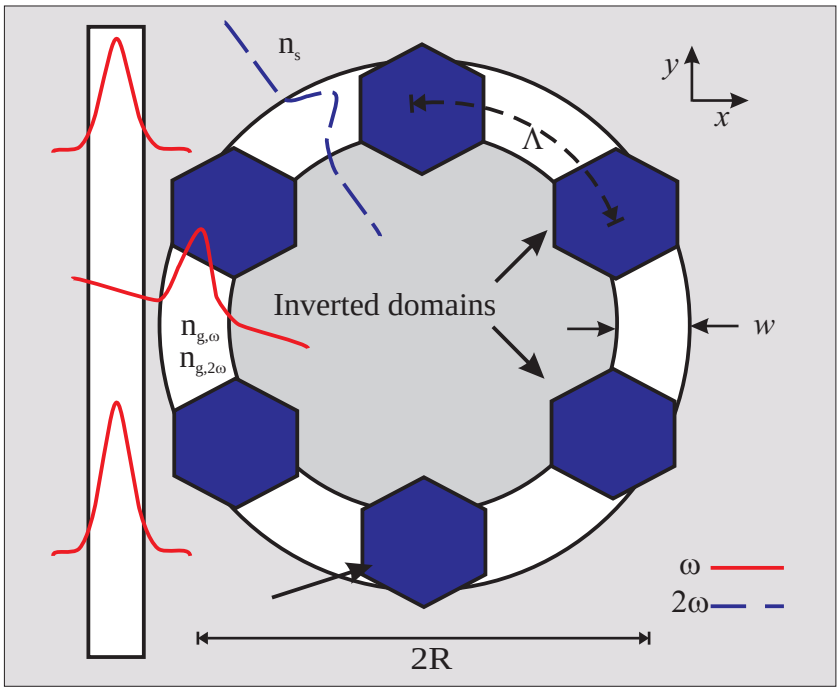

Figure 7.1: PPTi:LN ring resonator for nonlinear applications

We also propose the use of an optical ridge waveguide, instead of a bulk material, to further improve the mode confinement within the device. Three dimensional structures like *ridges, strip or channel* waveguides are normally used in order to enhance the confinement within optical devices. The choice of the type of waveguide to use is defined by the application of the final devices. For example, ridge waveguides have high index contrast and hence allow smaller cross-section dimensions and tighter bend angles with lower optical losses than the conventional channel waveguide [118]. It is for the later reason that this type of waveguide was preferred for our microring resonator devices.

The technology behind manufacturing reproducible Ti:$LiNbO_3$ is very mature and the analytical functions describing the refractive index profile of this waveguide have already been evaluated [119, 120, 32]. Ti:$LiNbO_3$ was therefore selected as a platform to demonstrate our proposed goals. From these analytical functions, the refractive index can be calculated as a function of the Ti film thickness (τ), dwell temperature (T_d) and dwell time (t_d) during the diffusion processes.

In this chapter, the fabrication steps towards achieving a microring resonator, shown in figure 7.2, and the attempt to obtain a periodically poled resonator will be discussed. The following steps, as outlined in figure 7.2, will be followed to achieve the final device:

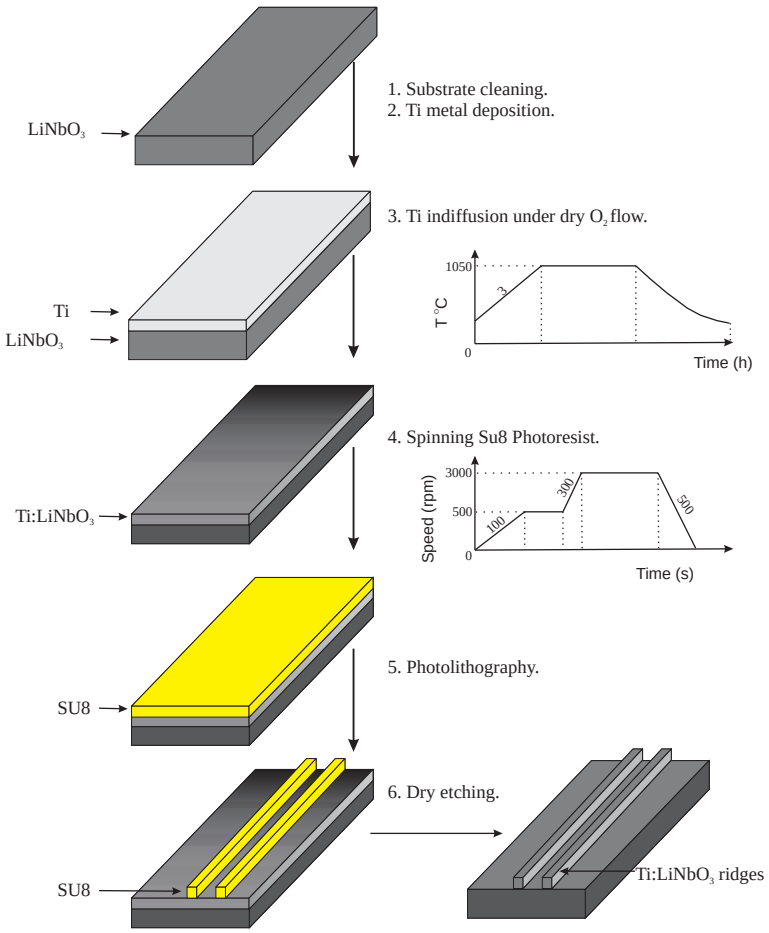

Figure 7.2: A schematic flow diagram for the production of the Ti in-diffused $LiNbO_3$ planar waveguide

Preparation of the Ti:$LiNbO_3$, poling the resulting planar waveguide along the ring cavity (not shown in the figure 7.2) , and finally the preparation of the ridge waveguide. The details of the steps will be discussed in the next sections.

Due to the lack of a clean room facility at the University of Southampton, following the fire incident in 2005, part of the fabrication work was undertaken at Glasgow University. Because of the need to work at different clean room facilities, work on the optimization of the Ti:$LiNbO_3$ index profile was necessary and will be shown.

7.2 Theory

7.2.1 Ti:$LiNbO_3$

The effective index (n_{eff}) is not known precisely before the design of the device, but it can be determined from the universal curves [119] once the refractive index $n_{gi}(y,z)$ of the waveguide is known; where i refers either to the extraordinary (e) or the ordinary (o) refractive index in the case of Ti:$LiNbO_3$. $n_{gi}(y,z)$ can be written as a function of the refractive index of the substrate (n_{ib}) and the maximum change in the refractive index (Δn_i) as [119, 120]

$$n_{ig}(y,z,\lambda) = n_{bi}(\lambda) + \Delta n_i(\lambda) f(y) g(z/D),\ i = e, o. \tag{7.1}$$

In equation (7.1), the $g(z)$ function represents the diffusion shape and it can be an experimentally determined function or a theoretical one in the form of an error function ($erfc(y,z)$), an exponential function ($exp(y,z)$) or a Gaussian function ($exp(y,-(z)^2)$). The function $g(z)$ defines the shape of n_{gi} along the depth of the guide (z-axis) and $f(y)$ defines the lateral shape for a mode propagating along the x-axis.

The diffusion of the metal into the substrate depends on T and t_d and it is characterized by the diffusion depth, given by

$$D_j = \sqrt{2 D_{Tj} t_d},\ j = B, S \tag{7.2}$$

where B and S stand for bulk or surface diffusion respectively. $D_{Tj} = D_0 exp(-T_0/T)$ and it contains the temperature dependent part, where D_0 and T_0 are constants. The later two constants are functions of the material and hence they will be affected by any variation of the material quality [121]. Also, calibration of the furnaces used for the diffusion process may differ hence affecting the absolute temperature of diffusion from one laboratory to another. These factors, together with the temperature dependent diffusion constant, force the need for the optimization of the diffusion function profile at each laboratory.

For a Ti-diffused waveguide, with τ being very much smaller than the substrate thickness and with the diffusion time being long enough for all the metal to be diffused into the substrate, a Gaussian function is found to be more appropriate for the depth function while an error function is found to be suitable for the surface profile. The two functions are given as [120, 122]

Table 7.1: Possible values of p, m and R for a given $n_{eff}(1.55\mu m) = 2.1551$

ring number	p	m	$R(\mu m)$
1	17	443.0003	50.709
2	34	886.0006	101.412
...	...	...	...
k	pk	$m_{k-1}k$	$R_{k-1}k$

$$g(z) = exp(-\frac{1}{2}(\frac{z}{D_B})^2) \tag{7.3}$$

$$f(y) = [erf[\frac{1}{\sqrt{2}D_S}(x + \frac{w}{2})] - erf[\frac{1}{\sqrt{2}D_S(x - \frac{w}{2})}]]/(2erf(\frac{w}{2\sqrt{2}D_S})) \tag{7.4}$$

7.2.2 Nonlinear ring resonator

In a ring or disk resonator, with radius R and effective refractive index n_{eff}, WGM will be at resonance if m number of wavelengths of that mode fits exactly along the circumference of the resonator as

$$m\frac{\lambda_o}{n_{eff}} = 2\pi R.\ m = 1, 2, \ldots \tag{7.5}$$

For a linear resonator, any WGM satisfying equation (7.5) for a given R will resonate. For a nonlinear resonator, on the other hand, where the periodic poling technique is utilized, Λ constrains further the value of R, as only integral p numbers of Λ are allowed. For the first order QPM, the domain constraints are as follows

$$p\Lambda = 2\pi R.\ p = 1, 2, \ldots \tag{7.6}$$

Equations (7.5-7.6) have to be satisfied simultaneously for the operation of this nonlinear resonator. From equations (7.5-7.6), $m = pn_{eff}\frac{\Lambda}{\lambda_0}$ which is in general real since Λ and $\lambda = \frac{\lambda_o}{n_{eff}}$ are all real values. However, for certatin values of p, it is possible for the values of m to come close to integer values for which the above equations (7.5-7.6)will be satisfied. If n_{eff} is known, $\Lambda = \frac{\lambda_0}{2(n^{2\omega}_{eff} - n^{\omega}_{eff})}$ can be determined, m can then be determined from the possible p values, from which the resonating R can be determined. Table 7.1 shows possible values of p, m and R, for a given $n_{eff}(1.55\mu m) = 2.1551$.

7.3 Bend loss

Optical loss in a curved waveguide is due to a combination of the material absorption (α_m), pure bending (α_b) and the scattering (α_w). $LiNbO_3$ is transparent, and α_m is considered to be low, from the fundamental bandgap absorption band-edge around 350 nm to about 5 μm, where phonon absorption starts to occur [7, 123].

Pure bending loses are mainly due to wavefront mismatch between the modes within the bending waveguide and that just radiated from within the bend into the surroundings as the mode negotiates the bends. For a bent waveguide with radius R large enough to inhibit mode conversion, pure bend losses are given by [118]

$$\alpha(R) = C_1 exp(-C_2 R) \tag{7.7}$$

C_1 and C_2 are functions of the bent waveguide and the mode dimension but not of R. That is, both of them depend on the mode confinement, but with C_2 showing much more of the dependence than C_1, so C_2 is considered to have a dominating contribution to $\alpha(R)$ and it is given for the case where n_{eff} varies slightly from the bulk index, n_b, by [118] as

$$C_2 = \frac{2\pi}{\lambda} \frac{(2\Delta N)^{3/2}}{\sqrt{n_b}} \tag{7.8}$$

where ΔN is the modal confinement. From equation(7.8), because C_2 appears in the exponential of the expression in equation 7.7, the bending losses are expected to decrease rapidly with the increase of the modal confinement. Also, the bend radius at which a certain loss occurs moves to smaller radii when make confinement is increased [118]. A ridge waveguide can have a high lateral index contrast and hence minimal bending losses, $\alpha(R) =\leq 0.1 dB/cm$, for a very small R as compared to lower index contrast waveguides. For a Ti:$LiNbO_3$ ridge waveguide, with air as the surrounding medium, ΔN is high enough for our starting radius $R = 50.8 \mu m$ to have minimal pure bend losses and hence a negligible contribution to the total bending loss [118, 54].

Scattering losses are due to the surface roughness on the walls of the ridge waveguide. A mode within the ring cavity sees more of the outer wall than the inner wall more especially with the reduction of the radius of the cavity, and hence the losses will be due to the outer wall quality. For a given mode confinement, the scattering loss for small rings will be higher than that from larger rings. Smaller ring sizes were avoided for our devices due to the need to include more domains within a ring. Besides the quality of the photolithography mask, scattering losses are products of material preparation and they can be minimized by improving the etching method used to achieve the final ridge guide. In the previous chapter, this effect was not considered as the device was to be achieved via

chemical etching, which gives an excellent quality side walls, much better than dry etching.

7.4 Experimental

7.4.1 Photolithography mask design

For z-cut $LiNbO_3$ it is known that $\Delta n_e > \Delta n_o$ after Ti diffusion. This produces smaller w and h when n_e is utilized than when n_o is used. Hence shorter diffusion times and shorter etching times are required for fabrication of a monomode waveguide at a given wavelength. Also, our devices were to be used for nonlinear applications via a QPM process, therefore TM modes will result in more efficient devices as $d_{33} > d_{31} > d_{22}$. It was because of this consideration that we shifted our focus to the TM guiding during our design. The wavelength used for the design was $\lambda = 1.55\mu m$.

An assumed value of $\Delta n_e = 0.01$ was used to determine n_{ig} and the n_{eff} from which R was determined via graphical methods. There is no analytical solution for R, so p was varied until a near integer value of m, with an accuracy of 0.001, was observed. Rings and disks of suitable R with a width, w, were designed and reproduced on a 5 inch Chrome on quartz photolithography mask. Figure 7.3 shows pictures of the designed photolithography mask. In this picture, the ring, rectangular and covered patterns depict the waveguide shapes.

Another photomask, with periodically poled hexagonal patterns placed on the same R values (as the above), was also designed and reproduced on a 5 inch quartz plate with chrome coating. This photomask was made to be used for creating periodically poled patterns on the Ti:$LiNbO_3$ planar waveguide substrate before the patterning rings/disks. These superimposed periodically poled hexagonal patterns are shown schematically in figure 7.3. Figure 7.2 shows a typical flow diagram containing steps that were followed to achieve a ridge waveguide.

7.4.2 Substrate preparation

Rectangular pieces (15 mm $\times$ 10 mm in size) of z-cut $LiNbO_3$ were cleaned in a clean room environment in an ultrasonic bath as follows: Five minutes immersed in acetone, then moved into isopropanol (IPA) for a further five minutes and then into distilled water for a another five minutes. The samples were removed from the ultrasonic bath and blow

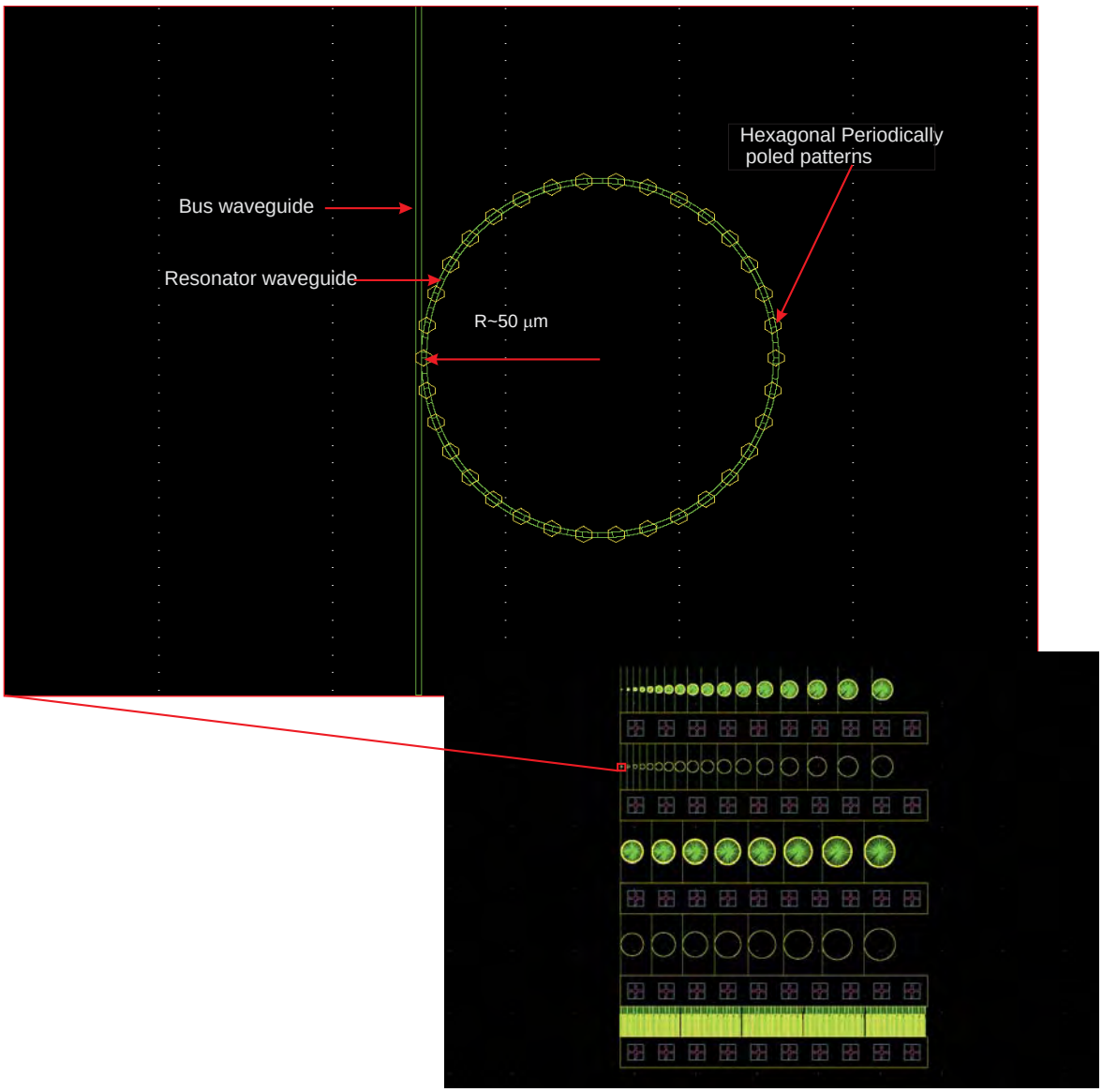

Figure 7.3: Pictures of the designed photomasks with the waveguides and the periodic hexagonal patterns

Table 7.2: Summary of the Ti film thickness used and diffusion time

	$\tau(nm)$		
t(h)	80	100	130
6	TiLN(1)	TiLN(2)	
10	TiLN(3)	TiLN(4)	TiLN(5)
13	TiLN(6)	TiLN(7)	TiLN(8)

dried with N_2 gas.

7.4.3 Ti deposition

An Edward coater (ORC) or Plassy (University of Glasgow) was used to deposit the desired thickness of Ti film on the $-z$ face of the crystal. The Ti film thickness varied from 50 nm to 150 nm depending on the required maximum refractive index change and the final height of the ridge waveguide.

7.4.4 Ti indiffusion

The samples were placed on a platinum mesh bed or silica boat and then placed in a tube furnace. Dry O_2, flowing at 0.5 l/min, was passed through the samples for the entire period while the samples were in the furnace to suppress Li out- diffusion. To avoid spontaneous poling on the sample, due to the temperature in the furnace, the temperature was ramped up to the dwell temperature of 1050 ^oC at a rate of 3 $^oC/min$. The dwell time varied from 6 to 14 hours. The ramp down rate was set to 5 $^oC/min$ but the rate observed was actually less than this because of the good thermal insulation of the furnace. Table 7.2 shows a summary of the different Ti film thickness used together with the corresponding diffusion dwell times.

7.4.5 Poling of Ti:$LiNbO_3$

A similar method used by Broderick *et al.* [117], to fabricate hexagonal domain inverted area z-cut $LiNbO_3$, was used in this work on Ti:$LiNbO_3$. A 1 μm, thin Shipley S1813, photoresist was deposited on the -z face of the Ti:$LiNbO_3$ planar waveguide and then photo-lithographically patterned with the aid of a photomask containing hexagonal patterns. The samples were arranged so that the flat side of the hexagons in the mask was aligned with a y-direction of the Ti: $LiNbO_3$ sample.

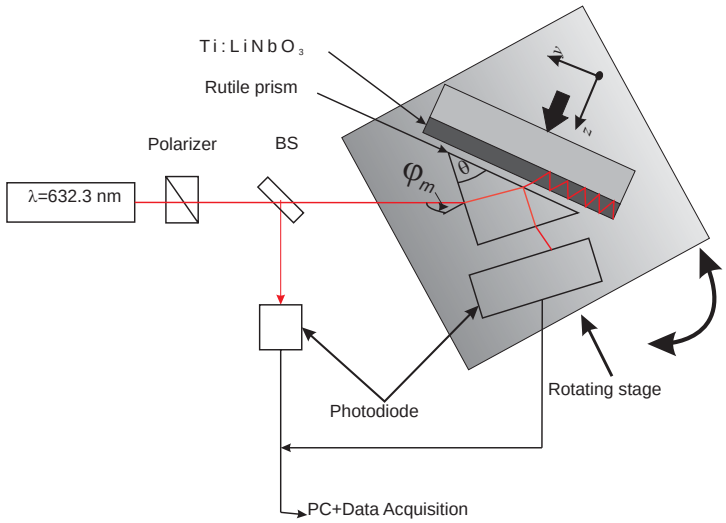

Figure 7.4: A schematic diagram for a prism coupling setup used for the determination of n_{eff}. BS = beam splitter

7.4.6 Determination of n_{eff}

The effective refractive index (n_{eff}) of the planar $LiNbO_3$ waveguide modes were determined by a prism coupling setup, as shown in figure 7.4. A polarized laser beam, with $\lambda = 632.3nm$, was passed through a beam splitter (BS) before arriving on the rutile prism at a incident angle of ϕ_m. The rutile prism, the planar waveguide and the photodiode detecting the reflected beam from the rutile prism were all mounted on a rotating stage. The waveguide sample was compressed slightly against the prism until a coupling spot was observed. The table was rotated to vary ϕ_m while the reflected signal from the interface between the prism and the waveguide was recorded. The recorded signal was normalized against the one partially reflected by the BS. The presence of modes was observed by dips on the normalized signal corresponding to the reflection loss due to mode coupling into the waveguide. With the angle θ (as shown in figure 7.4) known, together with the refractive index of the rutile and the substrate for the polarization used, n_{eff} was determined for the selected angle of polarization used.

Once the n_{eff} was known, the desired final height of a ridge waveguide, required to give a monomode output at 1550 nm, was calculated to determine the required thickness of the SU 8 photoresist. The thickness of the SU8 photoresist was set to be about two times the height of the ridge, due to the different etch rate between the photoresist and $Ti:LiNbO_3$.

7.4.7 Applying photoresist

SU 8 10 photoresist (SU 8 optimized for 10 μm thickness)(MicroChem) was poured slowly on the sample that was placed on a spinner. The photoresist was allowed to cover the whole sample with a uniform volume. The spinner was set as follows: start from 0 rpm, accelerate at 100 rpm/s to 500 rpm, dwell for 5 s, accelerate at 300 rpm/s to 3000 rpm. At 3000 rpm, the dwell time was varied to obtain the required photoresist thickness and then the spinner was decelerated to 0 rpm at 500 rpm/s. A 30 s dwell time was used to obtain the SU8 with an average thickness of 9.9 μm.

7.4.8 Soft bake

The samples were removed from the spinner and placed directly on a hot plate that was set at room temperature. The temperature of the hot plate was ramped up at 3 $^oC/min$ to 95 ^oC and left there for the sample to soft bake for 5 min and then the hot plate was switched off. This dwell time was enough to evaporate the solvent for the SU 8 thickness of less than 11 μm. The samples were then returned slowly to room temperature.

7.4.9 Exposure

The power density calibration values of the MA6 mask aligner, (16.3 $\rightarrow$ 17.2 $mWcm^{-2}$), were used to determine the required time of exposure. A recommended energy density, (100 $mJcm^{-2}$) for 10 μm, supplied by the photoresist provider were used as a guideline to obtain the optimized exposure time for our SU 8 thicknesses. The measured width and the profile of the SU 8 ridges were used to quantify the exposing conditions. The required width of 3 μm and a better ridge profile were obtained with 5 $\rightarrow$ 6 s for 8.5 to 9.5 μm SU8 thicknesses.

7.4.10 Post exposure bake

From the mask aligner the samples were post baked on a hot plate at the same temperature as the soft bake. The baking profile differed only by the shorter dwell time of 2 min as compared to the soft bake.

7.4.11 Development

Within 30 *min* of exposure, the samples were immersed in an Microposit EC solvent (Chestech Ltd, UK) for 30 *s*, then in a new Microposit EC solvent for 15 *s*, 15 *s* in IPA. During immersion in the solvent, the samples were strongly shaken. The samples were then gently dried with N_2.

7.4.12 Dry etching of the ridge waveguide

When the refractive index profile was known and the depth of the ridge was determined from the BPM simulations, the SU 8 patterns on the planar waveguides were transferred into the planar waveguide via dry etching. Figure 7.5 shows the optical micrograph of the developed SU 8 patterns on the Ti:$LiNbO_3$ planar waveguide before they were etched.

Initial attempts to achieve optimum conditions for dry etching at Glasgow University suffered from material re-deposition after etching, as shown in figure 7.7. Reactive ion etching (RIE) of the SU 8 masked Ti:LiNbO3 waveguide was performed using Ar^+:O_2 chemistry using a RTE340 (Electrotech SRC PlasmaFab340). A gas rate of 30/3 Ar^+/O_2 sccm was used with an open valve (lowest pressure available) and the power of the RTE 340 was set to 130W. The temperature on sample stage was kept at 20^oC. The samples were kept on a flat surface during dry etching for a total period of 3 hours in three hour-long steps.

One major problem which will lead to major optical loss can be observed from these optical micrographs. Because the gap between the ring/disk and the bus waveguides was defined to be zero in the photolithography mask, the contact area between the ring and the bus waveguides is distorted. This problem should be solved as it will affect the coupling efficiency of the mode in and out of the resonator and also degrade the mode propagating along this contact. However, as we needed to optimize the etching conditions, these structures were used anyway.

Because the etch rate of a non-hard-baked SU 8 is about 1.5 times higher than that of $LiNbO_3$ or Ti:$LiNbO_3$, a thicker SU 8 photoresist ($h_{SU8} \approx 1.5h$) was used so that the desired h is achieved when all of the SU 8 etches away.

Figure 7.6 shows an SEM macrograph of the developed SU 8 patterns on a $LiNbO_3$ substrate. This figure shows that the width of the SU 8 is already greater than the corresponding width on the photolithography mask ($3\mu m$) and also that the top part of the photoresist is wider than the bottom part. This problem occurs during the UV

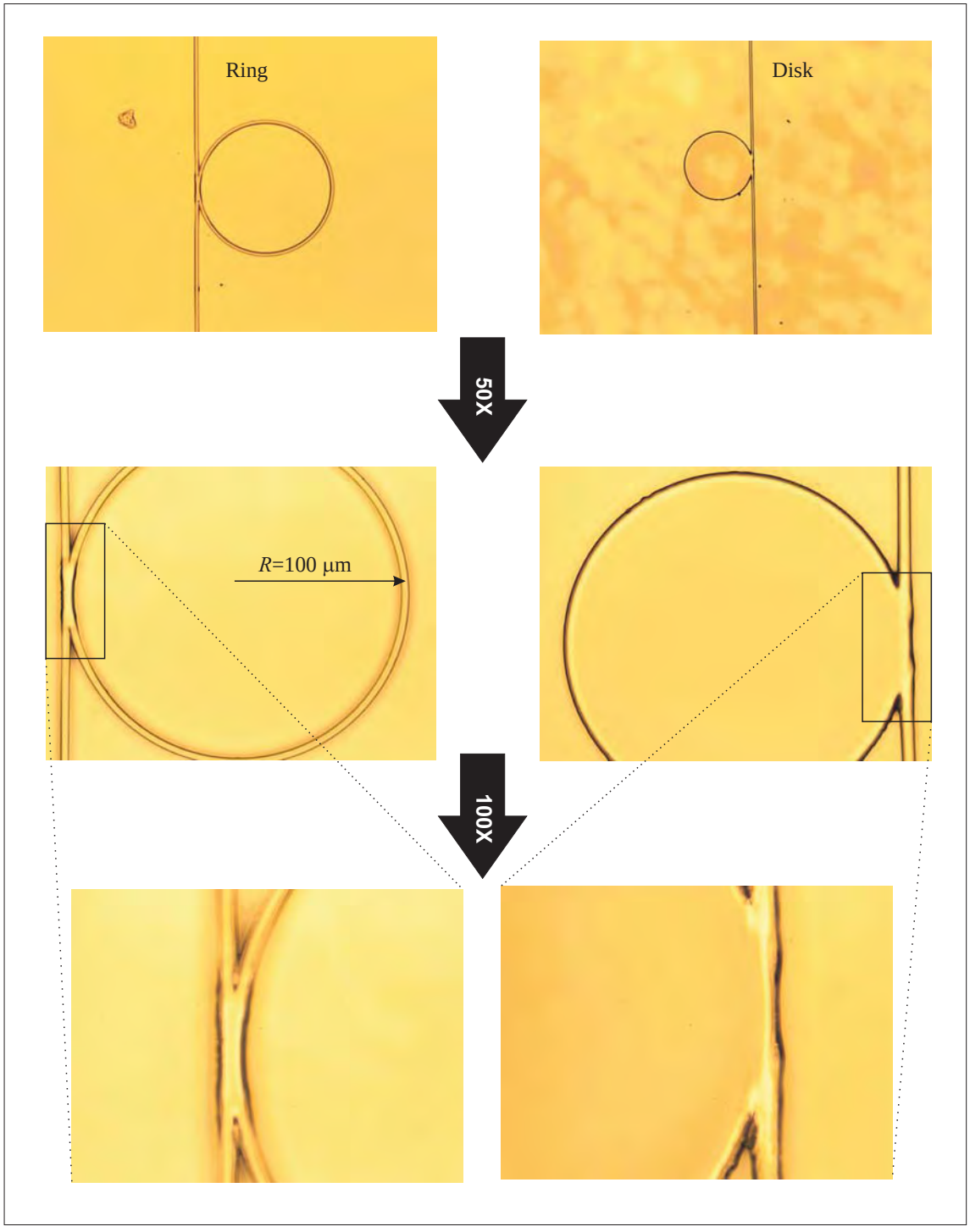

Figure 7.5: Optical micrograph of the developed SU 8 photoresist patterns on a Ti:$LiNbO_3$ planar waveguide before dry etching

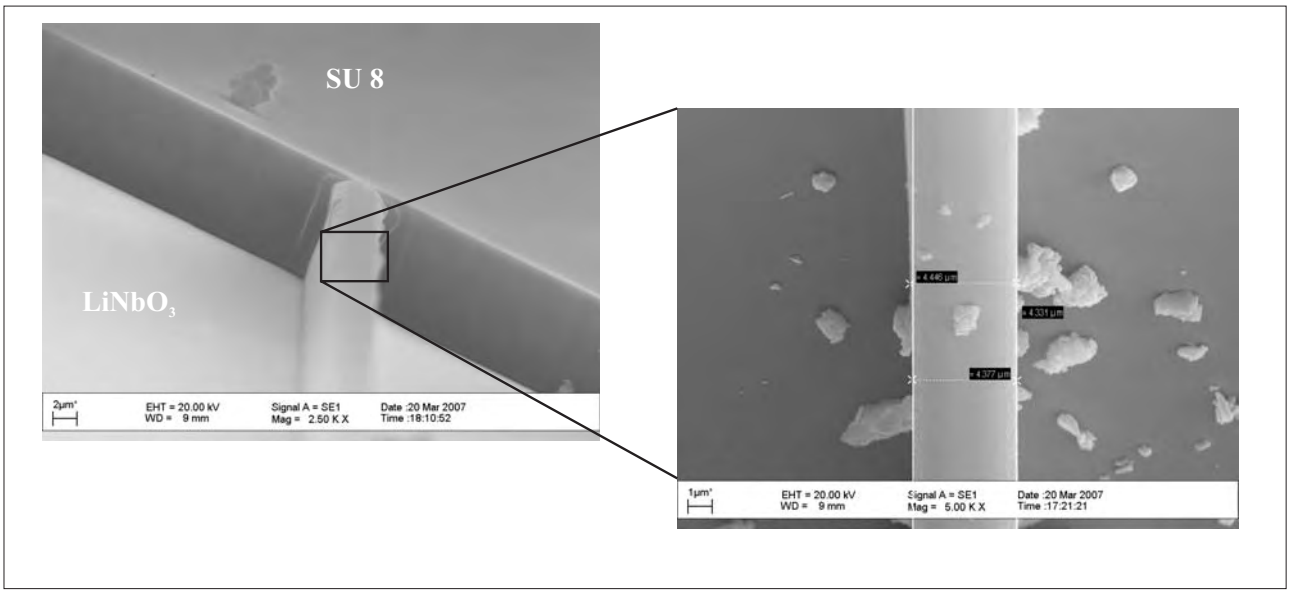

Figure 7.6: SEM micrograph of the developed SU 8 photoresist patterns on a $LiNbO_3$ substrate before the dry etching

exposure and is caused by UV beam diffraction within the gap between the photomask and substrate [124]. Although the hard contact mode was used during exposure, any irregularity on the substrate will introduce a gap. This problem can be resolved by applying a matching fluid in-between the mask and the substrate. However, due to time constraints such corrections were not attempted in the frame of this work.

Although the re-deposited material was removed, by wet etching with 48% HF for 15 min, the quality of the ridges was compromised by the chemical etching of the Ti:$LiNbO_3$ layer. Additionally, due to the normal incidence of the plasma during the dry etching, the etched samples showed a very shallow angle of the ridge wall. This angle is very bad as it will prevent the bus and the resonator wall from coming close to each other, which is necessary to allow close proximity, for proper evanescent mode coupling between the two. Both of the above dry etching problems have to be resolved before a better ridge waveguide can be achieved.

In an attempt to resolve the re-deposition of material during dry etching, the samples were sent to Oxford Instruments (OF) which houses some of the dedicated dry etching apparatus. Figure 7.8 shows our etched samples as returned from OF. The re-deposition seems to have been minimized, however there appear to be other problems, as shown in this figure, such as the two steps along the depth of the ridge. About the same time as

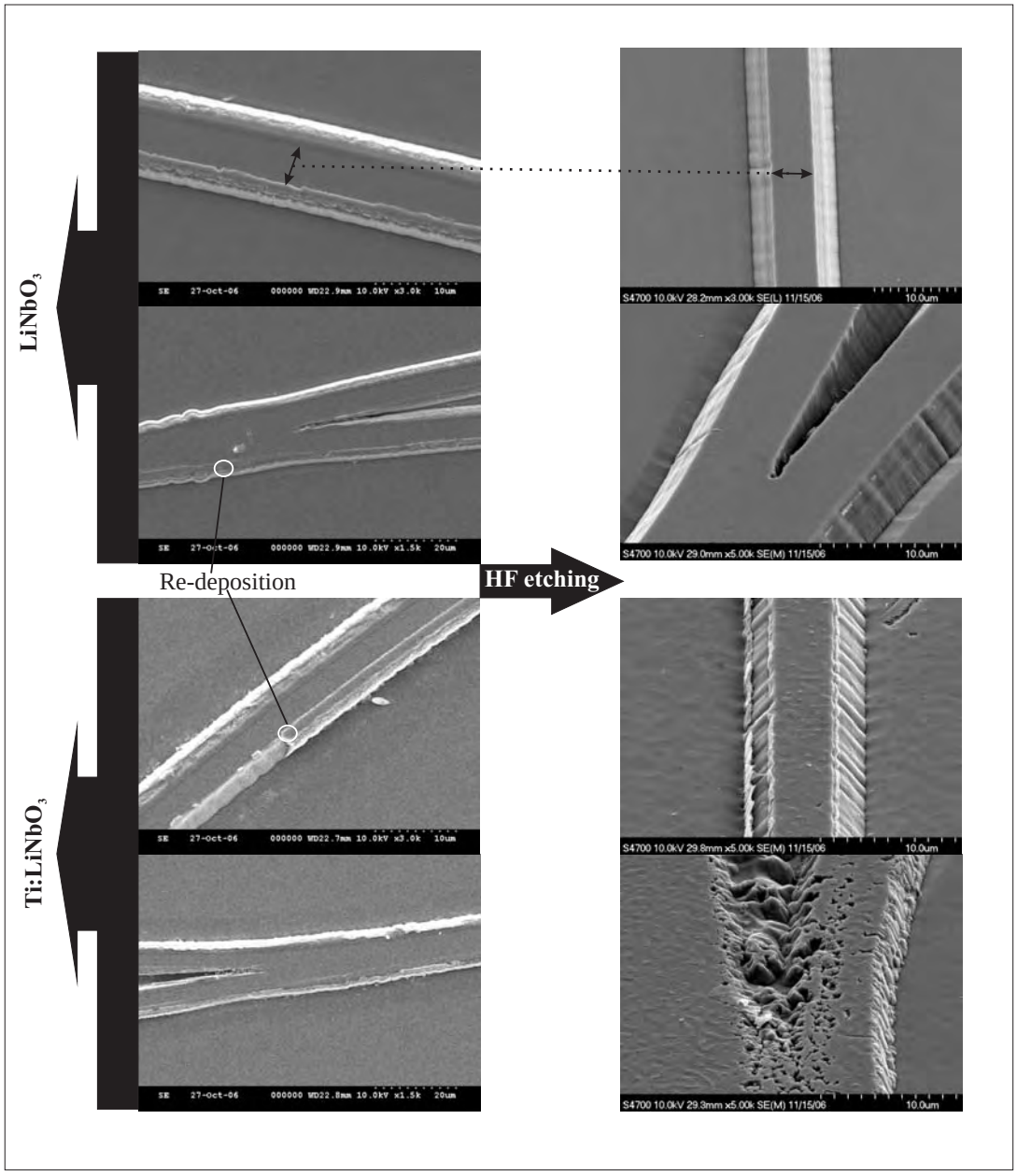

Figure 7.7: SEM micrograph of the etched $LiNbO_3$ substrate Ti:$LiNbO_3$ waveguide before and after they were chemically etched by concentrated HF acid

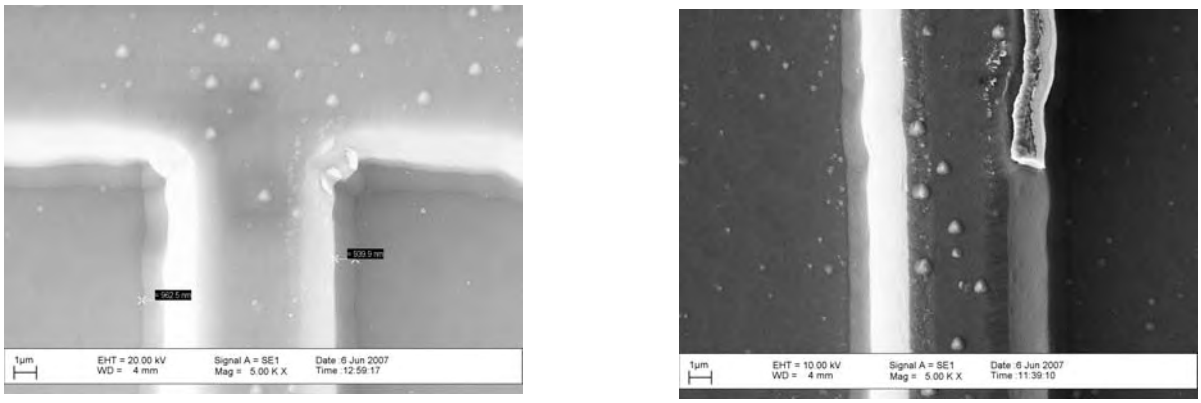

Figure 7.8: SEM micrograph of the dry etched Ti:$LiNbO_3$ waveguide

we were sending the samples to OF, our temporary clean room facility in Southampton was put in place and OF was expected to come and install their equivalent dry etching apparatus in our clean room, hence this work was delayed while waiting for the installation. However, the installation took much time and we could not continue with the work.

Dry etching seems to be the bottleneck for the successful fabrication of ring resonators based on ridge waveguides. Due to time constraints, the dry etching problems were not investigated sufficiently and they should be revisited in future studies.

The above problems have halted, for now, the success of the fabrication of Ti:$LiNbO_3$ ring resonators in our laboratory. The formation of domains along the path of the waveguides was not explored as the priority was to fabricate a ring resonator first.

7.5 Results and Discussion

7.5.1 Effective index

Figures 7.9 and 7.10 show the TM and TE modes, observed from the planar Ti:$LiNbO_3$ fabricated under different experimental conditions, at $\lambda = 632.8$. For a given waveguide, with the same τ and diffusion dwell time, there are more TM modes than TE modes which is as expected since Δn_e is larger than Δn_o for the $LiNbO_3$ crystal.

Table 7.3: Summary of the measured n_{eff} of the planar Ti:$LiNbO_3$ at $\lambda = 632.8$ nm

		$\tau(nm)$		
t(h)	mode	80 (TM; TE)	100 (TM; TE)	130 (TM; TE)
6	0		(2.22025; 2.2955)	
	1		(2.21050; 2.29071)	
	2		(2.20500; ——-)	
10	0	(2.21340; 2.29350)	(2.21685; 2.29430)	(2.22025; 2.29535)
	1	(2.20820; 2.29065)	(2.2101; 2.29075)	(2.21300; 2.29155)
	2	(2.20505; 2.28830)	(2.2055; 2.28840)	(2.20275; 2.2889)
13	0		(2.21430; 2.29380)	(2.21915; 2.29525)
	1		(2.20950; 2.29115)	(2.21310; 2.29200)
	2		(2.20610; 2.28905)	(2.20820; 2.28850)
	3			(2.2057;———)

The effect of a longer dwell time is to push the waveguide modes deeper into the bulk without affecting the overall mode number. For ridge waveguides, the dwell time needs to be controlled as it will affect the required height of the ridge, i.e, a single mode waveguide (corresponding to longer dwell time) will be deeper in the substrate and hence a taller ridge will be required to guide the mode effectively.

As τ increases so does the number of modes. However, the bigger τ also implies a longer dwell time to make sure that no Ti is left undiffused at the surface which will then result in greater surface loses.

From this discussion, TiLN(4) and TiLN(5) seem to stand a better chance of being single mode at 1550 nm.

7.5.2 BPM simulation

Figure 7.11 shows the n_e index profile at 632.8 nm, for τ= 100 nm and dwell time = 6 h, obtained from the slab mode solver for a given 1D Gaussian diffusion profile through the use of OlympoiS slab mode solver. This corresponds to the index profile of Ti:LN(2) sample in figure 7.9. The diffusion constants were varied until only three TM modes were observed, as shown in figure 7.9.

A dispersion factor, $\Delta n = f(\lambda)$ [121, 125], was included before the same Gaussian diffusion profile and diffusion constant were used to calculate the index profile and mode at $\lambda = 1550$ nm, as shown in figure 7.11 and 7.12 respectively.

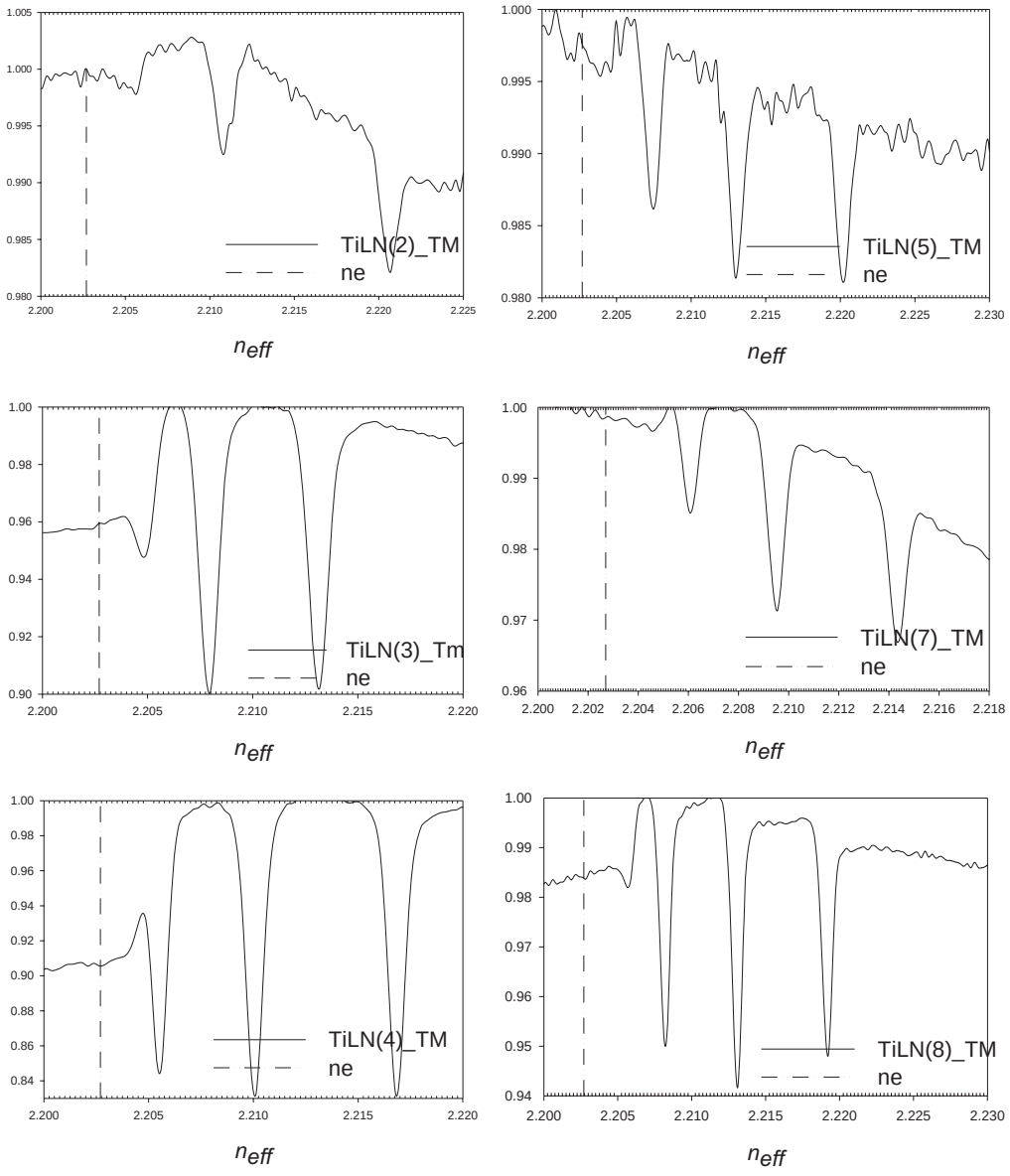

Figure 7.9: Planar TM modes at 632.8 nm for different Ti film thickness (τ) and dwell time (t). See table 7.2

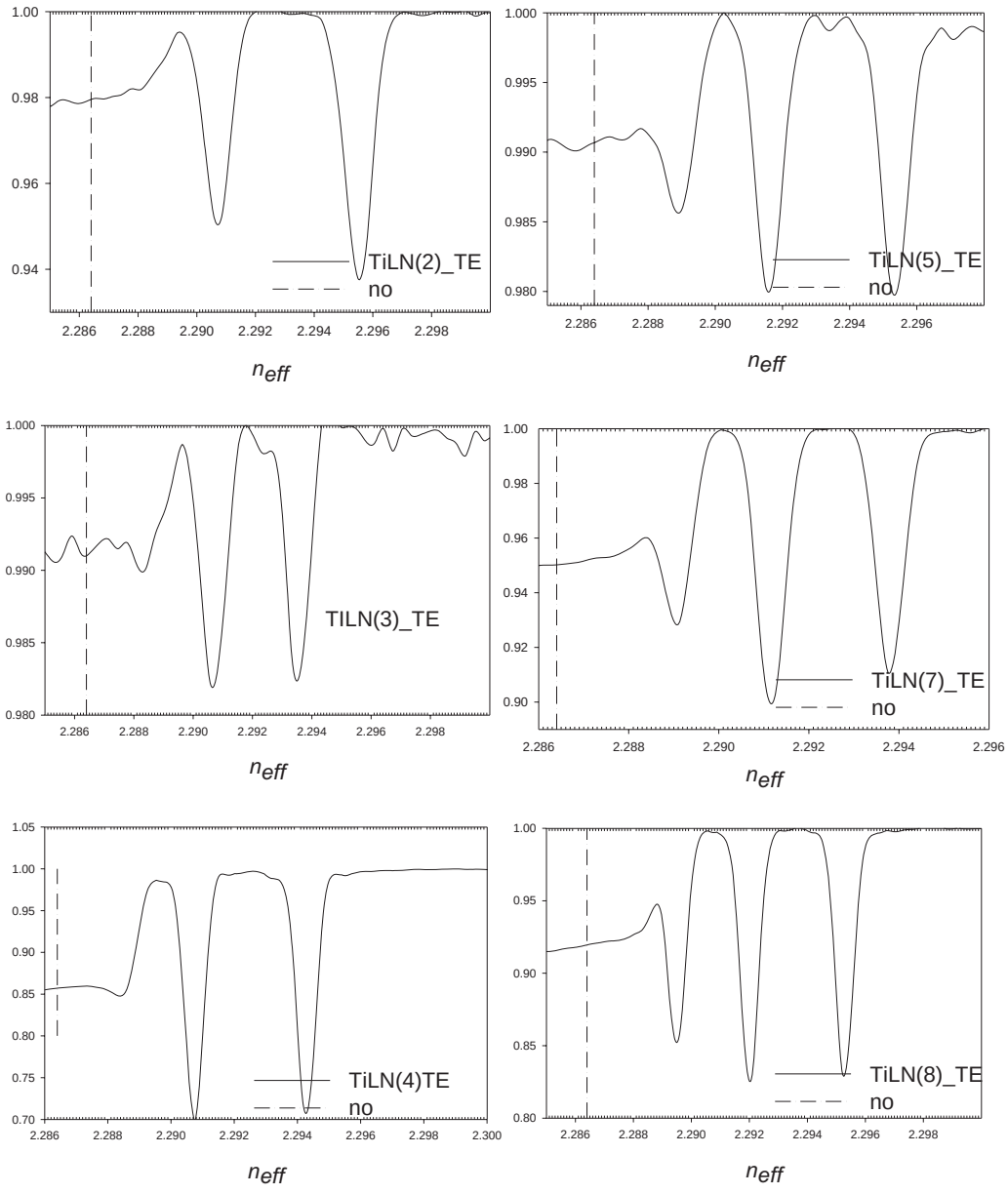

Figure 7.10: Planar TE modes at 632.8 nm for different Ti film thickness (τ) and dwell time (t). See table 7.2

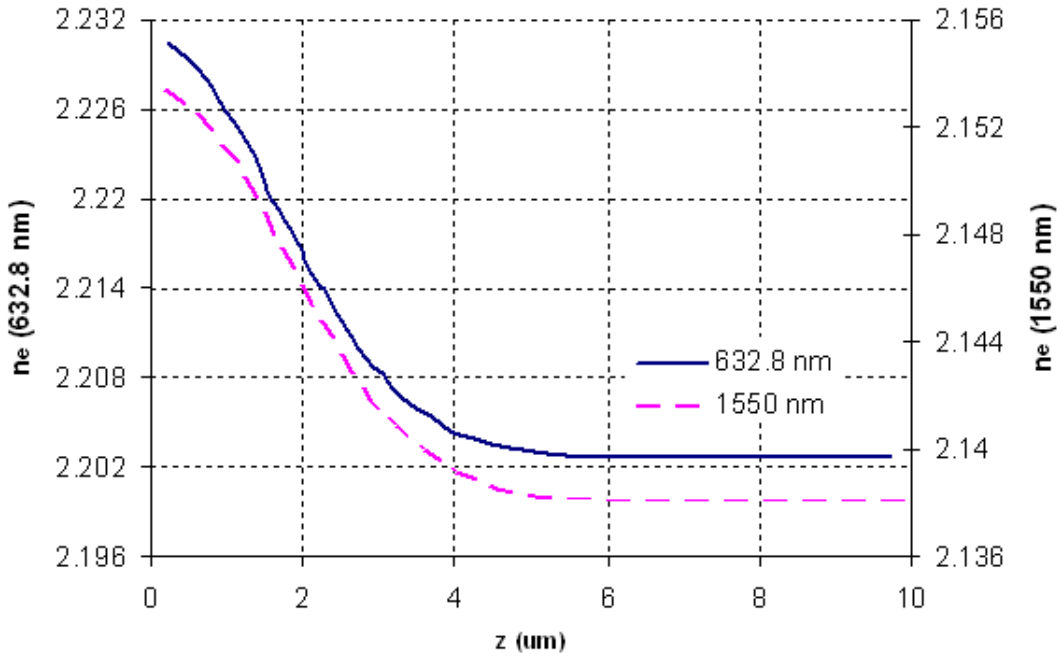

Figure 7.11: n_e index profile at 632.8 nm and 1550 nm for τ=100 nm and t= 6 h extracted from slab mode solver.

To obtain the height (h) of the ridge waveguide, the cross-section BPM mode solver (OlympioS Selene) was employed. The width (w) of the ridge was fixed to 3 μm during the design of the mask. Due to the large index contrast between the surrounding air and the waveguide, any widths larger than 0.5 μm will correspond to multimode structures at the wavelength used. However such a small width is not practical since it is at the resolution of photo lithography hence it will be difficult to achieve.

The optimized diffusion profile obtained from the measured n_{eff} at λ = 632.8 nm and slab mode solver was used for the refractive index of the waveguide at λ=1550 nm.

Figure 7.13 shows a simulated single TM_{00} mode at λ = 1550 nm with $w = 5\mu$m and TiLN(8) profile, (i.e. τ = 130 nm and dwell time = 13 h). For this diffusion profile, h needs to be above 3 μm for the mode to be more confined in the strip of the ridge. A longer dwell time pushes the modes deeper into the substrate hence requiring a higher h. For $h \geq 6\mu m$, the undesired TM_{01} starts to appear. The waveguides design of $4\mu m < h < 6\mu m$ was then selected, the h value depending on the dwell time, with the shorter dwell time corresponding to the shorter h.

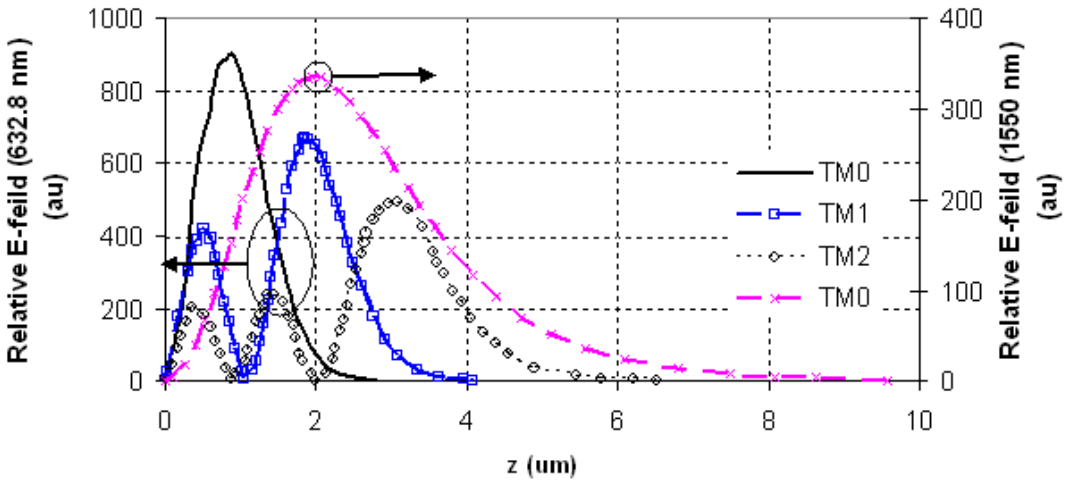

Figure 7.12: Modes and single mode at 632.8 nm and 1550 nm, respectively. for τ=100 nm and t= 6 h extracted from slab mode solver.

Note that more of the modes need to be in the strip part of the ridge for effective coupling as these ridge waveguides are to be used for the fabrication of a ring resonator. Though $h = 3\mu m$ is small for TiLN(8) , it can be sufficient for TiLN(5) as it has less dwell time (10 h). However, from the n_{eff} shown in figure 7.9, the quality of the modes was poor, suggesting that there may be some undiffused Ti on the surface. It was then concluded that in the future both the TiLN (5) and (8) design will be avoided due to the above constraints.

7.6 Conclusion

In this chapter, the theory to achieve a nonlinear microcavity by periodically poling ring/disk resonators was introduced. This theory was based on the operation of a circular microcavity made of a Ti:$LiNbO_3$ ridge waveguide. The design of the fabrication process of a periodically poled QPM SHG optical waveguide microcavity was discussed and the fabrication steps were attempted. The optimization of the fabrication of the Ti:$LiNbO_3$ was detailed and problems associated with dry etching were highlighted. Demonstration of the operation of the devices was hindered by the dry etching problems and they will need to be resolved before the device can be realized.

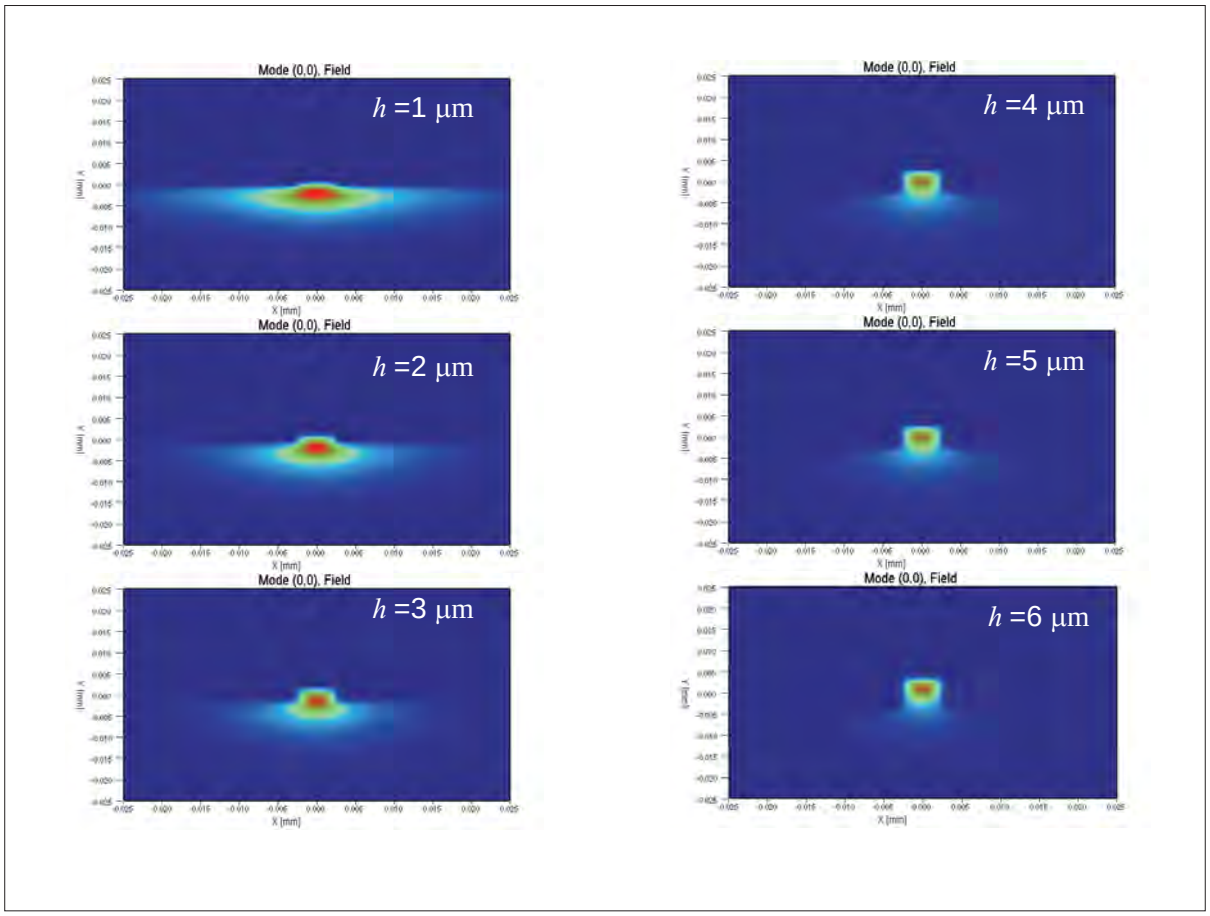

Figure 7.13: Single mode at 1550 nm for τ=130 nm and t= 13 h obtained using the BPM solver.

Chapter 8

Conclusions and Further work

8.1 Conclusions

In this chapter, I summarize the work presented in the previous chapters and present recommendations for future work.

Chapter 2 summarizes the physical properties of $LiNbO_3$ crystals in which important properties such as ferroelectricity, the Sellmeier equations, domain inversion, etc, have been discussed. From these properties, it is clear that this material is suitable to the scope of this thesis, namely, for use in the RSHG experiments, and microcavity experiments for nonlinear applications.

In chapter 3 the theory of surface SHG was discussed, in particular a three-layer model (see ref [60]) was discussed in detail. From the three-layer model, the equations (3.29-3.31) describing the variation of the SH with the input/output polarization angles γ/Γ and azimuthal angle ϕ were formulated. Equations (3.29-3.31) were then used in chapter 4 to describe the observed SH signal from the experimental results. In this chapter I have also discussed the experimental setup for the RSHG experiments.

In chapter 4, RSHG experiments were used to determine the symmetry of the interfacial layer of a z-cut $LiNbO_3$ crystal with a known crystal axis. For $\gamma = \Gamma = s$ the rotation anisotropy results shows six maxima over a 360 ^{o} rotation of the sample as shown by figure 4.2. With this polarization combination only the anisotropic term in $E^{2\omega} = A'K(\phi)$ contributes to any observed SHG signal. For the case where $\gamma = \Gamma = p$, the largest isotropic term B' dominates due to the large value of χ_{zzz} and the six maxima are reduced to three as a consequence and are shown in figure 4.3. From these results it was concluded that the interfacial layer has the same symmetry as that of the bulk medium.

The use of RSHG experiments to detect the signal difference from the poled and non poled faces was described in this chapter. The aim was to compare, for example, the SH signal generated from the $+z$ and $-z$ faces of the poled and non-poled regions, respectively. A set of results has shown the signal difference between the two regions at a given ϕ, γ, Γ and are presented in figure 4.5. This was however unsuccessful because the results were not consistent. The inconsistency was attributed to a couple of parameters, one of them being the fluctuation of the fundamental laser beam and the other being the domination of the bulk properties for which no difference between the two faces can be seen.

On the other hand, RSHG experiments were conducted successfully to shows that the y axis does invert direction during poling. During poling, $+z$ changes to $-z$, in which case the order of the cation, Nb^{+5}, Li^{+}, Vacancy, Nb^{+5}, along the z axis also reverses as shown in figure 4.6. The changes along the z axis force the change of the order of the cation along the y axis in between the oxygen layer. This is presented in figure 4.6 and this results have been published in a journal [33].

Chapter 5 introduces polygonal microcavities and their properties for application in linear optics, and chapter 6 demonstrates a hexagonal microcavity for nonlinear applications. In chapter 5 the theory governing mode propagation and mode resonance within a microcavity was detailed. It was shown that for a mode to resonate in a hexagonal microcavity a wavefront matching condition given by equation (5.30) should be satisfied. In this work, resonating modes with a 60^o incident angle were considered only.

Properties of the hexagonal microcavity such as the Q-factor, FSR and the effect of rounding the hexagonal corners of the cavity were investigated at a given resonating wavelength (λ_0). For $\lambda_0 = 959nm$, one of the ideal cavity sizes was calculated from equation (5.30), and was confirmed by FDTD shown in figure 5.6 to be $\alpha = 2.97\mu m$ for a s-polarized FW in a z-$LiNbO_3$ crystal. The FSR for in this cavity was found to be 48 μm. For a regular hexagonal microcavity, a Q-factor of 180 was calculated from the FDTD simulation. For such a low Q-factor cavity, it takes only 10 round trips before the cavity reaches steady state.

This low Q-factor was attributed to high cavity losses at the corners of the hexagon, and the effect of rounding the corners of the hexagon shows an increase in Q-factor. This is presented in figure 6.9. The limitation of the Q-factor at maximum rounding ($\frac{R}{\alpha} = 50\%$) is no longer due to the corners but due to the bending losses, which are a

function of the refractive index contrast and the size of the cavity. A smaller cavity like the one used in this study will have higher bend losses than a larger cavity at the given refractive index contrast.

Rounding the corners also changes the overall cavity size and the shape of the cavity. Consequently the resonating wavelength and the form of mode propagation in the cavity changes. Figure 6.10 shows the resonating wavelength shift within the ideal cavity size determined for the regular hexagon. It was also observed that when rounding the corners to a value of $\frac{R}{\alpha} > 20\%$ the form of propagation changes from a six-bounce to a WG kind of propagation. Within $\frac{R}{\alpha} = 20\%$ the shift of the resonating wavelength was found to be small ($\delta\lambda \approx 1nm$) compared to that of $\frac{R}{\alpha} > 20\%$. It was then concluded that rounding of cavity corners up to 20% is sufficient to increase the Q-factor.

In chapter 6, a further requirement was imposed on the ideal cavity size for the FW by making such a cavity also resonate at $\frac{\lambda_0}{2}$. An example of this is the SH from SHG. This means that the cavity doubly resonates.

For practical nonlinear application of the microcavity, the nonlinear process takes place *in situ* within the cavity from the FW, and the condition to favour this nonlinear process was also included in the cavity. Therefore, such a doubly resonant microcavity was further made to allow phase matching to occur. A model for TIR-QPM in a doubly resonating hexagonal cavity was then developed according to equation (6.4-6.6). From the model some ideal cavity sizes were found for $\lambda_0 = 959nm$ to be $\alpha_1^m = 2.98\mu m$, $\alpha_2^m = 12.73\mu m$ and $\alpha_3^m = 22.35\mu m$, ...

In figure 6.2 I have made a comparison of the SHG yield between different phase matching processes. In that figure the most efficient process was shown to be the PPM followed by TIR-QPM for ($l_1 < l_c$) and the QPM method, respectively, in non-resonant devices. The reason for the TIR-QPM with ($l_1 < l_c$) being better than the QPM was attributed to the phase matching which is achieved in the devices when the TIR-QPM with ($l_1 < l_c$) process is set-up. In the QPM process the phase matching is achieved at l_c by reversing the sign of the $\chi^{(2)}$. For example, while in the (TIR-QPM($l_1 < l_c$)) the phase matching is achieved by balancing the Fresnel phase shift and the dispersion phase shift which in this case occurs at $l_1 < l_c$. Thus the SHG starts to grow faster in the (TIR-QPM($l_1 < l_c$)) case than that in the QPM, and was shown in figure 6.2.

I compared the TIR-QPM processes for different values of l_1 and I have shown that

(TIR-QPM($l_1 < l_c$)) > (TIR-QPM($l_1 > l_c$)). This implies that for three ideal cavity sizes $\alpha_i^m, i = 1, 2, 3,$, the most efficient one will be that for the small α in a non resonating cavity. However, for resonating cavities such as the doubly resonant one in this study, the small cavity size was found to lose resonance very quickly hence leading to a low Q-factor. I have since shown that the bigger the cavity size (as is the case with our hexagonal devices) the higher the Q-factor. In addition the resonating nature of our hexagonal device gives rise to a higher SHG yield for this cavity compared to that of non-resonance QPM devices with a longer length (90 times longer). That, is if the length of the QPM and TIR-QPM were the same and the starting FW power was the same, the TIR-QPM will show a higher efficiency because both the FW and SH will be amplified on resonance.

From our study a few major parameters were not dealt with, one of them being how much of the FW will actually couple into the cavity from the bus waveguide to excite the cavity mode? The work in this chapter needs an analysis in terms of how to practically achieve firstly the six-mode propagation via evanescent coupling and secondly how to achieve doubly resonant TIR-QPM in practice. For a linear hexagonal microcavity this coupling was achieved and demonstrated by varying the width of the bus waveguide until a resonant mode was launched in the cavity. This is yet to be demonstrated for a double resonant microcavity. A practical demonstration of the device is required to confirm that works and this work is presently continuing at the ORC.

In this chapter, the theory to achieve a nonlinear microcavity by periodically poling ring/disk resonators was introduced. This theory was based on the operation of a circular microcavity made of a Ti:$LiNbO_3$ ridge waveguide. The design of the fabrication process of a periodically poled QPM SHG optical waveguide microcavity was discussed and the fabrication steps were attempted. The optimization of the fabrication of the Ti:$LiNbO_3$ was detailed and problems associated with dry etching were highlighted. Demonstration of the operation of the devices was hindered by the dry etching problems and these will need to be resolved before the device can be realized. The problem with dry etching has been attributed to the choice of the etch mask which in this case was SU 8. A thick etch mask with SU 8 is not avoidable due to the low SU 8/$LiNbO_3$ selectivity of about 1.5 and low vertical index contrast (< 0.01) of the Ti:$LiNbO_3$ waveguide. An effort should be made to try a metal mask such as Cr [126] in order to improve the selectivity required.

8.2 Further Work

In the first part of this thesis, the potential usage of the RSHG technique as a non-destructive tool to test and quantify the degree of poling on the sample was presented. To continue this work, the use of a stable laser beam should be considered for the reproducibility of the method. In addition, the choice of λ of the FW should be reduced further from 532 nm to push the SH deeper in the UV region such that this RSHG technique is surface specific and the bulk contribution is further minimized. There is no expected SHG difference through the bulk of the crystal so the increased bulk contribution on the measured reflected SHG will limit this application.

In the second part of this thesis the potential usage of microcavities for nonlinear applications was shown and the problems encountered were discussed.

One of the obstacles in achieving a circular microcavity was due to the taller ridge height required with our choice of waveguide. The taller height requirement can be further reduced if annealed H:$LiNbO_3$ is used instead of Ti:$LiNbO_3$ waveguide. This is because Δn_e for proton exchange waveguide can be ten times lager than that of a titanium in-diffused waveguide which leads to a smaller ridge height of the order of 1 μm [127]. Annealed proton exchange has been shown to have recovered d_{33} values to that of the bulk $LiNbO_3$ crystal as compared to non-annealed proton exchange [128]. The limitation of guiding only the extraordinary wave by a H:$LiNbO_3$ waveguide is overlooked by the fact that d_{33} will be accessed in this polarization.

The phase matching capability of $LiNbO_3$ is superior compared to that of semiconductors as a platform for non-linear microcavities. Hence the use of $LiNbO_3$ as a platform for microcavities for non-linear applications in this work. However, flexible phase matching process such as TIR-QPM have recently been demonstrated in semiconductor materials [5]. This together with the high values of $\chi^{(2)}$, Δn and the maturity of the semiconductor fabrication processes present opportunities for the investigation of the use of semiconductors in microcavities for non-linear applications.

The numerical work discussed in this thesis can be improved by estimating the generation of SHG *in situ* for given input power of the FW and coupling strength. This can be achieved by using the ideal cavity sizes presented in this work, defining the non-linearity of the material and launching only the FW through the bus waveguide to generate the SHG within the cavity. The FDTD methods used in this work should be optimized to allow phase matching process such as TIR-QPM to occur within the cavity.

Bibliography

[1] M. Ohgaki, K. Tanaka, and F. Marumo, "Structure refinement of lithium (i) niobium (v) trioxide, $LiNbO_3$, with anharmonic thermal vibration model," *Mineral. J.*, vol. 16, no. 3, p. 150, 1992.

[2] L. O. Svaasand, M. Eriksrud, G. Nakken, and A. P. Grande, "Solid-solution range of $LiNbO_3$," *J. Cryst. Growth*, vol. 22, p. 230, 1974.

[3] C. L. Sones, S. Mailis, W. S. Brocklesby, R. W. Eason, and J. R. Owen, "Differential etch rates in z-cut $LiNbO_3$ for variable HF/HNO_3 concentrations," *J. Mater. Chem.*, vol. 12, p. 295, 2002.

[4] M. M. Fejer, G. A. Magel, D. H. Jundt, and R. L. Byer, "Quasi-phase-matched second harmonic generation: Tuning and tolerances," *IEEE J. Sel. Top. Quantum Electron.*, vol. 28, no. 11, p. 2631, 1992.

[5] R. Haidar, N. Forget, P. Kupecek, and E. Rosencher, "Fresnel phase matching for three-wave mixing in isotropic semiconductors," *J. Opt. Soc. Am. B: Opt. Phys.*, vol. 21, no. 8, p. 1522, 2004.

[6] R. Haidar, "Fractinal quasi-phase-matching by Fresnel birefrigence," *Appl. Phys. Lett.*, vol. 88, p. 211102, 2006.

[7] U. Schlarb and K. Betzler, "Refractive indices of lithium niobate as a function of wavelength and composition," *J. Appl. Phys.*, vol. 73, no. 7, p. 3472, 1993.

[8] A. M. Mamedov, "Optical properties (VUV region) of $LiNbO_3$," *Opt. Spectrosc.*, vol. 56, no. 6, p. 645, 1984.

[9] E. Wiesendanger and G. Guntherrodt, "Optical anisotropy of $LiNbO_3$ and $KNbO_3$ in the interband transition region," *Solid State Commun.*, vol. 14, p. 303, 1974.

[10] J. A. Armstrong, N. Bloembergen, and J. D. P. S. Pershan, "Interaction between light wave in a nonlinear dielectric," *Phys. Rev.*, vol. 127, no. 6, p. 1918, 1962.

[11] H. Komine, W. H. long, J. W. Tully, and E. A. Stappaerts, "Quasi-phase-matched second-harmonic generation by use of total-internal-reflection phase shift in galliun arsenide and zinc selenide plates," *Opt. Lett.*, vol. 23, no. 9, p. 661, 1998.

[12] A. M. Prokhorov and Y. S. Kuzminov, eds., *Physics and Chemistry of Crystalline Lithium Niobate*. Adam Higer, New York, 1990.

[13] P. Rejmankova, J. Baruchel, P. Moretti, M. Arbore, M. Fejer, and G. Foulon, "Visualization of inverted ferroelectric domains in $LiNbO_3$ by x-ray topography," *J. Appl. Cryst.*, vol. 31, p. 106, 1998.

[14] A. Boulle, C. Restio, C. Darraud-Taupial, R. Guinerbretiere, and A. Dauger, "Structural characterization using x-ray diffraction of Ti indiffused periodically poled $LiNbO_3$ fabricated by direct electron beam bombardment," *Ferroelectr. Lett.*, vol. 30, p. 91, 2003.

[15] P. Pernot-Rejmankova, P. A. Thomas, P. Cloetens, F. Lorut, J. Baruchel, Z. W. Hu, P. Urenski, and G. Rosenman, "Periodically poled KTA crystal investigated using coherent X-ray beams," *J. Appl. Crystallogr.*, vol. 33, p. 1149, 2000.

[16] R. C. Miller *Phys. Rev.*, vol. 134, no. 5A, p. A1313, 1964.

[17] E. D. Mishina, N. E. Sherstyuk, D. R. Barskiy, and A. S. Sigov, "Domain orientation in ultrathin (Ba,Sr)TiO_3 films measured by optical second harmonic generation," *J. Appl. Phys.*, vol. 93, no. 10, p. 6216, 2003.

[18] V. Gopalan and T. E. Mitchell, "Wall velocities, switching times, and the stabilization mechanism of 180^o domains in congruent $LiTaO_3$ crystals," *J. Appl. Phys.*, vol. 83, p. 941, 1998.

[19] V. Gopalan, T. Mitchell, Y. Furukawa, and K. Kitamura, "The role of nonstoichiometric in 180^o domain switching of $LiNbO_3$ crystals," *Appl. Phys. Lett.*, vol. 72, p. 1981, 1998.

[20] J. G. Scott, S. Mailis, C. L. Sones, and R. W. Eason, "A Raman study of single-crystal congruent lithium niobate following electric-field repoling," *Appl. Phys. A*, vol. 79, p. 691, 2004.

[21] K. J. Vahala, "Optical microcavities," *Nat.*, vol. 424, p. 839, 2003.

[22] K. Vahala, ed., *Optical Microcavities*, vol. 5 of *Advanced series in Applied Phyiscs*. World Scinetific, 2004.

[23] V. Van, T. A. Ibrahim, P. P. Absil, F. G. Johnson, R. Grover, and P. T. Ho, "Optical signal processing using nonlinear semiconductor microring resonators," *IEEE J. Sel. Top. Quantum Electron.*, vol. 8, no. 3, p. 705, 2002.

[24] T. J. Sono, C. Riziotis, S. Mailis, and R. E. Eason, "Second harmonic generation via total internal reflection quasi-phase- matching in a hexagonal nonlinear optical microresonator," in *Proc. ECIO*, (ECIO, Copenhagen, Denmark), 2007.

[25] R. S. Weis and T. K.Gaylord, "Lithium niobate, summary of physical properties and crystal structure," *Appl. Phys. A*, vol. 37, p. 191, 1985.

[26] G. Malovichko, V. Grachev, and O. Schirmer, "Interrelation of intrinsic and extrinsic defects congruent, stoichiometric, and regularly ordered lithium niobate," *Appl. Phys. B*, vol. 68, p. 785, 1999.

[27] D. Xue and K. Kitamura, "Effects of Li^{+} and Nb^{5+} cationic sites on macroscopic properties of lithium niobate crystals," *J. Phys. chem. Solids*, vol. 66, p. 589, 2005.

[28] D. Xue and S. Zhang, "The effect of stoichiometry on nonlinear optical properties of $LiNbO_3$," *J. Phys.*, vol. 9, p. 7515, 1997.

[29] U. Schlarb and K. Betzler, "Refractive indices of lithium niobate as a function of temperature, wavelength and composition: A generalized fit," *Phy. Rev. B: Condens. Matter*, vol. 48, no. 21, p. 15613, 1993.

[30] M. De-Sario, M. N. Armenise, and C. Canali, "TiO_2, $LiNb_3O_8$, and ($Ti_xNb_{1-x}O_2$ compound kinetics during Ti:$LiNbO_3$ waveguide fabrication in the presence of water vapors," *J. Appl. Phys.*, vol. 57, p. 1482, 1985.

[31] O. F. Schirmer, O. Thiemann, and M. Wohlecke, "Defects in $LiNbO_3$ i. experimental aspects," *J. Phys. Chem. Solids*, vol. 52, no. 1, p. 185, 1991.

[32] R. J. Holmes and D. M. Smyth, "Titanium diffusion into $LiNbO_3$ as a function of stoichiometry," *J. Appl. Phys.*, vol. 55, p. 3531, 1984.

[33] T. J. Sono, J. G. Scott, C. L. Sones, C. E. Valdivia, S. Mailis, R. W. Eason, J. G. Frey, and L. Danos, "Reflection second harmonic generation on a z-cut congruent lithium niobate crystal," *Phys. Rev. B: Condens. Matter*, vol. 74, p. 205424, 2006.

[34] M. Houe and P. D. Townsend, "An introduction to methods of periodic poling for second harmonic generation," *J. Phys. D: Appl. Phys.*, vol. 28, p. 1747, 1995.

[35] R. W. Keys, A. Loni, R. De La Rue, C. N. Ionside, J. H. Masrh, B. J. Luff, and P. D. Townsend *Electron. lett.*, vol. 28, p. 189, 1990.

[36] C. Restoin, S. Massy, C. Darraud-Taupiac, and A. Barthelemy, "Fabrication of 1D and 2D structures at submicrometer scale on lithium niobate by electron beam bombardment," *Opt. Mater.*, vol. 22, p. 193, 2003.

[37] M. Fujimura, T. Suhara, and H. Nishihara, "Ferroelectric-domain inversion induced by SiO_2 cladding for $LiNbO_3$ waveguide SHG," *Electron. Lett.*, vol. 27, no. 13, p. 1207, 1991.

[38] M. Yamada, N. Nada, M. Saitoh, and K. Watanabe, "First-order quasi-phase matched $LiNbO_3$ waveguide periodically polde by applying an external field for efficient blue second-harmonic gereration," *Appl. Phys. Lett.*, vol. 62, no. 5, p. 435, 1993.

[39] L. H. Peng, Y. C. Fang, and Y. C. Lin, "Polarization switching of lithium niobate with giant internal field," *Appl. Phys. Lett.*, vol. 74, no. 14, p. 2070, 1999.

[40] V. Gopalan and C. G. Mool, "Origin of internal field and visualization of 180^o domains in congruent $LiTaO_3$ crystals," *J. Appl. Phys.*, vol. 80, p. 6099, 1997.

[41] D. H. Jundt, "Temperature dependent sellmeier equation for the index of refraction,n_e, in congruent lithium niobate," *Opt. Lett.*, vol. 22, no. 20.

[42] Z. Jiangou, Z. Shipin, X. Dingquan, W. Xiu, and X. Guanfeng, "Optical absorption properties of doped lithium niobate crystal," *J. Phys.: Condens. Matter*, vol. 4.

[43] B. K, "Light-induced charge transport processes in photorefractive crystals i: Models and experimental methods," *Appl. Phys. B*, vol. 64, no. 3, p. 273, 1997.

[44] B. K, "Light-induced charge transport processes in photorefractive crystals ii: Materials," *Appl. Phys. B*, vol. 64, no. 4, p. 391, 1997.

[45] Y. Ohmori, Y. Yasojima, and Y. Inishi, "Photoconduction, thermally stimulated luminescence, and optical damage in single crystal of $LiNbO_3$.," *Jpn. J. Appl. Phys.*, vol. 14, no. 9, p. 1291, 1975.

[46] J. A. Armstrong, N. Bloembergen, and P. S. Pershan, J. Ducuing, "Optically-induced refractive index inhomogeneities in $LiNbO_3$ and $LiTaO_3$.," *Appl. Phys. Lett.*, vol. 9, no. 1, p. 72, 1966.

[47] T. Volk, N. Runinia, and M. Wohlecke, "Optical-damage-resistant impurities in lithium niobate," *J. Opt. Soc. Am. B: Opt. Phys.*, vol. 11, no. 9, p. 1681, 1994.

[48] G. G. Zhong, J. Jian, and Z. K. Wu, "Measurements of optically induced refractive-index damage of lithium niobate doped with different concentrations of MgO," in *In Proceedings of the 11th International Quantum Electronics Conference*, vol. 631, (New York, USA), 1980.

[49] Y. Zhang, Y. H. Xu, M. H. Li, and Y. Q. Zhao, "Growth and properties of zn doped lithium niobate," *J. Cryst. Growth*, vol. 233, p. 537, 2001.

[50] L. Razzari, P. Minzioni, L. Cristiani, V. Degiorgio, and P. Kokanyan, "Photorefractivity of hafnium-doped congruent lithium-niobate crystal," *Appl. Phys. Lett.*, vol. 86, pp. 131914–1, 2005.

[51] C. C. Davis, *Lasers and Electro-Optics: Fundamental and Engineering*. Cambridge: Cambridge University Press, 1996.

[52] I. S h O j i, T. Kondo, and R. Ito, "Second-order nonlinear susceptibilities of various dielectric and semiconductor materials," *Opt. Quantum Electron.*, vol. 34, p. 797, 2002.

[53] M. Chin, C. Youtsey, W. Zhao, T. Pierson, Z. Ren, S. L. Wu, L. Wang, Y. G. Zhao, and S. T. Ho, "Gaas microcavity channel-dropping filter based on a race track resonator," *IEEE Photonics. Technol. Lett.*, vol. 11, p. 1620, 1999.

[54] V. Van, P. P. Absil, J. V. Hryniewics, and P. T. Ho, "Propagation loss in single-mode GaAsAlGaAs microring resonators: Measurement and model," *J. Lightwave Technol.*, vol. 19, no. 11, p. 1734, 2001.

[55] P. N. Butcher and D. Cotter, *The element of Nonlinear optics*. Cambridge: Cambridge Univesity Press, 1990.

[56] D. L. Mills, *Nonlinear Optics, Basic Concepts*. Berlin: Springer, second ed., 1998.

[57] N. Bloembergen and P. S. Pershan, "Light wave at the boundary of nonlinear media," *Phys. Rev.*, vol. 128, no. 2, p. 606, 1962.

[58] T. Stehlin, M. Feller, P. Guyot-Sionnest, and Y. R. Shen, "Optical second-harmonic generation as a surface probe for noncentrosymmetric media," *Opt. Lett.*, vol. 13, no. 5, p. 389, 1988.

[59] R. W. Boyd, *Nonlinear Optics*. New York: Academic Press, 2003.

[60] T. G. Zhang, C. H. Zhang, and G. K. Wong, "Determination of molecular orientation in molecular monolayes by second harmonic genaration," *J. Opt. Soc. Am. B: Opt. Phys.*, vol. 7, no. 6, p. 902, 1990.

[61] G. Liipke, D. J. Bottomley, and H. M. v. Driel, "Second- and third-harmonic generation from cubic centrosymmetric crystals with vicinal faces: phenomenological theory and experiment," *J. Opt. Soc. Am. B: Opt. Phys.*, vol. 11, no. 1, p. 33, 1994.

[62] C. Yamada and T. Kimura, "Rotational symmetry of the surface second-harmonic generation of zinc-blende-type crystals," *Phys. Rev. B: Condens. Matter*, vol. 49, no. 20, p. 14372, 1994.

[63] J. E. Meja, B. S. Mendoza, M. Palummo, G. Onida, and R. Del Sole, "Surface second-harmonic generation from Si(111)(1 × 1)H: Theory versus experiment," *Phys. Rev. B: Condens. Matter*, vol. 66, p. 195329, 2002.

[64] H. W. K. Tom, T. F. Heinz, and Y. R. Shen, "Second-harmonic reflection from silicon surface and its relation to structural symmetry," *Phys. Rev. B: Condens. Matter*, vol. 51, no. 21, p. 1983, 1983.

[65] C. Jung, B. K. Rhee, and D. Kim, "Simple method for determining the crystalline axes of nonlinear uniaxial crystal with second-harmonic generation," *Appl. Opt.*, vol. 39, no. 28, p. 5142, 2000.

[66] S. K. Andersson, M. C. Schanne-Klein, and F. Hache, "Symmetry and phase determination of second-harmonic reflection from calcite surfaces," *Phys. Rev. B: Condens. Matter*, vol. 59, no. 4, p. 3210, 1999.

[67] M. E. Lines and A. M. Glass, *Priciples and Applications of Ferroelectrics and Related materials*. Oxford: Clarendon, 1977.

[68] D. Xue and K. Kitamura, "Effects of Li^+ and Nb^{5+} cationic sites on macroscopic properties of lithium niobate crystals," *J. Phys. Chem. solids*, vol. 66, no. 2-4, p. 589, 2005.

[69] M. Houe and P. D. Townsend, "Thermal polarization reversal of lithium niobate," *Appl. Phys. Lett.*, vol. 66, p. 2667, 1995.

[70] D. Klunder, E. Kriosukov, F. S. Tan, T. V. D. Veen, H. F. Bulthuis, G. Sengo, C. Otto, H. J. W. M. Hoekstra, and A. Driessen, "Vertically and laterally waveguide-coupled cylindrical microresonators in Si_3N_4 on SiO_2 technology," *Appl. Phys. B*, vol. 73, p. 603, 2001.

[71] T. M. Benson, S. V. Boriskina, P. Sewell, A. Vukovic, S. C. Greedy, and A. I. Nosich1, *Frontiers in planar lightwave circuit technolgy: Design, simulation, and Fabrication*, vol. 216 of *Nato Science series II: Mathematics, Physics and Chemistry*. Netherlands: Springer.

[72] V. Lefevre-Seguin and S. Haroche, "Towards cavity-QED experiments with silica microspheres," *Mater. Sci. Eng. B*, vol. 48, p. 53, 1997.

[73] M. Ilchenko, V.S.and Gorodetsky, X. Yao, and L. Maleki, "Microtorus: a highfinesse microcavity with whispering-gallery modes," *Opt. Lett.*, vol. 26, p. 256, 2001.

[74] T. J. Armani, D. K.and Kippenberg, S. M. Spillane, , and K. Vahala, "Ultra-high-q toroid microcavity on a chip," *Nat.*, vol. 421, p. 905, 2003.

[75] A. Polman, B. Min, J. Kalkman, T. Kippenberg, and K. Vahala, "Ultralow-threshold erbium-implanted toroidal microlaser on silicon," *Appl. Phys. Lett.*, vol. 84, no. 7, p. 1037, 2004.

[76] B. Little, S. Chu, H. Haus, J. Foresi, and J.-P. Laine, "Microring resonator channel dropping filters," *J. Lightwave Technol.*, vol. 15, p. 998, 1997.

[77] B. Little, W. Chu, S.T.and Pan, D. Ripin, T. Kaneko, Y. Kokubun, and E. Ippen, "Vertically coupled glass microring resonator channel dropping filters,," *IEEE Photon. Technology. Lett.*, vol. 11, no. 2, p. 215, 1999.

[78] R. Grover, P. Absil, V. Van, J. Hryniewicz, B. Little, O. King, L. Calhoun, F. Johnson, and P. Ho, "Vertically coupled gainaspinp microring resonators," *Opt. Lett.*, vol. 26, p. 506, 2001.

[79] D. Rafizadeh, J. P. Zhang, S. C. Hagness, A. Taflove, K. A. Stair, and S. T. Ho, "Photorefractivity of hafnium-doped congruent lithium-niobate crystal," *Opt. Lett.*, vol. 22, p. 1244, 1997.

[80] C. Y. Fong and A. W. Poon, "Mode field patterns and preferential mode coupling in planar waveguide-coupled square microcavities," *Opt. Express*, vol. 11, p. 2897, 2003.

[81] M. Lohmeyer, "Mode expansion modeling of rectangular integrated optical microresonators," *Opt. Quantum. Electron.*, vol. 34, p. 541, 2002.

[82] J. Wiersig, "Hexagonal dielectric resonators and microcrystal lasers," *Phys. Rev. A: At. Mol. Opt. Phys.*, vol. 67, p. 023807, 2003.

[83] N. Ma, C. Li, and A. W. Poon, "Laterally coupled hexagonal micropillar resonator adddrop filters in silicon nitride," *IEEE Photon. Technol. Lett.*, vol. 16, no. 16, p. 2487, 2004.

[84] I. Braun, G. Ihlein, F. Laeri, J. U. Nckel, G. Schulz-Ekloff, F. Schth, U. Vietze, O. Weib, and D. Whrle, "Hexagonal microlasers based on organic dyes in nanoporous crystals," *Appl. Phys. B*, vol. 70, p. 335, 2000.

[85] O. Painter, R. Lee, A. Scherer, A. Yariv, J. OBrien, P. Dapkus, and I. Kim, "Two-dimensional photonic band-gap defect mode laser," *Science*, vol. 284, p. 1819, 1999.

[86] I. Kiyat and A. Aydinli, "High-q silicon-on-insulator optical rib waveguide racetrack resonators," *Opt. Express*, vol. 13, p. 1900, 2005.

[87] M. R. Poulsen, P. I. Borel, J. Fage-Pedersen, J. Hubner, M. Kristensen, J. H. Povlsen, K. Rottwitt, M. Svalgaard, and W. Svendsen, "Advances in silica-based integrated optics," *Opt. Eng.*, no. 10, p. 2821, 2003.

[88] A. Vrckel, M. Mnster, W. Henschel, P. H. Bolivar, and K. H, "Asymmetrically coupled silicon-on-insulator microring resonators for compact adddrop multiplexers," *IEEE Photon. Technol. Lett.*, vol. 15, no. 7, p. 921, 2003.

[89] C. J. Kaalund, "Critically coupled ring resonators for add-drop filtering," *Opt/ Commun.*, vol. 237, p. 357, 2004.

[90] A. Yariv, "Universal relations for coupling of optical power between microresonators and dielectric waveguides," *Electron. Lett.*, vol. 36, p. 321, 200.

[91] J. M. Choi, R. K. Lee, and A. Yariv, "Control of critical coupling in a ring resonator-fiber configuration: application to wavelength-selective switching, modulation, amplification, and oscillation," *Opt. Lett.*, vol. 26, no. 16, p. 1236, 2001.

[92] A. Yariv, "Critical coupling and its control in optical waveguide-ring resonator systems," *IEEE Photon. Tech. Lett.*, vol. 14, p. 483, 2002.

[93] G. Griffel, "Synthesis of optical filters using ring resonator arrays," *IEEE Photon. Technol. Lett.*, vol. 12, p. 810, 2000.

[94] N. Ma, *Laterally coupled hexagonal micro-pillar resonator add-drop filter for optical communications*. MPhil, The Hong Kong Univ. of Science and Tech., 2004.

[95] H. Kogelnik and V. Ramaswamy, "Scaling rules for thin-film optical waveguides," *Appl. Opt*, vol. 13, no. 8, p. 1857, 1974.

[96] G. Hocker and K. W. Burns, "Mode dispersion in diffused channel waveguides by the effective index method," *Appl. Opt.*, vol. 16, p. 114, 1977.

[97] Y. Liu, T. Chang, and A. E. Craig, "Coupled mode theory for modeling microring resonators," *Opt. Eng.*, vol. 44, no. 8, pp. 084601–1, 2005.

[98] C. Li, L. Zhou, S. Zheng, and A. W. Poon, "Silicon polygonal microdisk resonator," *IEEE J. Sel. Top. Quantum Electron.*, vol. 12, no. 6, p. 1438, 2006.

[99] N. Ma, F. K. L. Tung, S. F. Lui, and A. W. Poon, "Hexagonal micro-pillar cavities: multimode resonances and open-loop resonance linewidth broadening," in *Proc. SPIE*, vol. 4986, (Photonics West Conference, San Jose, California), 2003.

[100] A. K. Bhowmik, "Polygonal optical cavities," *Appl. Opt.*, vol. 39, p. 3071, 2000.

[101] A. Yariv and P. Yeh, *Optical waves in crystals: Propagation and control of laser radiation*. New Jersey: Wiley-Interscience, Wiley classics library ed., 2003.

[102] D. M. Sheen, S. M. Ali, M. D. Abouzahra, and J. A. Kong, "Application of the three-dimensional finite-difference time domain method to the analysis of planar microstrip circuits," *IEEE. Trans. Microwave. Theory Tech.*, vol. 38, p. 849, 1990.

[103] S. Chu and S. K. Chaudrhuri, "A finite difference time-domain method for the design and analysis of guided-wave optical strucatures," *J. Lightwave Technol.*, vol. 7, p. 2033, 1989.

[104] J. Berenger, "Three-dimensional perfectly matched layer for the absorption of electromagnetic waves," *J. Comp. Phys.*, vol. 127, p. 363, 1996.

[105] T. Kako and Y. Ohi, *Domain Decomposition Methods in Science and Engineering XVII*, vol. 10 of *Lecture Notes in Computational Science and Engineering*. Berlin Heidelberg: Springer.

[106] S. G. Johnson, *Notes on Perfectly Matched Layers (PMLs)*.

[107] S. Zheng, N. Ma, and A. W. Poon, "Experimental demonstration of waveguide-coupled hexagonal micropillar resonators with round-corners in silicon nitride," in *Proc. Cleo*, vol. CMY5, 2005.

[108] C. Li and A. W. Poon, "Experimental demostration of waveguide-coupled round-cornered octagonal microresonator in silicon nitride," *Opt. Lett.*, vol. 30, no. 5, p. 546, 2005.

[109] P. P. Absil, J. V. Hryniewicz, B. E. Little, P. S. Cho, R. A. Wilson, L. G. Joneckis, and P.-T. Ho, "Wavelength conversion in GaAs micro-ring resonators," *Opt. Lett.*, vol. 25, no. 8, p. 554, 2000.

[110] V. S. Ilchenko, A. A. Savchenkov, A. B. Matsko, and L. Maleki, "Nonlinear optics and crystalline whispering gallery mode cavities," *Phys. Rev. Lett.*, vol. 92, pp. 043903–1, 2004.

[111] S. Schiller and R. L. Byer, "Quadruply resonant optical parametric oscillation in a monolithic total-internal-reflection resonator," *J. Opt. Soc. Am. B*, vol. 10, no. 9, p. 1696, 1993.

[112] Y. Xu, K. Lee, and A. Yariv, "Propagation and second-harmonic generation of electromagnetic waves in a coupled-resonator optical waveguide," *J. Opt. Soc. Am. B*, vol. 17, no. 53, p. 387.

[113] K. Sakoda and K. Ohtaka, "Sum-frequency generation in a two-dimensional photonic lattice," *Phys. Rev. B*, vol. 54, p. 5742, 1996.

[114] Y. Dumeige and P. Feron, "Whispering-gallery-mode analysis of phase-matched doubly resonant second-harmonic generation," *Phys. Rev. A*, vol. 74, p. 063804, 2006.

[115] P. D. Maker, R. W. Terhune, M. Nisenhoff, and C. M. Savage *Phys. Rev. lett.*, vol. 8, p. 21, 1962.

[116] A. Melloni, "The effect of phase matching method and of uniaxal crystal symmetry on the polar distribution of second-order nono-linear optical polarization," *Br. J. Appl. Phys.*, vol. 26, no. 12, p. 1135, 1965.

[117] N. G. R. Broderick, G. W. Ross, H. L. Offerhaus, D. J. Richardson, and D. C. Hanna, "Hexagonally poled lithium niobate: a two-dimensional nonlinear photonic crystal," *Phys. Rev. lett.*, vol. 84, no. 19, p. 4345, 2000.

[118] J. W. Minford, S. K. Korotky, and R. C. Alferness, "Low-loss Ti:$LiNbO_3$ waveguide bends at $\lambda = 1.3\mu$m," *IEEE J. Quantum Electron.*, vol. 18, no. 10, p. 1802, 1982.

[119] G. Hocker and K. W. Burns, "Modes in diffused optical waveguides of arbitrary index profile," *IEEE J. Quantum electron.*, vol. 11, p. 270, 1975.

[120] S. K. Korotky, W. J. Minford, L. L. Buhl, M. D. Divino, and R. C. Alferness, "Mode size and method for estimating the propagation constant of single-mode Ti:$LiNbO_3$ strip waveguide," *IEEE J. Quantum electron.*, vol. 18, no. 10, p. 1796, 1982.

[121] K. T. Koai and P.-L. Liu, "Modeling of Ti:$LiNbO_3$ waveguide devices: Part i- directional couplers," *J. Lightwave Technol.*, vol. 7, no. 3, p. 533, 1989.

[122] M. Fukuma, J. Noda, and H. Iwasaki, "Optical properties in titanium-diffused $LiNbO_3$ strip waveguides," *J. Appl. Phys.*, vol. 49, p. 3693, 1978.

[123] K. K. Wong, *Properties of Lithium Niobate*, p. 119. No. 28 in emis Datareviews series, INSPEC, 2002.

[124] Y. J. Chuang, F. G. Tseng, and W. K. Lin, "Reduction of diffraction effecr of UV expeosure on SU8 negative thick photoresist by air gap elimination," *Microsyst. Technol.*, vol. 8, p. 308, 2002.

[125] A. Sjoberg, G. Arvidsson, and A. A. Lipovskii, "Characterization of waveguides fabricated by titanium diffusion in magnesium-doped lithium niobate," *J. Opt. Soc. Am. B: Opt. Phys.*, vol. 5, p. 285, 1988.

[126] F. Lacour, N. Courjal, M.-P. Bernal, A. Sabac, C. Bainier, and M. Spajer, "Nanostructuring lithium niobate substrates by focused ion beam milling," *Opt. Mater.*, vol. 27, p. 1421, 2005.

[127] M. N. Armenise, "Fabrication techniques of lithium niobate waveguides," *IEE Proceedings*, vol. 135, p. 85, 1988.

[128] X. Cao, R. Srivastava, R. V. Ramaswamy, and J. Natour, "Recovery of second-order opticalnonlinearity in annealed proton-exchanged $LiNbO_3$," *IEEE Photonics. Technol. Lett.*, vol. 3, no. 1, p. 25, 1991.